Dynamically Consistent Interpretation of the Seismic Structure at the Base of the Mantle

Thesis by

Igor A. Sidorin

In Partial Fulfillment of the Requirements

for the Degree of

Doctor of Philosophy
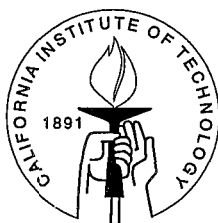
California Institute of Technology

Pasadena, California

1999

(Submitted May 6, 1999)

Acknowledgements

The years at Caltech have been very rewarding in many different ways. I was lucky to learn from some of the brightest people, and the friendships I made here definitely made this experience even more enjoyable. I am very grateful to all the faculty, staff, and students of the Seismo Lab and, in fact, the whole Division, for the remarkable environment of freedom and independence coupled with numerous available sources of help and inspiration.

My deepest appreciation goes to my research advisor, Mike Gurnis. His faith in me as a scientist and continuous encouragement have ultimately allowed me to stay the course and carry through this work. His guidance and remarkable scientific insight has helped me to overcome many stumbling blocks along the way. I am also very fortunate to have worked closely with Don Helmberger. His vast experience and terrific sense of humor make all those waveforms suddenly become down-to-Earth and make some sense. Both Don and Mike not only inspired me to quest the understanding of the enigmatic world of nature, but also served as role models demonstrating remarkable integrity, enthusiasm, and dedication to science. They nurtured the scientist in me, and I am especially grateful for their interest in my future beyond my graduate career.

Don Anderson has always amazed me with his erudition, and the breadth and depth of his knowledge. Discussions with him have largely shaped my understanding of the Earth.

Rob Clayton has been more than just my academic advisor. I am very grateful for his constant willingness to help. It is enough to mention that he once came to the Lab on a weekend just to fix a problem with my computer. Given that it was a day before AGU, the degree of my appreciation should be obvious!

I thank Joann Stock for the unforgettable research cruise to Antarctica. Katrin Haffner, Jim Holik (Antarctic Support Associates), and Tim Melbourne made the most memorable trip of my life even more delightful.

I would also like to thank John Holbrook (Southeast Missouri State University), Michael Hamburger (Indiana University), and Rod Myers (Stanford University) and their families for their hospitality during my first visit to the USA. John and his wife Camila have my warmest gratitude for their friendship, their belief in me, and the encouragement that essentially led me to pursue a graduate career.

Professor Vladimir Smirnov, my research advisor at Moscow State University, planted the seeds of scientific curiosity in me and enlivened my research interests.

But all of this would not be possible without the tremendous support on the part of my family. I am forever grateful to my parents who have worked so hard and sacrificed so much to give me every opportunity to pursue knowledge and education. Throughout my life they have been a constant source of emotional, spiritual, and financial support, and all my love to them will never be enough to thank them for all they have done.

My wife Natasha and son Sasha have provided a solid home base and motivation to carry through the work. Without their love, understanding and continuous support and encouragement this thesis would never happen. I deeply appreciate their patience and tolerance, I love them with all my heart and am very sorry if this work consumed a little more of the precious time that I could have spend with them. I devote this thesis to my wife, my son, and my parents.

To My Parents

Abstract

There is increasing evidence of large degrees of heterogeneity in the seismic structure of the lowermost 200–300 km of the mantle constituting the D" layer. The region is believed to play an important role in the dynamics of the mantle and the Earth as a whole. This is the place where hot plumes, reaching the Earth's surface may originate. This is also the region where most of the lithosphere subducted from the surface may ultimately settle. The interface between the two largest structural domains of the Earth, the core-mantle boundary, is also a zone of active chemical reactions.

One of the most diagnostic seismologically observed features in the D" region is an apparent seismic velocity discontinuity 200–300 km above the core-mantle boundary, generally referred to as the D" discontinuity. The primary evidence for the discontinuity comes from the observed seismic triplication with phases Scd or Pcd arriving between the direct arrival, S or P, and the core-reflected, ScS or PcP, in the 65°–85° distance range. The cause of this abrupt velocity increase is unknown and various explanations have been advanced, including sharp thermal gradients, a chemical interface, or a solid-solid phase transition. However, neither seismology nor geodynamics alone can distinguish between the alternatives. In addition, no satisfactory explanation has yet been given to the apparent intermittance of the D" discontinuity, as the triplication is strong in some regions (such as Alaska or Central America) but weak or missing in other regions (such as Central Pacific).

We use a combination of dynamic and seismic waveform modeling to provide tighter constraints on this structural feature of D" and reduce the tradeoffs that exist in both seismological studies and dynamic modeling. The dynamic models are based on the adiabatic model that is computed in Chapter 2 by integrating available mineral physics data. The temperature field, chemical heterogeneity, and the distribution of phases computed from convection models are mapped to seismic velocities which are then used to compute synthetic seismic waveforms. By comparing these waveforms

with data, we rule out some classes of dynamic models in favor of others. In particular, in Chapter 3 we demonstrate that a model with a chemical layer at the base of the mantle does not provide a consistent explanation for the seismological observations of the D" discontinuity. We propose that the strength of the triplication is conditioned by both the abrupt velocity increase at the D" discontinuity and the local velocity structure accompanying the discontinuity. Variations of the local structure strongly modulate the strength of the observed triplication and provide a natural explanation for the apparent intermittance. We also show that purely thermal gradients computed from convection models do not produce a sufficiently strong Scd phase. In Chapter 4 we suggest that the observed regional patterns in the strength of the D" triplication are most compatible with a phase change model of the D" discontinuity. In Chapter 5 a variety of convection models with a basal phase transition are tested to obtain the characteristics of the phase transition most compatible with observations. We find that the best value for the ambient elevation above the core-mantle boundary is about 150 km and the best value for the Clapeyron slope is about 6 MPa/K. In Chapter 6 this model is further tested by placing a discontinuity in context of the global shear velocity structure recovered by Grand's [1994] tomography model. We find that such a synthetic velocity model with a phase change characterized by a shear velocity contrast of 1.5%, ambient elevation $\sim$ 200 km and Clapeyron slope $\sim$ 6 MPa/K predicts the observed differential travel times patterns for the D" triplication beneath Alaska, Eurasia and Central America. The model also provides an explanation for the apparent intermittance of the D" discontinuity by predicting very weak triplication for Central Pacific and north-eastern Caribbean where convincing evidence for the D" triplication is lacking.

Contents

List of Figures

List of Tables

Chapter 1 General Introduction

The seismologically observed heterogeneity at the bottom 200-300 km of the mantle constituting the D" region is becoming increasingly apparent. The amplitudes of seismic velocity anomalies can exceed 10% for both P and S waves and the scales of the anomalies range from several tens to several thousand kilometers. This structural complexity probably reflects a variety of interacting geophysical processes that take place in the core-mantle boundary (CMB) region and are believed to play a major role in global dynamics (see [*Lay et al.*, 1998] for a review). Interpreting the seismic structure at the base of the mantle provides a key to understanding the dynamic complexity and ultimately the evolution of the Earth as a whole.

The large-scale structure of the mantle has been established using long-period tomography techniques (e.g., [*Dziewonski and Woodhouse*, 1987; *Su et al.*, 1994; *Li and Romanowicz*, 1996; *Masters et al.*, 1996]). Although some differences exist between various models, several large-scale features in the deep mantle are common to most studies. These include broad low velocity regions beneath Africa and the Pacific and a relatively fast circum-Pacific fringe. The sharpness of these large-scale features and the lateral transitions between the regions with fast and slow velocities remain unresolved.

Higher resolution can be obtained by using body-wave tomography. In some regions, such as beneath the Americas, the raypath coverage is sufficient to image structures in the deep mantle with dimensions within a few hundred kilometers. A tomography model computed by *Grand* [1994] using S body-wave data displays narrow linear high velocity features for several regions beneath the circum-Pacific belt. This picture is corroborated by a detailed P-wave tomography study [*van der Hilst et al.*, 1997] that employed completely different data types and methods. In addition, the same features are found in the mid-mantle using high resolution surface waves overtones [*van Heijst and Woodhouse*, 1998]. In some regions these fast veloc-

ity structures can be traced from the surface to the base of the mantle [*van der Hilst et al.*, 1997] and their morphology has some similarities with the thermal structure of subducting slabs obtained in convection modeling (e.g., [*Bunge et al.*, 1998]), suggesting that these structures represent the lithosphere subducting to the bottom of the mantle.

Mapping of even smaller variations at the base of the mantle has been achieved by modeling the differential waveform behavior of phases interacting with D" and the CMB. Such studies have revealed ultra low velocity zones with large reductions in both P and S velocities beneath the mid-Pacific, Africa and other regions (see [*Lay et al.*, 1998] for review). These structures appear to be related to the larger scale low velocity regions, as discussed by *Garnero and Helmberger* [1995].

In contrast, the large-scale high velocity structures appear to have a positive velocity jump at the top of the D" region, as was first suggested by *Lay and Helmberger* [1983]. The primary evidence for this D" discontinuity is based on an extra phase (Scd) that arrives between S and ScS at epicentral distances from 65° to 85° forming a triplication. The triplication is also observed for P waves in some regions however, the low signal to noise ratio in P waveforms significantly complicates its detection (e.g., [*Ding and Helmberger*, 1997]). The timing and amplitude of Scd relative to S and ScS shows considerable variations (see review in [*Wysession et al.*, 1998]). Four regions that have been well studied and where Scd is clearly displayed are indicated in Figure 1.1 along with the inferred 1-D velocity models. Model SGLE [*Gaherty and Lay*, 1992] is a reference model for the raypaths under the northern Siberia, SYLO [*Young and Lay*, 1990] for the raypaths under Alaska, SYL1 [*Young and Lay*, 1987] for the raypaths under India, and SLHA [*Lay and Helmberger*, 1983] for the raypaths under Central America. Due to existing tradeoffs, such 1-D reference models are not unique [*Sidorin et al.*, 1998]. For example, several different 1-D models have been proposed to approximate the structure beneath Central America [*Lay and Helmberger*, 1983; *Kendall and Nangini*, 1996; *Ding and Helmberger*, 1997; *Sidorin et al.*, 1998]. Two of them – SLHA and SGHD120 – are shown in Figure 1.1. While model SLHA has a 2.75% jump at the top of D", common to most models explaining the triplication,

in the structure approximated by model SGHD120, a similar triplication arises due to only a 1% discontinuity overlain by a 120 km transition zone with a high gradient [*Sidorin et al.*, 1998].

A recent study by *Lay et al.* [1997] addressed these variations in the structure of the D" discontinuity considering the correlations and spatial patterns in Scd-S, ScS-Scd, and ScS-S differential travel time residuals for raypaths sampling the lowermost mantle in three different regions of the world. The study suggested a strong lateral heterogeneity at scale lengths of 600-1500 km at the base of the mantle with significant heterogeneity at smaller (200-500 km laterally) scales. The strongest heterogeneity was prescribed to the region just above or within a top thin layer of D". Although these observations alone may have important dynamic implications, the analysis was unable to distinguish between the volumetric velocity anomalies and the topography of the D" discontinuity. Even when the velocity structure is well constrained, it does not allow a unique determination of the variation of material properties, such as elastic moduli, density or viscosity, all of which to some extent control the dynamics of mantle flow. The data that is used to study the D" seismic structure, for example, are either not sensitive to the density variations (as SH reflections off the discontinuity) or are heavily contaminated by either noise or superposition of other phases (as SV or P reflections). Consequently, seismological modeling alone fails to distinguish between thermal and compositional influences on the velocity field.

The complexity of the D" region, its remoteness from the surface, and its ultimate importance in the global dynamics of the Earth call for an interdisciplinary approach to its exploration. Such approach is particularly important due to ambiguities in the interpretation of seismologically inferred structure and inherent uncertainties and tradeoffs of seismic imaging. More importantly, only a comprehensive integration of diverse observations from various disciplines may help to bring all the pieces of the puzzle together in a coherent manner and lead to a self-consistent unified model of the mantle. Such a model must reconcile seismological observations with dynamic constraints as well as mineral physics data and geochemical implications. Several such studies attempting to integrate some of these observations have been undertaken.
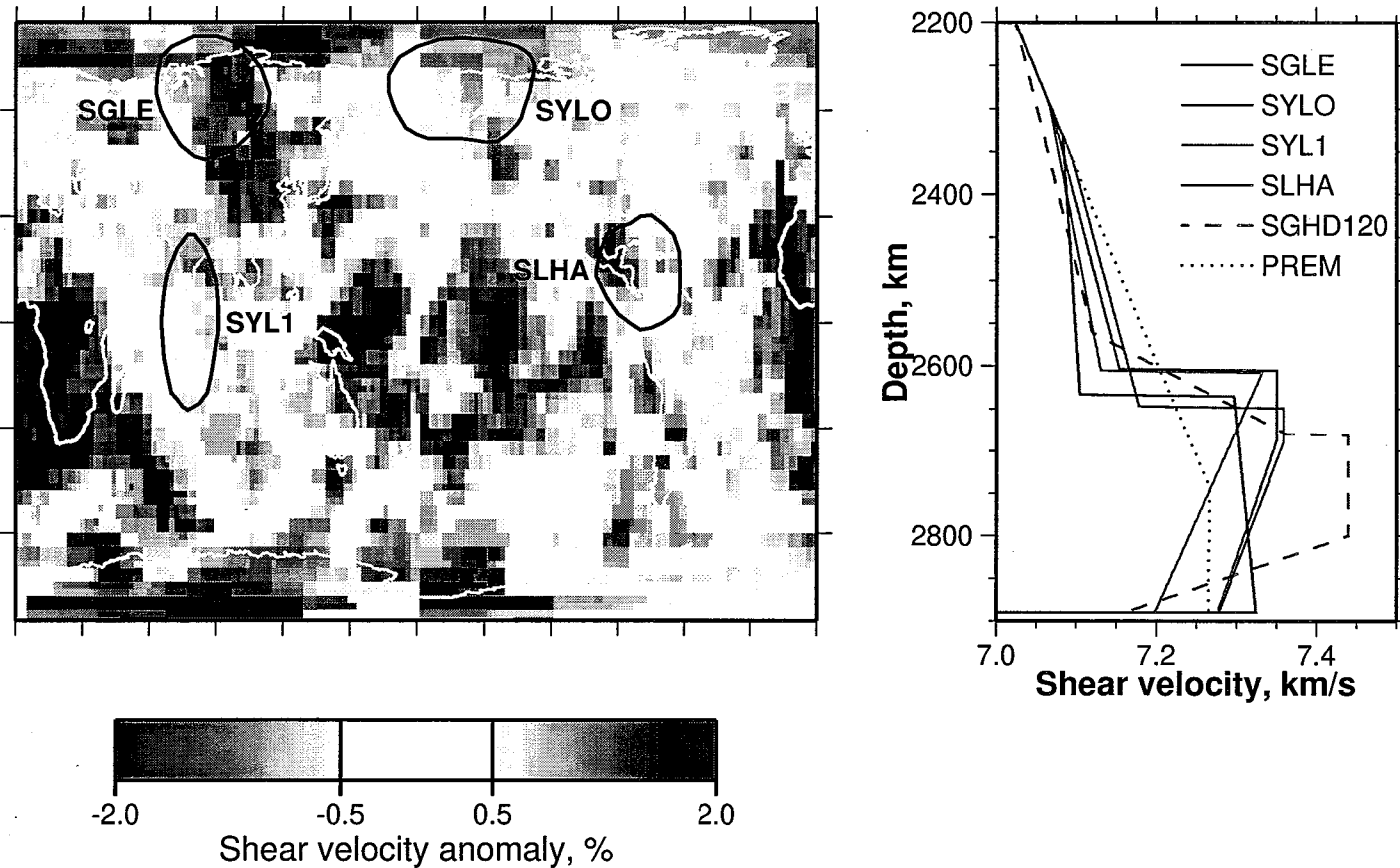
Figure 1.1: Location of the four geographical regions where there is strong evidence for the D" triplication. The color map shows the average shear velocity anomaly in the lowermost 250 km of the mantle [*Grand et al.*, 1997]. The reference 1-D models corresponding to the four regions along with PREM are given on the right: SGLE [*Gaherty and Lay*, 1992] is a reference model for the structure beneath northern Siberia; SYLO [*Young and Lay*, 1990] for the structure beneath Alaska; SYL1 [*Young and Lay*, 1987] for the structure beneath India and Indian ocean; SLHA [*Lay and Helmberger*, 1983] for the structure beneath Central America. Model SGHD120 [*Sidorin et al.*, 1998] approximates the structure beneath Central America using a 1% discontinuity and a 120 km transition zone above it. PREM [*Dziewonski and Anderson*, 1981] is a global Earth reference model.

Christensen and Hofmann [1994] studied mixing and transport in a thermo-chemical model of convection and predicted isotopic systematics of mantle derived basalts. *Forte and Peltier* [1989] compared seismically inferred CMB topography with that produced by a global flow model using buoyancy constrained by seismic tomography. Several studies attempted to predict temperature or density variations in the mantle from tomographic models (e.g., *Hager et al.* [1985]; *Yuen et al.* [1993]) or seismic velocities from dynamic models (e.g., *Davies and Gurnis* [1986]). However, all previous studies generally use simple scalings between temperature and seismic velocity while a comprehensive interrelation between the dynamic modeling and mantle composition and thermoelastic properties is required.

It is obvious that the increasing resolution of tomography, more sophisticated dynamical models, and rapidly developing techniques in mineral physics experiments which provide elastic properties at higher pressures and temperatures, require a systematic approach to the problem. Such a systematic approach should allow us to close the gap between seismological inversions and dynamic models.

In Chapter 2 we integrate the currently available mineral physics data coupled with geochemical constraints on the composition to compute an adiabatic model of thermoelastic parameters of the lower mantle. Particular attention is given to the depth dependence of the coefficient of thermal expansion, as this parameter influences the dynamic regime of mantle flow and to a large extent controls the mapping between thermal perturbations and seismic velocity anomalies. The resulting adiabatic model is used in Chapters 3–5 to compute dynamic models and infer seismic velocities consistent with them. By comparing the waveforms produced by these seismic velocity structures with seismic data, we reject certain classes of dynamic models as incompatible with seismological observations. In Chapter 6 we add a refined structure to large scale seismic tomography models and test a specific mechanism (a phase-transition) for the D" shear velocity discontinuity.

Chapter 2   Geodynamically Consistent Seismic Velocity Predictions in the Lower Mantle

2.1   Abstract

By integrating the available mineral physics data we compute a model of thermoelastic properties for a chemically homogeneous adiabatic lower mantle. Particular attention is given to the pressure dependence of the coefficient of thermal expansion, α. A technique of perturbing the seismic velocities to account for possible effects of non-adiabaticity is introduced. Such non-adiabatic effects may include thermal perturbations, chemical anomalies or phase transitions. The computed adiabatic thermoelastic parameters are used in the following chapters to constrain the dynamic models and the described velocity perturbation technique is used to obtain the seismic velocity fields from computed dynamic models.

2.2   Introduction

To make the dynamic simulation and the seismic velocities inferred from it consistent, a coherent adiabatic reference model of thermoelastic parameters as a function of depth is required for the whole mantle. Since the focus of this study is the bottom of the mantle, we start by computing an adiabatic model for a chemically homogeneous lower mantle, using currently existing mineral physics data and geochemical constraints. Where necessary, the upper mantle parameters can be evaluated by interpolating between the lower mantle and surface values. The difficulties of measuring the properties of rocks under simultaneous high pressures and temperatures have lead

to a considerable discrepancy in the results produced by different researchers or using different techniques. In this chapter we attempt to integrate the available mineral physics measurements and theoretical predictions to constrain the depth and temperature dependence of thermoelastic properties of the two major elements of the lower mantle: silicate perovskite and magnesiowüstite. The weighted averaging of these properties provides an adiabatic model of the lower mantle which we use in the following chapters to constrain the dynamic models. In addition, we develop a technique that we use in the following chapters to adjust the adiabatic values of seismic velocities for the non-adiabatic effects (temperature, chemical heterogeneity and phase transition) that are computed in convection simulations.

2.3   Adiabatic model for chemically homogeneous lower mantle

The approach we used to calculate the adiabatic model for a chemically homogeneous lower mantle is similar to that of *Zhao and Anderson* [1994]. A $(Mg,Fe)SiO_3$ perovskite – $(Mg,Fe)O$ magnesiowüstite lower mantle composition is assumed with given molar partitioning coefficient $\chi_{Pv} = Pv/(Pv + Mw)$ and a molar fraction of iron $\chi_{Fe} = Fe/(Fe + Mg)$. The values of the adiabatic bulk modulus, K_S, rigidity, G, and density, ρ, at a given foot temperature, T_f, of the adiabat (i.e., temperature at depth $z = 0$), are calculated separately for $(Mg,Fe)SiO_3$ and $(Mg,Fe)O$ using equations [*Burdick and Anderson, 1975*]:

$$K_S(P_0, T_f) = K_{S_0} \exp\left\{-\int_{T_s}^{T_f} \alpha(T)\bar{\delta}_S dT\right\} \tag{2.1}$$

$$G(P_0, T_f) = G_0 \exp\left\{-\int_{T_s}^{T_f} \alpha(T)\bar{\Gamma} dT\right\} \tag{2.2}$$

$$\rho(P_0, T_f) = \rho_0 \exp\left\{-\int_{T_s}^{T_f} \alpha(T) dT\right\}, \tag{2.3}$$

where $T_s = 300K$ is the surface temperature, $P_0 = 0$ is the surface pressure, $K_{S_0} = K_S(P_0, T_s)$, $G_0 = G(P_0, T_s)$ and $\rho_0 = \rho(P_0, T_s)$ are the ambient adiabatic bulk mod-

ulus, rigidity and density, respectively, $\alpha(T) \equiv 1/V(\partial V/\partial T)_P$ is the coefficient of thermal expansion at $P = 0$, $\bar{\delta}_S \equiv (\partial \ln K_S/\partial \ln \rho)_P$ and $\bar{\Gamma} \equiv (\partial \ln G/\partial \ln \rho)_P$ are average dimensionless anharmonic parameters at $P = 0$ (taken as a mean value of the corresponding ambient and high temperature parameters).

The major difference between our calculations and the study of *Zhao and Anderson* [1994] is in the approach to the pressure and temperature dependence of the coefficient of thermal expansion, α. The coefficient of thermal expansion has a significant influence on both the dynamics of convection [*Yuen et al.*, 1991] and the seismic velocity calculation and is the major parameter linking the convection simulation and seismic velocity prediction in our study. This is why an accurate analysis of this important property as a function of pressure, temperature and composition is required.

The values of α for magnesiowüstite reported by various authors (e.g., [*Chopelas*, 1996; *Chopelas and Boehler*, 1992; *Duffy and Ahrens*, 1993; *Isaak et al.*, 1989, 1990; *Suzuki*, 1975]) seem to agree rather well with each other. Though the current state of the experimental techniques is not able to provide accurate measurements at simultaneous high pressures and temperatures appropriate for the bottom of the mantle, the values at intermediate pressures and temperatures can be extrapolated to the required conditions with a certain degree of uncertainty. Fortunately, there seems to be general agreement on the first-order temperature and pressure dependence of α for (Mg,Fe)O [*Anderson et al.*, 1992; *Chopelas and Boehler*, 1992]. For temperature dependence of the coefficient of thermal expansion of magnesiowüstite at $P = 0$ in equations (2.1)-(2.3), we use the data from [*Isaak et al.*, 1989].

However, the database of experimental measurements of α for silicate perovskite, (Mg,Fe)SiO$_3$, is sparse and inconsistent even at ambient conditions. An analysis of various reports shows that the range of reported values seem to have a bimodal nature, clustering around low values of about 1.7×10^{-5} K^{-1} [*Wang et al.*, 1994; *Chopelas*, 1996; *Stacey*, 1996] and high values about 4.0×10^{-5} K^{-1} [*Knittle et al.*, 1986; *Mao et al.*, 1991; *Patel et al.*, 1996].

In this study, the low values of α for (Mg,Fe)SiO$_3$ are favored for the follow-

ing reasons. First, such values were supported by different experimental techniques. The values of the coefficient of thermal expansion obtained in large volume press experiments [*Funamori and Yagi*, 1993; *Wang et al.*, 1994; *Utsumi et al.*, 1995] agree reasonably well with each other and the results of Raman spectroscopy measurements [*Chopelas*, 1996]. Secondly, such choice is supported by a statistical analysis of existing P-V-T data [*Jackson and Rigden*, 1996] and theoretical thermodynamic considerations [*Anderson et al.*, 1995; *Stacey*, 1996]. Besides, it has been suggested [*Wang et al.*, 1994] that the early measurements of expansivity of $(Mg,Fe)SiO_3$ may have been made outside the stability field and so may not be correct. Taking the huge uncertainty in measured values, we follow the approach of *Anderson et al.* [1995] and compute α from thermoelastic parameters [*Anderson and Masuda*, 1994] rather than use it as an input parameter. So the choice between the low and high values of α is, in fact, the choice between the values of the corresponding thermoelastic parameters.

The computation begins with the *Suzuki et al.* [1979] equation:

$$\frac{\triangle V}{V_0} = \frac{\left[1 + 2\tilde{k} - \left(1 - \frac{4\tilde{k}E_{TH}(\Theta/T)}{Q}\right)^{1/2}\right]}{2\tilde{k}a_v} - 1, \qquad (2.4)$$

where V_0 is the molar volume; $\tilde{k} = (1/2)(K'_T - 1)$, where $K'_T = \partial K_T/\partial P$ is the pressure derivative of the bulk modulus; $a_v = V(T_s)/V(0)$; $Q = K_{T_0}V_0/\gamma_0$, where K_{T_0} is the ambient isothermal bulk modulus, γ_0 is the ambient pressure Grüneisen ratio; $E_{TH}(\Theta/T)$ is the Debye energy and Θ is the Debye temperature. The temperature dependence of the ambient pressure coefficient of thermal expansion, $\alpha(P_0, T)$, is then obtained as a temperature derivative of (2.4).

After the values of K_S, G, and ρ at temperature T_f are known, their high pressure values can be calculated using the third-order Birch-Murnaghan equation of state [*Birch*, 1952]:

$$P = 3K_S(P_0, T_f)f(1 + 2f)^{5/2}\left(1 - \frac{3}{2}(4 - K'_S)f\right), \qquad (2.5)$$

where $f = \frac{1}{2}[\rho(P, T)/\rho(P_0, T_f)]^{2/3} - 1$ is the finite strain. Then the elastic parameters

of the adiabatically compressed material can be calculated as follows [*Sammis et al.*, 1970; *Davies and Dziewonski*, 1975]:

$$K_S(P,T) = K_S(P_0,T_f)(1+2f)^{5/2}[1+$$
$$(3K'_S-5)f] \tag{2.6}$$

$$G(P,T) = G(P_0,T_f)(1+2f)^{5/2}\{1+$$
$$[3G'K_S(P_0,T_f)/G(P_0,T_f)-5]f\} \tag{2.7}$$

$$\rho(P,T) = \rho(P_0,T_f)(1+2f)^{3/2}. \tag{2.8}$$

The elastic properties of the composite material are calculated by taking a Reuss-Voigt-Hill (RVH) average of the corresponding values for perovskite and magnesiowüstite:

$$M = \left\{ \frac{M_{\text{Pv}}M_{\text{Mw}}\left[\chi_{\text{Pv}}^{vol.}M_{\text{Pv}}+(1-\chi_{\text{Pv}}^{vol.})M_{\text{Mw}}\right]}{\chi_{\text{Pv}}^{vol.}M_{\text{Mw}}+(1-\chi_{\text{Pv}}^{vol.})M_{\text{Pv}}} \right\}^{1/2},$$

where M is either K_S, G or ρ and $\chi_{\text{Pv}}^{vol.}$ is the volume fraction of perovskite that can be calculated from the molar fraction χ_{Pv}.

The adiabatic temperature in the mantle is calculated using equation

$$\frac{dT}{dz} = \frac{T\gamma\rho g}{K_S}, \tag{2.9}$$

where γ is the Grüneisen parameter. It is generally accepted that the values of γ are not very sensitive to temperature above Θ [*Anderson*, 1988; *Anderson et al.*, 1996]. The effect of compression on γ is given by [*Anderson et al.*, 1993]

$$\gamma = \gamma_0\eta^q, \tag{2.10}$$

where $\eta = \rho(P_0,T_f)/\rho(P,T)$ and γ_0 is the value at $\eta = 1$. The dimensionless parameter q has values close to 1 for most minerals but is itself a function of pressure and temperature.

We separately calculate the Grüneisen parameters for perovskite and magne-

siowüstite and then take the RVH average to represent the Grüneisen parameter of the compound material which is used in the equation for temperature (2.9).

To calculate the coefficient of thermal expansion along the mantle adiabat, the calculated isobars $\alpha(P_0, T)$ must first be converted to isochores $\alpha(\eta = 1, T)$. This is done by integrating the identity

$$\left(\frac{\partial \alpha}{\partial T}\right)_V = \left(\frac{\partial \alpha}{\partial T}\right)_P - \bar{\delta}_T \alpha^2, \tag{2.11}$$

obtained by *Anderson and Masuda* [1994]. The Anderson - Grüneisen parameter, δ_T, varies with temperature below the Debye temperature (e.g., [*Isaak et al.*, 1990]), so we use the average value, $\bar{\delta}_T$, of the ambient and high temperature values in the equation above. After that the coefficient of thermal expansion at a given temperature, T, and compression, η, can be calculated using the following equation, obtained by *Anderson et al.* [1992]:

$$\alpha(T, \eta) = \alpha(T, \eta = 1) \exp\left[-\frac{\delta_{T_0}}{k}(1 - \eta^k)\right], \tag{2.12}$$

where δ_{T_0} is the high-temperature value of the Anderson - Grüneisen parameter at zero pressure, and k is a dimensionless thermoelastic parameter controlling the dependence of δ_T on compression [*Anderson and Isaak*, 1993]:

$$\delta_T = \delta_{T_0} \eta^k. \tag{2.13}$$

We use equations (2.12) and (2.13) to calculate α and δ_T, respectively, along the adiabat. The calculations are performed separately for perovskite and magnesiowüstite and a RVH average is taken to represent the lower mantle values.

The pressure dependence of the adiabatic Anderson - Grüneisen parameter, $\delta_S \equiv (\partial \ln K_S / \partial \ln \rho)_P$, has received significant attention recently. This parameter controls the sensitivity of the adiabatic bulk modulus, K_S, to temperature and is essential in evaluation of the temperature dependence of the compressional seismic velocity. The discussion on the matter was stimulated by an observation of apparent inconsistency of seismic tomography results with the mineral physics data that was first noted

by *Anderson* [1987] from the analysis of seismic velocities variation in tomographic models. The ratio of the relative shear velocity lateral variations to the compressional velocity variations, $(\partial \ln V_S / \partial \ln V_P)_P$, calculated from seismic tomography models, is about a factor of 2 larger than the estimates from zero-pressure mineral physics data, and the separate analysis of P and S velocity variations gives Γ values at the bottom of the mantle similar to the zero-pressure values (≈ 5.8), while it requires significantly lower values of δ_S (≈ 1.8) than the zero-pressure measurements (≈ 4.0) [*Anderson*, 1987].

The problem of δ_S pressure dependence was later addressed by *Agnon and Bukowinski* [1990] [1990] and *Isaak et al.* [1992]. Both studies provided further support for the relative insensitivity of Γ to pressure and a substantial decrease in δ_S.

Anderson [1967] showed an empirical relationship

$$\delta_S \approx \delta_T - \gamma, \tag{2.14}$$

valid for most minerals above the Debye temperature. From the analysis of the high temperature data on NaCl and KCl, *Yamamoto et al.* [1987] suggested that the following form of the relationship is more appropriate:

$$\delta_S \approx \delta_T - 1.4\gamma. \tag{2.15}$$

We use the relationship (2.15) to calculate δ_S along the adiabat. Parameter Γ is assumed to be constant along the adiabat and equal to 5.25, consistent with high-temperature values for MgO [*Isaak et al.*, 1989, 1992].

Following the described procedure, we calculate adiabatic profiles of K_S, G, ρ, T, α, γ, δ_T, and δ_S for a homogeneous lower mantle. Significant tradeoffs exist between the composition, foot temperature of the adiabat, T_f, and zero-pressure values of the coefficient of thermal expansion, α [*Bukowinski and Wolf*, 1990; *Hemley et al.*, 1992; *Stixrude et al.*, 1992; *Zhao and Anderson*, 1994; *Stacey*, 1996]. The coefficient of thermal expansion, in turn, depends on several thermodynamic parameters, of

which the most important are the Grüneisen ratio, γ, and the Anderson - Grüneisen parameter, δ_T [*Anderson et al.*, 1995; *Stacey*, 1996].

Parameters χ_{Pv}, χ_{Fe}, T_f were systematically varied in the limits $0.5 - 1.0$, $0.08 - 0.12$ and $1400 - 2100K$, respectively, in search for the best fit to PREM in the $800 - 2600$km depth range. The top and bottom regions of the lower mantle were excluded because the effects of non-adiabaticity may be significant (e.g., [*Butler and Anderson*, 1978]). The resulting preferred values are $\chi_{Pv} = 0.55$, $\chi_{Fe} = 0.11$ and $T_f = 1750K$, which are in agreement with the results of *Stacey* [1996]. However, this solution is obviously non-unique due to the existing tradeoffs and significant uncertainties in the values of input mineral physical properties and wide bounds of geochemical constraints. The corresponding profiles of density, ρ, and elastic moduli, K_S and G, are given in Figure 2.1 and the calculated seismic velocities

$$V_P = \sqrt{\frac{K_S + \frac{4}{3}G}{\rho}} \qquad (2.16)$$

and

$$V_S = \sqrt{\frac{G}{\rho}} \qquad (2.17)$$

are given in Figure 2.2. The modeling results (ρ, K_S and G) have systematically steeper slopes than PREM. Though this may be a drawback of the low-order equation of state, it does not necessarily imply that the calculated along an adiabat thermoelastic parameters are systematically wrong, since weakly super-adiabatic radial gradients of temperature cannot be ruled out for the lower mantle [*Bukowinski and Wolf*, 1990].

Several assumptions were used in the calculations. First, all parameters involved, except ρ and G, are probably not very sensitive to iron content [*Mao et al.*, 1991; *Wang et al.*, 1994]. So in most cases we used the properties of the Mg end members for both (Mg,Fe)O and $(Mg,Fe)SiO_3$ (Table 2.1). Second, we assumed non-equal partitioning of iron between magnesiowüstite and perovskite, consistent with the study of *Kesson and Fitz Gerald* [1992]. The iron partitioning coefficients for $(Mg,Fe)SiO_3$
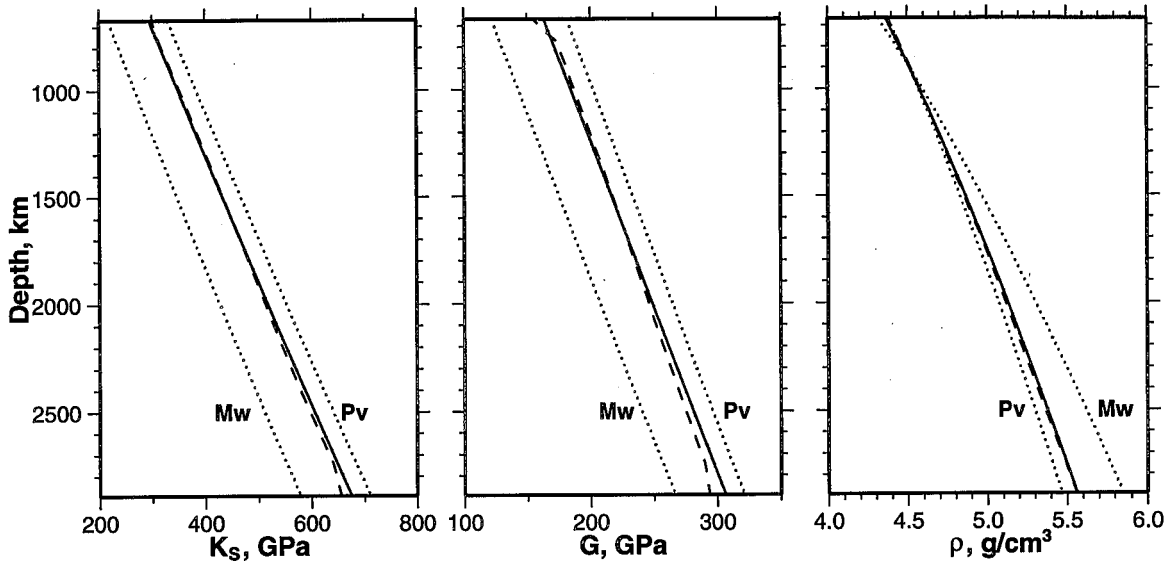
Figure 2.1: Elastic moduli and density calculated along a mantle adiabat. Dotted lines give values for magnesiowüstite and silicate perovskite; solid lines represent the RVH average values; dashed lines indicate PREM values for reference.
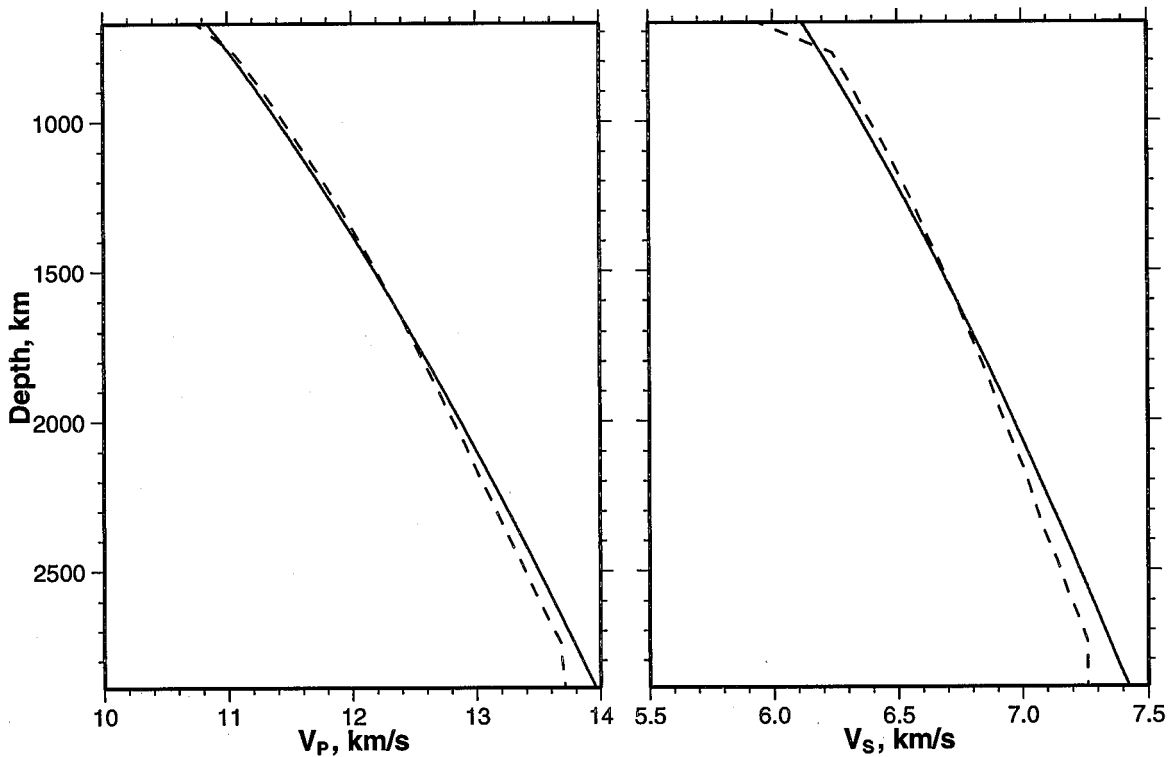
Figure 2.2: Seismic velocities calculated along a mantle adiabat. Solid lines represent the RVH average values; dashed lines indicate PREM values for reference.

Table 2.1: Thermoelastic parameters

Parameter	(Mg,Fe)O (mw)	(Mg,Fe)SiO$_3$ (pv)	SiO$_2$ (st)	Reference
V_0, cm^3	$11.25 + 1.0\chi_{\text{Fe}}^{\text{Mw}}$	$24.447 + 1.143\chi_{\text{Fe}}^{\text{Pv}}$	14.014	1, 2
K_{S_0}, GPa	$163 - 8\chi_{\text{Fe}}^{\text{Mw}}$	264	305	3, 4, 2
G_0, GPa	$131 - 77\chi_{\text{Fe}}^{\text{Mw}}$	177.3	217	3, 4, 2
K_S'	3.8[a]	4.0	5.3	5, 6, 2
G'	1.7[a]	1.6	1.8	5, 6, 2
Θ, K	945	1020	1192	7, 8, 3
γ_0	1.52	1.4	-	9, 8
δ_{T_0}	5.0	4.5	-	7, 8
$\bar{\delta}_T$	4.9	5.0	-	7, 8
$\bar{\delta}_S$	3.15	2.7	2.7[b]	7, 10
Γ	5.25	5.25[c]	5.25[c]	11
$\bar{\Gamma}$	5.1	5.1[c]	5.1[c]	7
k	$k(T)$[d]	1.5	-	12, 13
q	$q(\eta, T)$[e]	1	-	14, 8

References: 1, *Saxena* [1996]; 2, *Li et al.* [1996]; 3, *Duffy and Anderson* [1989]; 4, *Yeganeh-Haeri* [1994]; 5, *Isaak* [1993]; 6, *Zhao and Anderson* [1994]; 7, *Isaak et al.* [1989]; 8, *Anderson et al.* [1996]; 9, *Chopelas* [1996]; 10, *Bukowinski and Wolf* [1990]; 11, *Isaak et al.* [1992]; 12, *Anderson et al.* [1992]; 13, *Anderson and Masuda* [1994]; 14, *Anderson et al.* [1993].

[a] Calculated mid-mantle value is used.

[b] Assumed to be the same as for (Mg,Fe)SiO$_3$.

[c] Assumed to be the same as for MgO.

[d] A specific value is taken at any given temperature.

[e] A specific value is taken at any given compression and temperature.

and (Mg,Fe)O, respectively, were taken as $\chi_{\text{Fe}}^{\text{Pv}} = 0.07$ and $\chi_{\text{Fe}}^{\text{Mw}} = 1.727\chi_{\text{Fe}} - 0.016$ according to figure 2 of *Kesson and Fitz Gerald* [1992].

We neglected the possible effect of the presence of high-pressure phases of Al and Ca-bearing minerals. These are expected to be in small amounts and in perovskite structure with a minor effect on the properties of the lower mantle (e.g., [*Jeanloz and Knittle*, 1986; *Zhao and Anderson*, 1994]).

The isothermal bulk modulus, K_{T_0}, in equation (2.4) was calculated from the adiabatic bulk modulus:

$$K_T = K_S/(1 + \alpha\gamma T) \qquad (2.18)$$

and it was assumed that $K_T' \approx K_S'$ [*Anderson*, 1987; *Isaak*, 1993].

When calculating the pressure dependence of (2.10) and (2.13), we took into account the pressure and temperature effects on the values of parameter q [*Anderson et al.*, 1993] and temperature effect on the values of parameter k [*Anderson et al.*, 1992] for magnesiowüstite, while constant values of q and k were used for silicate perovskite due to the absence of data.

By taking a RVH average, we assumed that various properties of a composite material are bounded by the corresponding properties of the constituents. While this is true for density and elastic moduli [*Watt et al.*, 1976], this issue has not been thoroughly studied for the coefficient of thermal expansion, α, and the thermoelastic parameters δ_T and γ. *Anderson et al.* [1996] argued that γ of the magnesiowüstite-perovskite mix must be bounded by the corresponding values of the constituents. We expect this to be also true for the α and δ_T. The calculated values of δ_T, γ and δ_S along the lower mantle adiabat are given in Figure 2.3.

For a successful dynamic model, values of the coefficient of thermal expansion are required throughout the mantle. We used a function in the form

$$\alpha(z) = \frac{\alpha_0}{1 + az^b} \qquad (2.19)$$

to fit the calculated values of the coefficient of thermal expansion along the mantle adiabat (Figure 2.4). In equation (2.19) α_0 is the value of expansivity at zero depth, z is depth normalized by the radius of the Earth, and a and b are the fitting parameters to be determined. For the surface value of expansivity, α_0, we take the zero-pressure value of olivine at $T = 1750$K, which is about 4.5×10^{-5} K^{-1} [*Duffy and Anderson*, 1989]. The best fit is found for $a = 10.5$, $b = 0.85$.
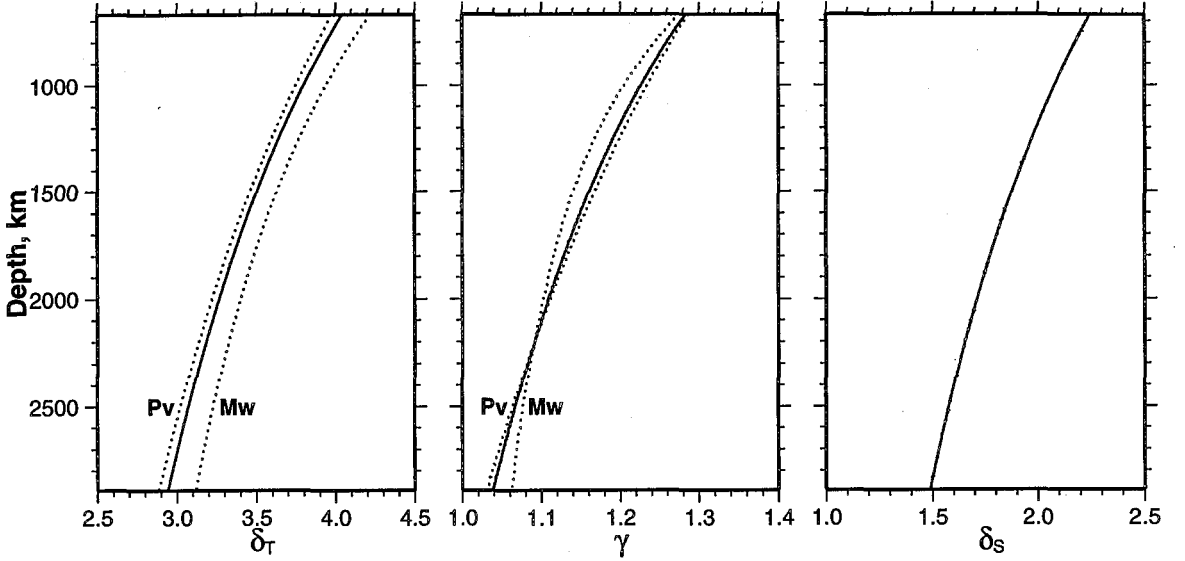
Figure 2.3: Thermoelastic parameters δ_T (left), γ (middle) and δ_S (right), calculated along a mantle adiabat. Dotted lines give values for magnesiowüstite and silicate perovskite; solid lines represent the RVH average values. The values of δ_S were calculated using equation (2.15).

2.4 Computing 2D velocity perturbations

To estimate the effect of the super-adiabatic temperatures and the inclusion of a distinct phase or chemically distinct material on the adiabatic 1D seismic velocities, we use a Taylor series expansion of equations (2.16) and (2.17) restricted to linear terms:

$$
\begin{aligned}
\triangle V_P &= \frac{\partial V_P}{\partial K_s} dK_s + \frac{\partial V_P}{\partial G} dG + \frac{\partial V_P}{\partial \rho} d\rho \\
&= \frac{\partial V_P}{\partial K_S}\left(\frac{\partial K_S}{\partial T} dT + \frac{\partial K_S}{\partial C} dC\right) \\
&\quad + \frac{\partial V_P}{\partial G}\left(\frac{\partial G}{\partial T} dT + \frac{\partial G}{\partial C} dC\right) \\
&\quad + \frac{\partial V_P}{\partial \rho}\left(\frac{\partial \rho}{\partial T} dT + \frac{\partial \rho}{\partial C} dC\right) \\
&= \frac{1}{2}\frac{K_{S_0}}{\rho_0 V_{P_0}}(\delta_S \alpha_0 \triangle T_{na} + (\epsilon_{K_S} - 1)C) \\
&\quad + \frac{2}{3}\frac{G_0}{\rho_o V_{P_0}}(\Gamma \alpha_0 \triangle T_{na} + (\epsilon_G - 1)C)
\end{aligned}
$$
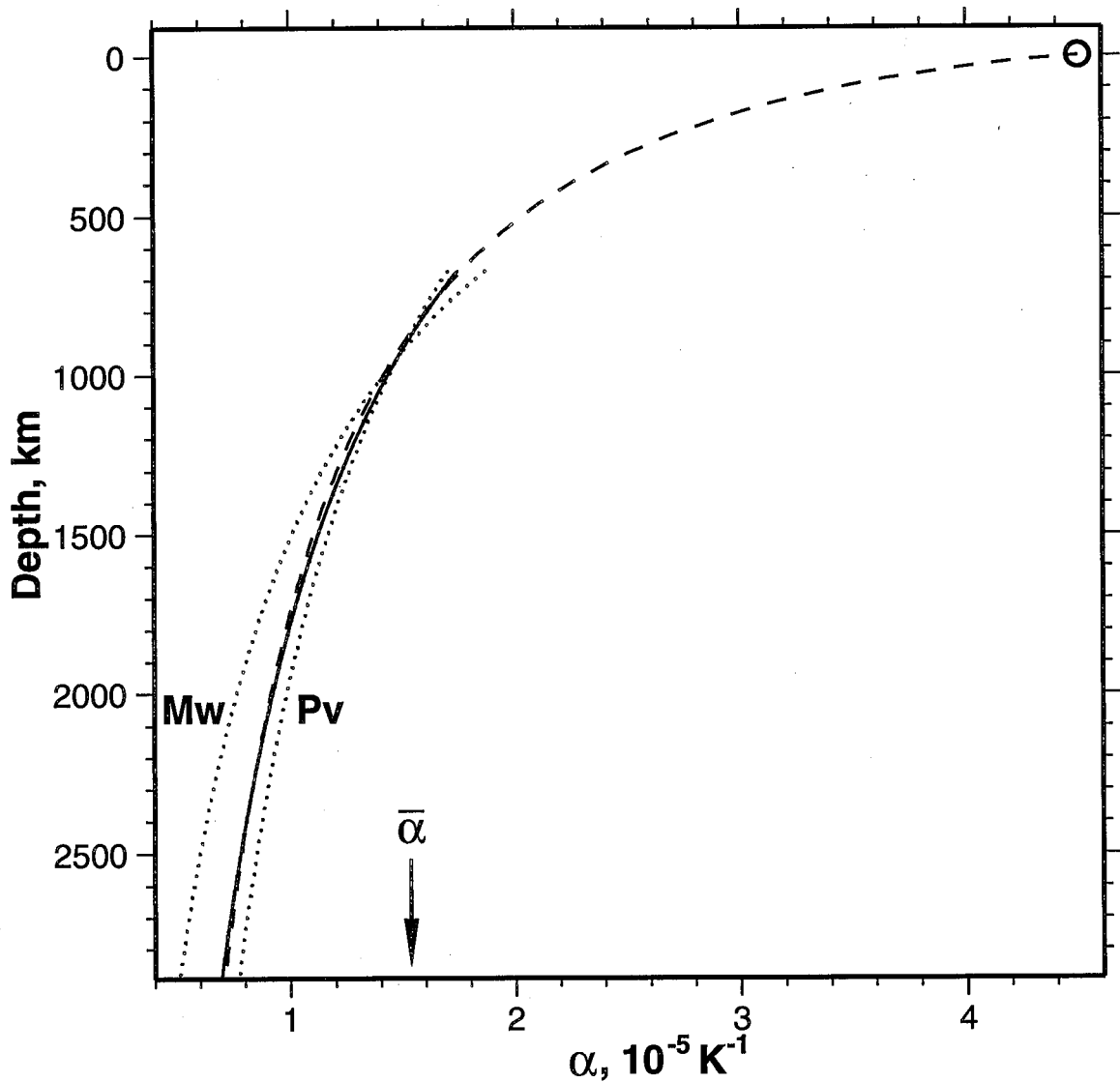
Figure 2.4: Coefficient of thermal expansion along a mantle adiabat. Dotted lines give values for magnesiowüstite and silicate perovskite; solid lines represent the RVH average values. The open circle represents the high-temperature value for olivine [*Duffy and Anderson*, 1989]. The dashed line gives the best fit using (2.19). The intercept on the horizontal axis shows the volume averaged value used in dynamic models.

$$-\frac{1}{2}V_{P_0}(\alpha_0 \triangle T_{na} + (\epsilon_\rho - 1)C) \, , \tag{2.20}$$

$$\triangle V_S = \frac{\partial V_S}{\partial G}dG + \frac{\partial V_S}{\partial \rho}d\rho$$

$$= \frac{1}{2}\frac{G_0}{\rho_o V_{S_0}}(\Gamma \alpha_0 \triangle T_{na} + (\epsilon_G - 1)C)$$

$$-\frac{1}{2}V_{S_0}(\alpha_0 \triangle T_{na} + (\epsilon_\rho - 1)C) \, , \tag{2.21}$$

where $\epsilon_\rho = \rho_d/\rho_a$, $\epsilon_{K_S} = K_{S_d}/K_{S_a}$, $\epsilon_G = G_d/G_a$ are the elastic parameters ratios of the distinct phase (chemically distinct material) and the ambient phase (ambient material), $\triangle T_{na}$ is the non-adiabatic temperature, C is the concentration of the distinct material and zero subscripts refer to the adiabatic 1D values. Values of δ_S at any given depth are taken consistent with the thermodynamic estimates along the adiabat (Figure 2.3). The value of Γ is assumed to be constant with depth and equal to 5.25.

The non-adiabatic temperature, $\triangle T_{na}$, and the concentration of the distinct material, C, are obtained from the convection simulation. The non-adiabatic temperature is calculated as

$$\triangle T_{na} = T - T_f, \tag{2.22}$$

where T_f is the foot temperature of the adiabat and T is the temperature from convection computations.

Chapter 3   Dynamics of a Chemical Layer at the Base of the Mantle

3.1   Abstract

Constraints provided by the adiabatic model computed in Chapter 2 are used in convection models to study dynamics of a chemically distinct layer at the bottom of the mantle. We find that the layer must be at least 2% denser than the overlying mantle to survive for geologically significant periods of time. Realistic decrease with depth of the thermal expansivity increases layer stability but is unable to prevent it from entrainment. Seismic velocities are computed for an assumed composition by applying the thermal and compositional perturbations obtained in convection simulations to the adiabatic values. The predicted velocity jump at the top of the chemical layer is closer to the CMB in the cold regions than in the hot. The elevation of the discontinuity above CMB in the cold regions decreases with increasing thermal expansivity and increases with increasing density contrast, while in the hot regions we find that the opposite is true. If the density contrast is small, the layer may vanish under downwellings. However, whenever the layer is present in the downwelling regions, it also exists under the upwellings. For a 4% density contrast and realistic values of expansivity, we find that the layer must be more than 400 km thick on average to be consistent with the seismically observed depth of the discontinuity. A simple chemical layer cannot be used to interpret the D" discontinuity: the required change in composition is large and must be complex, since enrichment in any single mineral probably cannot provide the required impedance contrast. A negative velocity gradient produced by thermal gradients at the material interface in downwelling regions would weaken the seismic triplication and requires a higher shear velocity contrast for the basal material than regional seismic 1-D reference models suggest. A simple

chemical layer cannot explain the spatial intermittance of the discontinuity.

3.2 Introduction

In this chapter we study the dynamics of a chemically distinct layer at the bottom of the mantle and explore the conditions under which such layer would survive for extended periods of time. Then we determine the properties of this layer which are consistent with fundamental seismological observations of the CMB region.

A convection model is formulated with a bottom layer of specified physical properties. The convection in the mantle is simulated numerically using parameters consistent with the adiabatic 1D model computed in Chapter 2 and the corresponding properties (such as density) of the bottom layer. The temperature field and the spatial distribution of the distinct material, obtained from the simulation, are used to adjust the adiabatic elastic parameters to account for the effects of non-adiabaticity. This approach provides a dynamically consistent two-dimensional field of seismic velocities. Thus, the calculated seismic velocities are closely linked to the geodynamic model through the adiabatic 1D parameters and properties of the distinct material.

3.3 Geodynamic Model

Thermo-chemical convection with two materials, each with distinct properties, is computed in a 2D cylindrical coordinate system (r, ϕ) for a variety of cases. An incompressible flow model (Boussinesq approximation) is used in the simulation. The system is governed by the following non-dimensional equations [*Zhong and Gurnis*, 1993], representing conservation of momentum

$$\nabla \cdot (\mu \nabla \boldsymbol{u}) = -\nabla p + \frac{1}{\zeta^3}\alpha(r)Ra\left(T - \frac{1}{\alpha(r)}B\,C\right)\hat{\boldsymbol{r}}\,, \qquad (3.1)$$

energy

$$\frac{\partial T}{\partial t} = -(\boldsymbol{u} \cdot \nabla)T + \nabla^2 T + H\,, \qquad (3.2)$$

Table 3.1: Values of parameters used in convection simulation

Parameter	Symbol	Value
Radius of the Earth	R_0	6371 km
Depth of the CMB	D	2891 km
Gravity acceleration	g	10 m/s^2
Average mantle density	ρ_0	4.0 g/cm^3
Average mantle viscosity	$\bar{\mu}$	10$^{21.5}$ Pa·s
Thermal diffusivity	κ	10^{-6} m^2/s
Average thermal expansivity	$\bar{\alpha}$	1.535×10^{-5} K^{-1}
Temperature increase across the mantle	$\triangle T$	2900 K
Maximum velocity of subducting plate	U_{plate}	5 cm/yr
Maximum trench migration velocity	U_{trench}	0.5 cm/yr

and mass

$$\nabla \cdot \boldsymbol{u} = 0. \tag{3.3}$$

In the above equations, $\hat{\boldsymbol{r}}$ is a unit vector in the radial direction, r is dimensionless radius, $\boldsymbol{u}$ is dimensionless velocity, p is dimensionless pressure, T is dimensionless temperature, t is dimensionless time, and ζ is dimensionless depth of the core-mantle boundary. These parameters are related to the corresponding dimensional values by means of the following scalings (asterisk denotes dimensional values):

$$r^* = R_0 r, \tag{3.4}$$

$$\boldsymbol{u}^* = \frac{\kappa}{R_0} \boldsymbol{u}, \tag{3.5}$$

$$p^* = \frac{\kappa \bar{\mu}}{R_0^2} p, \tag{3.6}$$

$$T^* = T_S + \triangle T\, T, \tag{3.7}$$

$$t^* = \frac{R_0^2}{\kappa} t, \tag{3.8}$$

where R_0 is the radius of the Earth, κ is the thermal diffusivity, $\bar{\mu}$ is the volume averaged mantle viscosity, T_S is the temperature at the surface, and $\triangle T$ is the temperature increase across the mantle (Table 3.1).

Dynamic viscosity, μ, and coefficient of thermal expansion, α, in equation (3.1) are non-dimensionalized using the volume averaged values as characteristic scales:

$$\mu^* = \bar{\mu}\mu, \tag{3.9}$$

$$\alpha^* = \bar{\alpha}\alpha, \tag{3.10}$$

where $\bar{\mu}$ and $\bar{\alpha}$ are volume averaged viscosity and expansivity of the mantle, respectively. We take $\bar{\mu} = 10^{21.5}$ Pa·s, consistent with the inversion results of *Mitrovica and Forte* [1997]. The value of the volume averaged coefficient of thermal expansion, $\bar{\alpha}$, is calculated from the 1D adiabatic model presented above. In terms of the dimensionless radius, r, the depth dependence (2.19) of α can be written as:

$$\alpha(r) = \frac{4.5 \times 10^{-5}}{1 + 10.5(1 - r)^{0.85}}. \tag{3.11}$$

Taking the volume average, we have:

$$\bar{\alpha} = \frac{1}{V} \iint \alpha \, dV = 1.535 \times 10^{-5} K^{-1}. \tag{3.12}$$

For the purpose of convenience we will drop the '$*$' for dimensional values in all consequent equations.

The effects of internal heating are not addressed in this study and only bottom-heated models are considered, so that $H = 0$ in (3.2). Dimensionless parameter Ra in (3.1) is the thermal Rayleigh number which characterizes the vigor of convection in such a system. It is given by

$$Ra = \frac{g\bar{\alpha}\rho_0 \triangle T D^3}{\kappa\bar{\mu}}, \tag{3.13}$$

where g is the gravitational acceleration, ρ_0 is the density of the ambient material, and D is the depth of the core-mantle boundary. The anomalous material has density $\rho_0 + \triangle\rho_0$ and its distribution is described by the composition function, $C(r, \phi)$, which takes values from 0 (ambient material) to 1 (anomalous material). The effect of

the introduced anomalous material on the flow is characterized by the compositional Rayleigh number, Ra_c, given by:

$$Ra_c = \frac{g\triangle\rho_0 D^3}{\kappa\bar{\mu}}.$$ (3.14)

Parameter B in (3.1) is the ratio of the two Rayleigh numbers, $B = Ra_c/Ra$. It characterizes the relative importance of the compositional and thermal buoyancy forces and is given by

$$B = \frac{\triangle\rho_0}{\rho_0\bar{\alpha}\triangle T}.$$ (3.15)

The model domain is represented by a half-annulus (Figure 3.1) with the inner radius corresponding to the core-mantle boundary and the outer radius corresponding to the surface of the Earth. Plates are modeled by imposing velocity boundary conditions on the top, as shown in Figure 3.1a. Free slip conditions are used at the bottom and side walls of the domain. The value of imposed surface velocity was determined from a free-slip calculation with no temperature dependent viscosity to ensure that the plate neither speeds up nor slows down the flow from what would be expected in convection with a free slip top [*Gurnis and Davies*, 1986]. A velocity overshoot is added in the back-arc basin to initiate subduction and prevent the slab from being sucked up under the overriding plate [*Christensen*, 1996a; *Davies*, 1997]. The trench migration velocity, U_{trench}, equal to the velocity of the overriding plate, is set to 10% of the surface velocity, U_{plate}, of the subducting plate.

The temperature is initially uniform throughout the interior of the mantle with superimposed top and bottom thermal boundary layers. The bottom boundary layer is 100 million years old. The thermal boundary layer for oceanic lithosphere is calculated using an infinite half-space cooling model with a velocity of $U_{plate} = 5$ cm/yr. The age of the lithosphere at the initial trench location is about 160 million years. To facilitate the detachment of the sinking slab from the overriding plate, the temperature on top of the overriding plate is set to the mantle interior temperature [*Christensen*, 1996a; *Davies*, 1997]. The temperature variation across the bottom thermal boundary layer is taken equal to the variation across the lithosphere. The
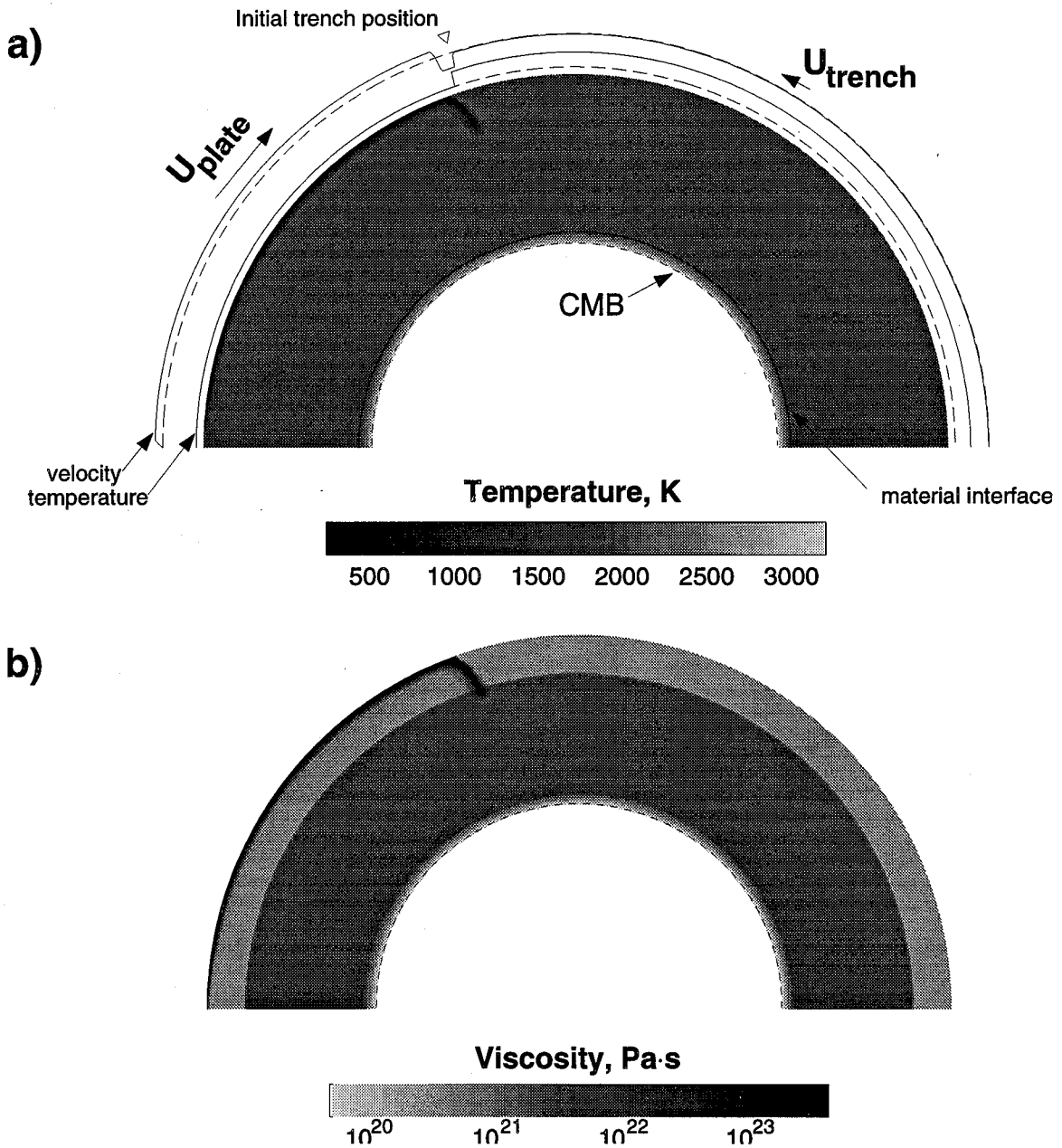
Figure 3.1: Dynamic model setup. a) Temperature field after 100 million years — just as the slab penetrates into the lower mantle. The value of the velocity overshoot in the back-arc region was scaled by a factor of 0.5 to give a clearer view of imposed plate velocities. b) Viscosity after 100 million years.

temperature in the mantle interior should correspond to the foot temperature of the mantle adiabat, $T_f = 1750K$, calculated above. This constraint and the choice of temperature variation across the bottom thermal boundary gives the value of the non-adiabatic temperature increase across the mantle, $\triangle T = 2900K$.

The imposed velocity of the subducting plate linearly increases from $0.05 U_{plate}$ to U_{plate} over a time of 190 million years, roughly the time it takes the slab to reach the bottom of the mantle with such a velocity. Accordingly, the velocity of the overriding plate, which is equal to the velocity of the trench, increases from $0.05 U_{trench}$ to U_{trench} over the same time interval. Such a gradual increase in imposed velocity helps to initiate subduction and is well justified physically, since the driving buoyancy force gradually increases with the increasing volume of subducted material. This is also consistent with a fully dynamic model of oceanic plates where plate margins are modeled with faults and surface velocities are model outcomes [*Zhong and Gurnis*, 1995].

A layer of distinct material with initial thickness d_0^{layer} is introduced at the bottom of the mantle. The material interface is initially represented by a chain of $N = 2000$ particles, extending from the left side-wall to the right. Each particle is a passive tracer and is characterized by its coordinates $(r_i^{int}, \phi_i^{int})$ in the system. Though this chain is not closed, the no-flux conditions at the bottom and the side-walls produce an effectively all-encompassing boundary. At any time a point lying above the chain is assumed to have an ambient composition, while a point lying below the chain is assumed to have a distinct composition.

The temperature and depth dependence of the dimensionless viscosity, μ, is given by

$$\mu = A\mu_0(r) \exp\left\{ \frac{c_1}{c_2 + \theta} - \frac{c_1}{c_2 + 0.5} \right\}. \tag{3.16}$$

The depth dependent part, $\mu_0(r)$, includes a factor of 10 increase across the 670 km depth:

$$\mu_0(r) = \begin{cases} 1 & \text{if } r > 0.89 \\ 10 & \text{if } r < 0.89. \end{cases} \tag{3.17}$$

Parameters c_1 and c_2 in (3.16) control the range of viscosity variation with temperature and the stiffness of the cold slab. We use $c_1 = 17.22$, which corresponds to an activation energy of 415 kJ·mol^{-1}, and $c_2 = 0.64$. A cutoff value of 10^3 is used. These parameters lead to 3 orders of magnitude in viscosity variation due to the temperature variations across the top boundary layer and another 2 orders of magnitude due to temperature variations in the bottom boundary layer.

The normalization parameter A in (3.16) is chosen so that the following equality holds when averaged over the entire duration of the simulation:

$$\frac{1}{V} \iint \log \mu \, dV = 0, \tag{3.18}$$

where V is the volume of the model domain. We find $A \approx 0.16$. Figure 3.1b shows viscosity of the flow as the slab penetrates into the lower mantle.

Equations (3.1)-(3.3) are solved using a finite-element code ConMan [*King et al.*, 1990], as modified by *Zhong and Gurnis* [1993] for a cylindrical geometry. The finite elements mesh has 300 elements in the azimuthal direction and 100 elements in the vertical. The mesh is refined both vertically and horizontally to increase the resolution in the thermal boundary layers and in the area of subduction.

The particles in the chain, representing the material interface, are advected using a third-order accurate predictor-corrector method. Whenever the distance between two adjacent particles exceeds a specified limit, δ_{max}, a new particle is introduced into the chain and placed between the two particles, so that the resolution of the boundary never falls below δ_{max}. In our calculations we use $\delta_{max} = 13$ km. An integration routine is used to calculate the ratio of each material in the finite element mesh. The associated compositional buoyancy is then fed back into the momentum equation (3.1). The accuracy of the material tracking algorithm was tested using steady-state divergence free analytic stream functions. The relative change in the volume, occupied by the distinct material, did not exceed 1% after two overturn times, which is quite satisfactory for our purposes.

Table 3.2: Computed thermo-chemical convection models

Convection Model	α	d_0^{layer}, km	$\triangle\rho_0/\rho_0$	$\triangle d_{RMS}(400\text{Ma})$, km
M1	constant	200	0%	2750
M2	variable	200	0%	2017
M3	constant	200	1%	1622
M4	variable	200	1%	521
M5	constant	200	2%	346
M6	variable	200	2%	147
M7	variable	200	3%	118
M8	constant	200	4%	154
M9	variable	200	4%	103
M10	variable	400	4%	114
M11	variable	200	5%	91
M12	variable	200	6%	78

[a] For models with variable α the depth dependence of the coefficient of thermal expansion is consistent with the adiabatic 1D calculations (3.11). For constant α cases the volume averaged value of α, given by (3.12) is used.

With all obvious limitations, introduction of compositional buoyancy into a convective system by means of a particle chain provides a nearly perfect resolution of the material interface, unlike solving an advective-diffusion equation or tracer particle methods. This jump in properties is essential for modeling seismic discontinuities. Moreover, the method does not seem to be vulnerable to the spurious settling problem encountered in various studies for the tracer particle techniques [*Gurnis*, 1986; *Christensen and Hofmann*, 1994; *van Keken et al.*, 1997].

We compute 12 different models of thermo - chemical convection, varying in the form of depth dependence of the coefficient of thermal expansion, $\alpha(r)$, the properties of the material in the bottom layer and the layer thickness, d_0^{layer} (Table 3.2). All studied cases have the same average thermal Rayleigh number. This is ensured by the normalization of the non-dimensional coefficient of thermal expansion, requiring its volume average to be 1. In models with depth dependent thermal expansivity, α varies with depth according to the adiabatic 1D model (3.11).

3.4 Results

The convection simulations have been integrated for 400 million years in each case. We now discuss the details of the results for a nominal case M9 with $\triangle\rho/\rho = 4\%$ and α varying with depth according with (3.11). The slab starts its descent into the lower mantle at a very steep dip angle and stays almost vertical until its tip reaches the bottom. After that the lower part of the slab levels off and continues along the top of the bottom layer. The dip of the slab is reduced and some folding occurs. The slab has a substantial influence on the morphology of the bottom layer, depressing the material below and pushing it aside, towards the upwelling regions. This results in significant topography of the material interface, which is raised in the upwelling regions on both sides of the slab and depressed below the slab.

Results of the convection simulations for models M1, M2, M9 and M10 after 400 million years are given in Figure 3.2. In order to estimate the influence of model parameters (α, B, and d_0^{layer}) on the morphology of the bottom layer, we computed the RMS topography of the layer for all model cases, using

$$\triangle d_{RMS} = \left[\frac{1}{N}\sum_{i=1}^{N}\left(r_i^{\text{int}} - d_0^{\text{layer}} - R_0 + D\right)^2\right]^{\frac{1}{2}}. \tag{3.19}$$

The parameter $\triangle d_{RMS}$ characterizes the radial disturbance of the layer and is equal to zero for a uniform layer and increases with topography. The values of $\triangle d_{RMS}$ for all cases after 400 million years are given in Table 3.2. Figure 3.3 gives the dependence of $\triangle d_{RMS}$ on the thermal expansion and the density contrast of the bottom material.

The topography of the layer is significantly reduced when the value of α at the bottom of the mantle is decreased. However, the effect of α on the slab dynamics is minor. This is most likely due to the imposed surface velocity conditions, that dominate the dynamics in the upper parts of the mantle, and the character of the depth dependence of α, that falls off fast in the upper 1/3 of the mantle and then
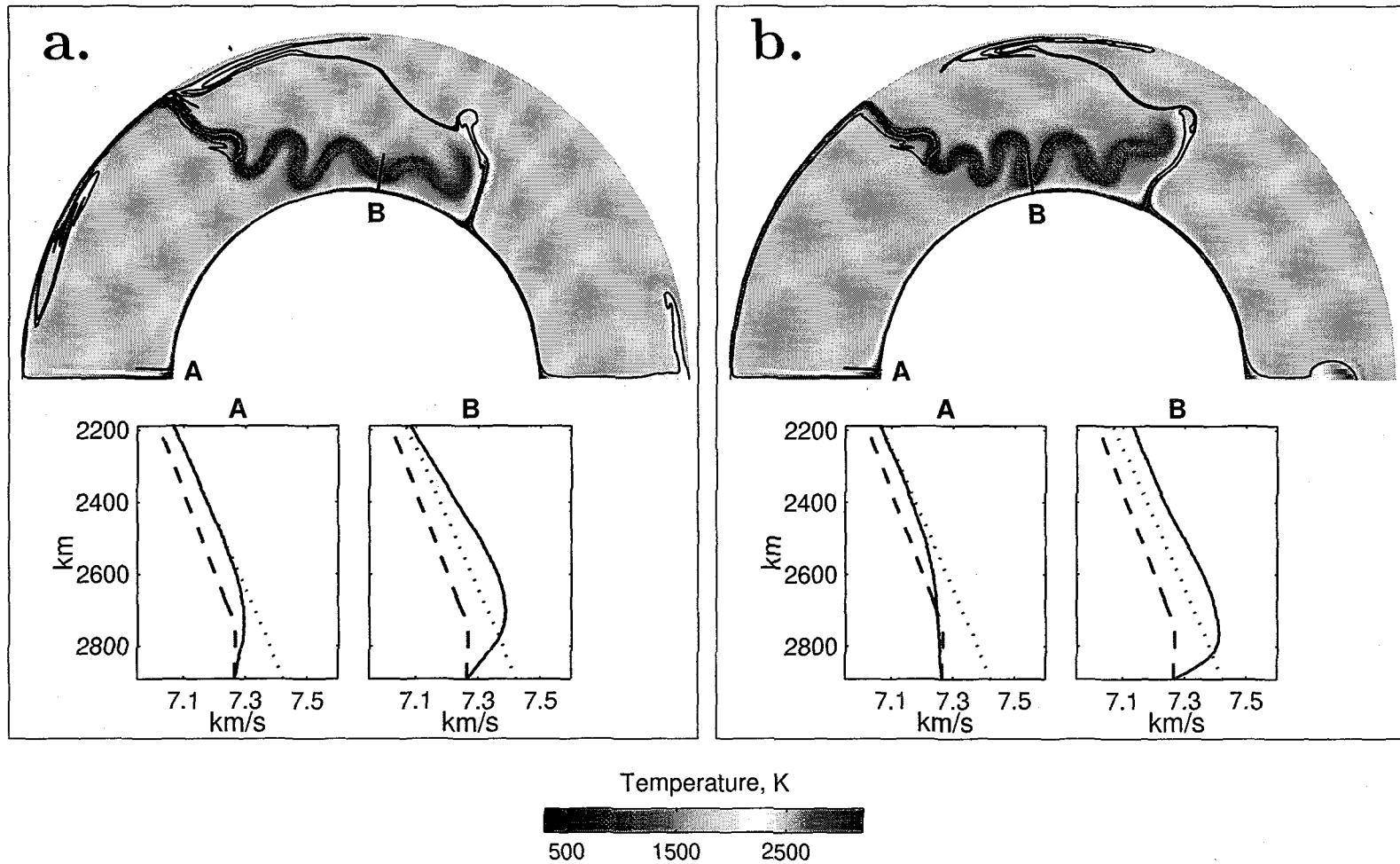
Figure 3.2: Four cases of convection simulation after 400 million years. Top panels show the temperature field and material interface (thin solid line). The core-mantle boundary is outlined by a dashed line. Bottom panels present seismic velocities (red solid lines) computed for the cross-sections indicated in the top panels. Cross-sections labeled 'A' correspond to upwelling regions, 'B' - to downwelling regions. The adiabatic 1D model (green dotted lines) and PREM values (blue dashed lines) values are given for reference.

a — model M1; b — model M2. The basal material is assumed to be identical to the overlying mantle for these two models.
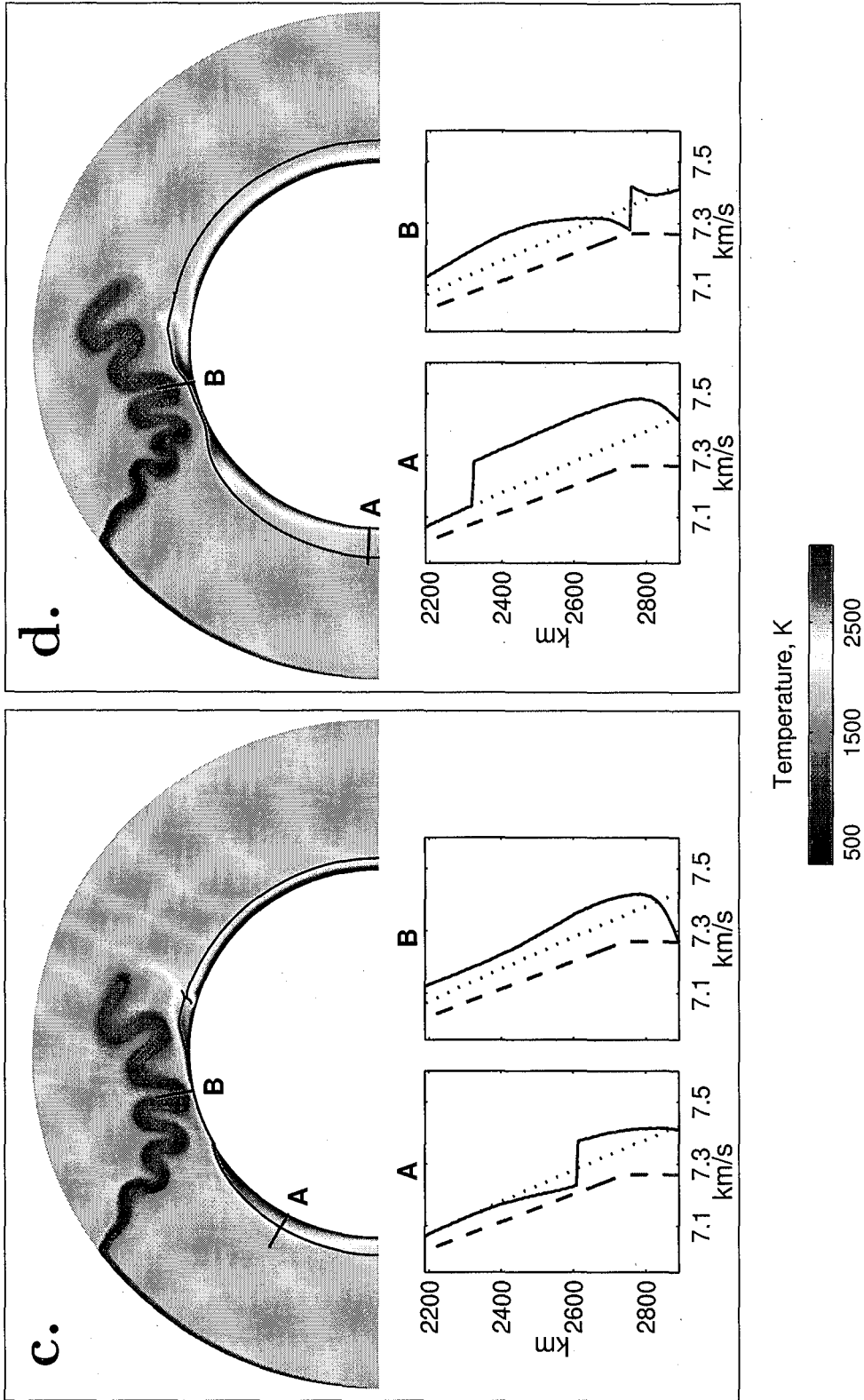
Figure 3.2 (*continued*): **c** — model M9; **d** — model M10. A stishovite and iron enriched basal chemical layer is assumed for these two models (composition indicated by a triangle in Figure 3.5).
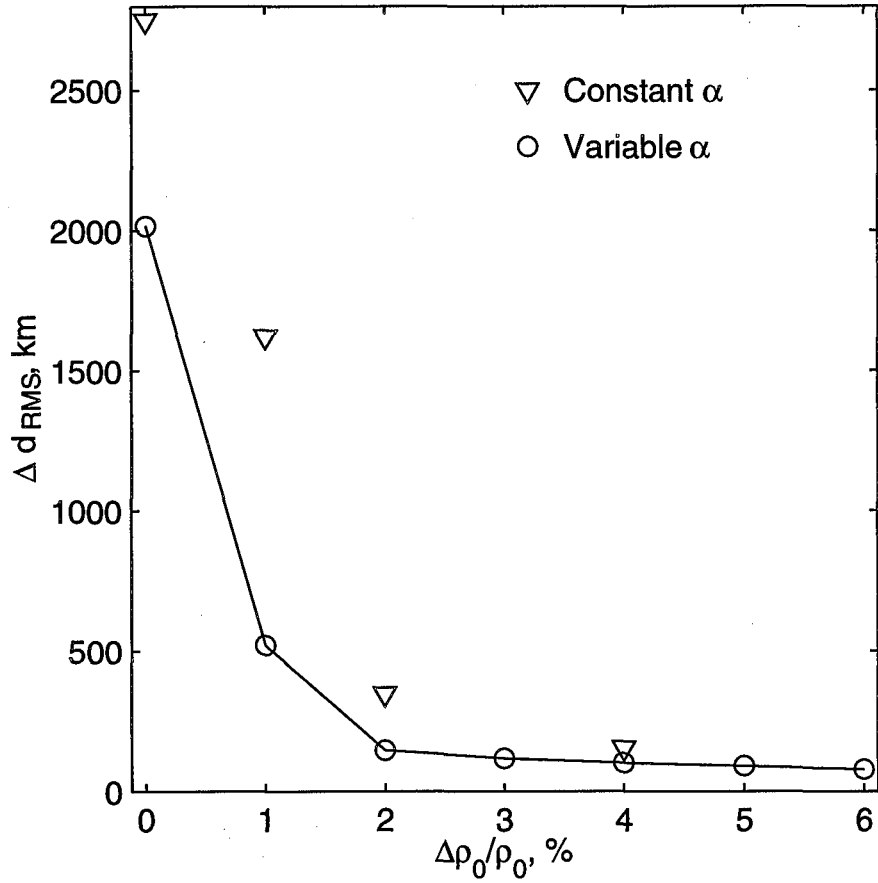
Figure 3.3: Radial RMS disturbance of the material interface after 400 million years. Circles represent models with the coefficient of thermal expansion varying with depth according to the adiabatic 1D model. Triangles correspond to models with constant α.

moderately decreases at greater depth. The result of the α normalization used in the models is that the constant α cases have values of α corresponding to about 900 km depth in cases with variable α (Figure 2.4). So while the total depth variation of α is about a factor of 6.5 throughout the mantle, the bottom values of the thermal expansivity for cases with constant and variable α differ only by a factor of 2.2.

As Figure 3.3 shows, the stability of the layer dramatically increases when its density anomaly increases to about 2%. In all cases with $\triangle\rho_0/\rho_0 < 2\%$ most of the bottom layer was already destroyed after 400 million years of integration through entrainment of the material by plumes. Though smaller values of α increase the survival time of the layer, the decrease in α alone, without a density anomaly in the bottom material, is not able to keep the layer intact for long periods.

Figure 3.4 gives the values of $\triangle d_{RMS}$ as a function of time for six different cases. The topography of the material interface is controlled by two opposing processes. In subduction areas, the weight of the cold slab and the stress transmitted by the slab from the surface tend to depress the material boundary. Away from the slab, in the upwelling regions, the growing bottom thermal boundary layer increases the thermal buoyancy of the material, tending to elevate the boundary. The topography rapidly increases for about 100-200 million years as the slab descends to the bottom of the mantle and depresses the chemical layer. Then topography stays approximately constant for some time until the layer heats up and thermal buoyancy becomes substantial. A 1% chemical density contrast is obviously not enough to balance this buoyancy and the basal material is rapidly entrained by the upwellings after about 300 million years of model integration. For a 2% density contrast, at least after the period of integration used in our study, the layer survives at the bottom. However, all the material is swept towards the upwelling regions away from the core-mantle boundary below the slab.

As the integration continues, the slab starts to buckle, reducing the stress transmitted downwards and producing periodic in time topography with a period approximately equal to the period of buckling. To the left of the slab the topography is dominated by the thermal buoyancy of the basal material and is the highest. Several
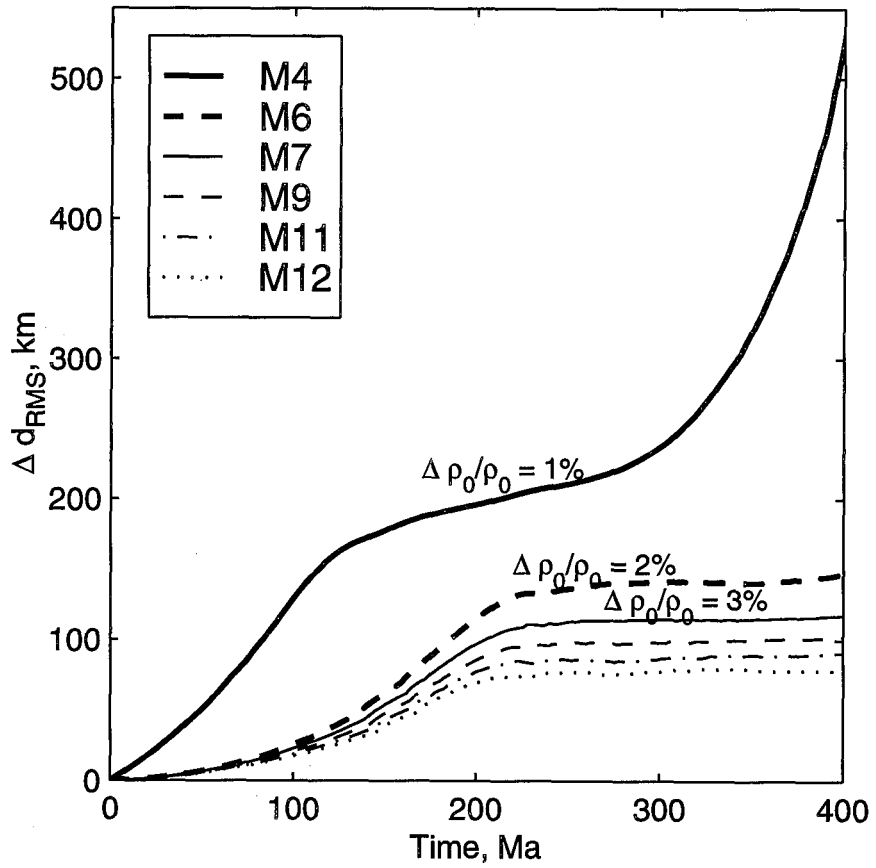
Figure 3.4: Disturbance of the basal layer as a function of time.

thousand kilometers to the right of the trench, where the slab rests on top of the basal layer, practically no stress is transmitted from the surface, and the weight of the slab opposes the buoyancy force of the hot bottom material. The topography in these regions is moderate.

The net effect of the processes on the layer morphology strongly depends on the density of the basal material. Figure 3.3 shows that topography for both models with a density contrast of 2% (M3 and M6) persistently decreases after reaching its maximum, while for the cases with $\triangle\rho_0/\rho_0 = 1\%$ (M7 and M10) the topography shows a trend for increase after about 370 million years. This means that at least 2% density contrast is required to keep a chemical layer stable at the bottom of the mantle. By keeping track of the material interface, we do not allow any mixing of the two materials. If such mixing takes place, a material with intermediate density may be produced, thus requiring even higher initial density contrasts for the layer stability.

An interesting change in dynamics occurs when the thickness of the layer is increased and a sufficient density contrast is applied. With an initial thickness of 400 km and a density contrast of 4% the slab fails to thin the layer significantly. The increased temperature drop across the bottom thermal boundary layer has a destabilizing influence [*Lenardic and Kaula*, 1994] and leads to the initiation of an upwelling below the slab (Figure 3.2d). This initiated upwelling increases the buoyancy of the layer below the slab, thus partially reducing the depression of the interface. However, this buoyancy increase is unable to reverse the effect of the slab and produce elevated topography below the slab.

The bottom panels in Figures 3.2 show seismic velocities through the radial profiles indicated in the top panels. The values of the adiabatic 1D velocities were corrected for the effects of temperature and chemistry using the procedure presented in Section 2.4. For cases M1 and M2 ($\triangle\rho_0/\rho_0 = 0$) the composition of the basal layer was identical to the overlying mantle ($\epsilon_\rho = 1$, $\epsilon_{K_S} = 1$, $\epsilon_G = 1$). For cases M9 and M10 ($\triangle\rho_0/\rho_0 = 4\%$) a distinct composition was assumed for the basal layer, with $\epsilon_\rho = 1.04$, $\epsilon_{K_S} = 1.047$ and $\epsilon_G = 1.079$. This choice of the properties of the basal

layer and the corresponding composition will be discussed below.

We will first discuss cross-sections in the downwelling regions (cross-sections labeled 'B'). For all models, except M10, where the layer was initially 400 km thick, V_S remains nearly adiabatic down to a depth of about 2200 km, where it starts to increase due to the slab thermal anomaly. In model M10, the slab rests higher in the mantle, since the thickness of the bottom chemical layer is higher. The shear velocity for this case starts to deviate from its adiabatic values at about 2000 km depth. The fast velocity anomaly then continues to increase with depth, reaching its maximum at depth of 2200-2500 km, corresponding to the middle of the slab. At greater depths the trend reverses and V_S returns to its adiabatic values. Both the increase and decrease take place over a depth range of about 200 km, as the slab is diffuse. Following the attainment of adiabatic values, velocity starts to decrease with a large gradient due to the super-adiabatic temperatures of the bottom thermal boundary layer. In model M10 (Figure 3.2d) a discontinuous velocity increase by about 2% occurs at the top of the layer in the region of a negative velocity gradient. The elevation of this discontinuity above the CMB is about 150 km. For models with $\triangle\rho_0/\rho_0 < 4\%$ and $d_0^{\text{layer}} = 200$ km no discontinuity is observed as the layer vanishes below the slab.

In the upwelling regions (cross-sections labeled 'A'), V_S remains adiabatic down to depth of about 2500 km. It then starts to decrease because of the super-adiabatic temperatures of the bottom thermal boundary layer. A discontinuous increase by about 2% occurs at the top of the chemical layer in models M9-M10. The elevation of the discontinuity above the CMB is about 290 km for model M9 and about 590 km for model M10 — much higher than for the downwelling regions.

Lower basal values of α increase the height of the discontinuity in the downwelling regions, while decreasing it in the upwelling regions. The influence of the density contrast increase is similar to the influence of α reduction. In terms of providing a given topography in the downwelling regions, a tradeoff exists between the layer density contrast, its average thickness, and the basal values of α. Although a 2% density contrast may be sufficient to prevent the layer from entrainment, a higher density contrast and a thickness of more than 200 km are required to ensure that the

layer does not vanish in the downwelling regions. An interesting implication of the dynamics of such systems is that if the layer survives for significant periods of time it becomes hot. This leads to high temperature gradients across the material interface in the downwelling regions, so that the discontinuous seismic velocity change occurs in the area of negative velocity gradient.

3.5 Discussion

A chemical layer at the bottom of the mantle has been proposed in several studies (e.g., [*Davies and Gurnis*, 1986; *Christensen and Hofmann*, 1994; *Wysession*, 1996]) as causing the seismic discontinuity at the top of D". Using both previous and new results, is such an interpretation of the seismology consistent with the dynamics of the mantle and mineralogical and geochemical constraints?

Seismic body waves have been interpreted in terms of a $2 - 3\%$ discontinuous velocity increase 150 to 350 km above the core-mantle boundary with a median height of 250 km in many regions of the world [*Loper and Lay*, 1995; *Lay et al.*, 1998]. There are, however, reports of the height of the discontinuity as low as 130 km [*Vidale and Benz*, 1993] and as high as 450 km [*Kendall and Shearer*, 1994]. One of the controversial issues about the discontinuity is the problem of its intermittent nature (see discussion by *Loper and Lay* [1995]). It is still not clear if the discontinuity is a global feature [*Nataf and Houard*, 1993] or if it only exists in some places in the world. The discontinuity has been observed in most seismically fast (cold) regions at the base of the mantle, but it has also been reported in some slow (hot) regions [*Kendall and Shearer*, 1994]. While it is still difficult to make firm conclusions about the correlation of the discontinuity with the location of upwelling and downwelling regions, an interpretation of this velocity jump should be able to provide some explanation to the absence of the discontinuity in seismically slow regions and why its detection in those regions would be complicated.

Dynamics of a dense layer at the base of a convection system has previously been studied [*Davies and Gurnis*, 1986; *Gurnis*, 1986; *Hansen and Yuen*, 1989; *Olson*

and Kincaid, 1991]. All of the previous studies and our new work demonstrate the same qualitative influence of convection on the morphology of the layer. The layer is depressed below the cold downwellings and is swept towards hot regions where it may or may not be entrained by the upwellings. Independent of the layer formation, all dynamic models predict that the layer would be thinnest in the downwelling regions and thickest below the upwellings. This means that if the seismic discontinuity in D" occurs on top of a chemical layer, this layer must be at least 200-250 km thick since this is the height of the observed velocity jump in most seismically fast regions and regions which are most likely regions of downwelling.

If a layer of sufficient thickness is formed at the bottom of the mantle, under what conditions would the layer survive for a geologically long time without substantial recharge? This problem was studied by *Davies and Gurnis* [1986] in convection models with constant viscosity. It was found that an initially 300 km thick layer which is 2-3% heavier than the surrounding mantle would survive for at least 250 million years. Laboratory experiments [*Olson and Kincaid*, 1991] suggest that at least 2% density anomaly is required to prevent the layer from immediate overturn. A layer with a higher density contrast would be stable against mixing on a geophysically significant time scale. *Sleep* [1988] formulated a single model of the entrainment of a dense layer and concluded that an approximately 6% density anomaly is required to prevent the layer from entrainment. *Kellogg and King* [1993] gave a similar estimate (3-6%) and noted that a low viscosity bottom layer would retard entrainment, reducing the density anomaly, required for layer stability. *Hansen and Yuen* [1989] emphasized the importance of depth dependent thermal expansion on the dynamics of the dense layer and suggested that the decrease in α with depth increases layer stability. Our results suggest a minimum required density contrast of 2% and agree with most previous studies.

The effect of internal heating on the stability of the layer was not addressed in this study. *Christensen and Hofmann* [1994] showed that varying the amount of internal heating in their models did not significantly affect the rate of entrainment of the layer. *Tackley* [1998] demonstrated that when the basal heating is completely

excluded, the rate of entrainment is considerably reduced. Such a model is unlikely true for the Earth as high temperature gradients probably exist at the base of the mantle [*Williams*, 1998]. However, this issue requires more detailed study.

Another important limitation of this study is a two-dimensional approximation. Results of *Tackley* [1998] show that the rate of entrainment is similar in equivalent 2D and 3D models. So while the dynamics in three dimensions can be qualitatively different from two-dimensional convection, our conclusions about the requirements for layer stability will probably hold for three dimensions.

If the material is efficiently entrained by the upwellings, considerable recharge of the layer is required so that the layer can exist for long periods of geological time. The sources of such recharge may include products of reactions between the core and mantle [*Knittle and Jeanloz*, 1991; *Kellogg and King*, 1993] or rock subducted from the surface [*Gurnis*, 1986; *Christensen and Hofmann*, 1994].

Modeling results of *Kellogg and King* [1993] indicate that if the layer is recharged from the core a density contrast of 3-6% is required for the material in the layer. Otherwise, entrainment processes dominate and the layer is destroyed. Such a mechanism would create a layer less than 100 km thick throughout Earth history - about half of what would be required to explain the D" discontinuity. If the material of the layer is intermixed by convection with the material above, creating a thicker layer with an intermediate density [*Kellogg and King*, 1993], the resulting layer would probably have a diffuse boundary and would be unable to produce seismic reflections.

Recharge by subduction was studied by *Gurnis* [1986] and *Christensen and Hofmann* [1994]. The problem with this scenario is that at the CMB only the original crustal layer of the subducting slab is expected to be denser than the surrounding material. This post-eclogite phase of basalt comprising the oceanic crust was estimated by *Christensen and Hofmann* [1994] to be about 2% denser than the surrounding material under the conditions relevant at the CMB. Convection models with constant viscosity demonstrated that separation of this dense phase from the rest of the slab is required in order to produce some chemical pool at the bottom of the mantle [*Gurnis*, 1986]. Incorporating the layered structure into numerical models, *Richards and*

Davies [1989] suggested that no separation between the original crust and depleted lithosphere would occur in the upper mantle and the transition zone. This result was corroborated by *Gaherty and Hager* [1994], who showed that slab dynamics in the upper part of the mantle is controlled by the thermal buoyancy and not the density differences associated with chemical lamination of the slab. However, *Christensen and Hofmann* [1994] suggested that the separation of the dense phase from the slab may occur at the bottom of the mantle and hypothesized that such separation would indeed produce a layer of post-eclogitic rock on top of the core-mantle boundary. It was found, however, that only a small fraction of the subducted crust would accumulate at the bottom of the mantle, while the rest would be remixed into the mantle. This fraction strongly depends on the Rayleigh number and is less than 2% for $Ra \sim 10^7$ [*Christensen and Hofmann*, 1994]. Using the present day rate of crust subduction of 20 km^3/yr, we can estimate that such a process would require 80-100 billion years to form a layer 200-250 km thick. Although the mantle dynamics was likely to be different in the early Earth history, we doubt that such mechanism could produce sufficient amount of material to form the D" layer. Moreover, because of intensive mixing of the subducted crust, a rather diffuse boundary is expected.

If a chemical layer with a thickness which matches the height of the D" discontinuity exists, what could the layer be comprised of? The material has to satisfy the following two properties: 1) in order to survive for a geologically significant period of time, it must be at least 2% denser than the surrounding material and 2) in order to match seismological constraints, it must have seismic velocities 2-3% higher than a lower mantle of "ambient" composition. Iron enrichment is the most effective mechanism for a density increase. However, Fe enrichment of the magnesiowüstite and silicate perovskite lower mantle results in lower velocities of the resulting assemblage. A possible exception is the low-spin Fe^{2+} [*Gaffney and Anderson*, 1973]. A spin-pairing transition in FeO was suggested by several studies (e.g., [*Strens*, 1969; *Gaffney and Anderson*, 1973; *Sherman*, 1988]). However, not only are the elastic properties of the low-spin phase unknown, the transition pressure itself is a subject of an ongoing discussion (e.g., [*Sherman and Jansen*, 1995]). In a recent study *Cohen*

et al. [1997] predicted from first-principles calculations that a magnetic collapse can occur in iron under the lower mantle conditions. However, no experimental evidence for such transitions has yet been found.

The subducted post-eclogite ocean crust, as estimated by *Christensen and Hofmann* [1994], is about 2% denser than the magnesiowüstite and silicate perovskite lower mantle and, as estimated by *Wysession* [1996], has a 2-3% faster seismic velocity. However, as was discussed above, a sufficiently thick layer of subducted ocean crust at the base of the mantle is unlikely.

Vidale and Benz [1993] estimated that a 25% enrichment in stishovite of the basal layer could explain the seismic data. Using a third-order Birch-Murnaghan equation of state we calculated the properties of SiO_2 stishovite at pressures 250 km above the core mantle boundary. The estimated density of stishovite at that depth is about 3% lower than the density of a magnesiowüstite and silicate perovskite assemblage with $\chi_{Pv} = 0.55$ and $\chi_{Fe} = 0.11$, which is the composition that provides a good fit to PREM, as estimated in our study. Several post-rutile structures have been proposed for SiO_2 and two were experimentally identified. These are a $CaCl_2$-type structure [*Tsuchida and Yagi*, 1989] and a α-PbO_2-type structure [*Dubrovinsky et al.*, 1997; *Karki et al.*, 1997a, b]. However, the volume change associated with each of the associated transitions is less than 1% [*Tsuchida and Yagi*, 1989; *Karki et al.*, 1997a]. This means that even if all silica at the base of the mantle is transformed into $CaCl_2$ structure, as suggested by *Kingma et al.* [1995], or even into α-PbO_2 structure, it will remain less dense than the magnesiowüstite and silicate perovskite assemblage. It is obvious that silica enrichment alone cannot provide a dynamically stable layer and some iron enrichment is also required.

Any extra iron in D" is likely to enter FeO, though some amount of FeSi alloy may also be present [*Knittle and Jeanloz*, 1991]. So iron enrichment is equivalent to the increase in FeO content. This means that if any high pressure phases of FeO exist, their properties may significantly affect the amount of FeO required to dynamically stabilize the layer. Two phase transitions in FeO at high pressures have been reported. One, taking place around 16 GPa, has been associated with a distortion of

the rock-salt-type cell into a rhombohedral cell [*Zou et al.*, 1980; *Yagi et al.*, 1985]. Another transition observed at pressures about 70 GPa [*Jeanloz and Ahrens*, 1980; *Knittle and Jeanloz*, 1986; *Yagi et al.*, 1988] is interpreted as a transition to a NiAs phase [*Fei and Mao*, 1994]. The nature of the other transition, that has only been observed in shock compression at about 70 GPa [*Jeanloz and Ahrens*, 1980; *Knittle and Jeanloz*, 1986; *Yagi et al.*, 1988], still remains a matter of discussion. A structure of the B2 (CsCl) or B8 (NiAs) type was suggested for the high pressure phase [*Jeanloz and Ahrens*, 1980; *Jackson and Ringwood*, 1981; *Navrotsky and Davies*, 1981]. Electronic type of the transition is also possible [*Jeanloz and Ahrens*, 1980], but unlikely [*Jeanloz and Ahrens*, 1980; *Sherman and Jansen*, 1995]. The phase transition at 70 GPa is accompanied by a density increase of at least 10-16% [*Jackson and Ringwood*, 1981]. However, the elastic moduli are similar for the low pressure and high pressure polymorphs, so that velocity is expected to decrease in the transition [*Jeanloz and Ahrens*, 1980]. A solid solution of MgO and FeO may have a significantly different phase diagram. Shock compression of $Mg_{0.6}Fe_{0.4}O$ to 200 GPa [*Vassiliou and Ahrens*, 1982] did not find a convincing evidence for any phase change similar to the phase transition of FeO at 70 GPa. This questions the existence of high pressure modifications of magnesiowüstite in the lower mantle and suggests that the density and elastic moduli of any such phases must be similar to the low-pressure phase.

We calculate the influence of stishovite and iron enrichment on the density and shear velocity of the adiabatic 1D model (Figure 3.5). The filled circle represents the composition of the computed adiabatic 1D model (a silicate perovskite and magnesiowüstite assemblage with $\chi_{Pv} = 0.55$ and $\chi_{Fe} = 0.11$). The solid contours indicate the influence of the change in iron content or stishovite enrichment on the density of the assemblage, while the dashed contours indicate the effect on the shear velocity. The light shaded area shows the range of compositions consistent with the requirements for a dynamic stability of the chemical layer ($\triangle \rho_0 / \rho_0 \geq 2\%$). The medium shaded region represents the range of compositions consistent with a seismologically observed shear velocity increase by 1-3%. The intersection of the two regions, the dark shaded region, represents the range of compositions that are both

dynamically and seismologically consistent. According to this analysis, 25-60% by volume of stishovite, accompanied by a significant increase of χ_{Fe} could produce a layer that would provide the required velocity jump and be dynamically stable. Due to the very small volume change and predicted average shear modulus softening of 10-30% estimated by *Jeanloz* [1989] for rutile→CaCl$_2$ transition, transformation of silica into one of the mentioned above post-rutile phases probably would not affect the estimates significantly or considerably reduce the required amount of silica.

The source of the extra SiO$_2$ and FeO is not clear. Several possibilities may exist. It was first suggested by *Birch* [1952] that silicates would break down into simple oxides under high pressures. A later study by *Stixrude and Bukowinski* [1990] supported the dissociation of silicate perovskite to SiO$_2$ and (Mg,Fe)O under the D" conditions. Such dissociation would produce a seismic velocity increase by about 3%, as estimated by *Wysession* [1996]. *Stixrude and Cohen* [1993] argue against such decomposition under lower mantle conditions, but more recent experimental work of *Meade et al.* [1995] shows evidence for a dissociation of silicate perovskite into an assemblage of perovskite and mixed oxides. However, estimates show that even if SiO$_2$ is transformed into one of the known post-rutile structures, perovskite remains denser than the isochemical mixture of oxides [*Tsuchida and Yagi*, 1989]. This means that silicate perovskite is expected to be stable under the lower mantle conditions, unless some denser phases of silica and magnesiowüstite exist.

Chemical reactions between the core and the mantle material may be another source of SiO$_2$ and FeO in D" [*Knittle and Jeanloz*, 1991], but, as was discussed above, this mechanism is unlikely to be sufficiently efficient to create enough reaction products to generate a layer of required thickness.

The layer may also have been created in the process of Earth differentiation. A model of inhomogeneous accretion predicts a layer of refractory material at the top of the CMB, since this material is expected to be about 2% denser than normal mantle [*Ruff and Anderson*, 1980]. However, as estimated by *Ruff and Anderson* [1980], the refractories would have about 5% lower seismic velocity, so such composition is an unlikely candidate for a D" chemical layer consistent with the seismic discontinuity
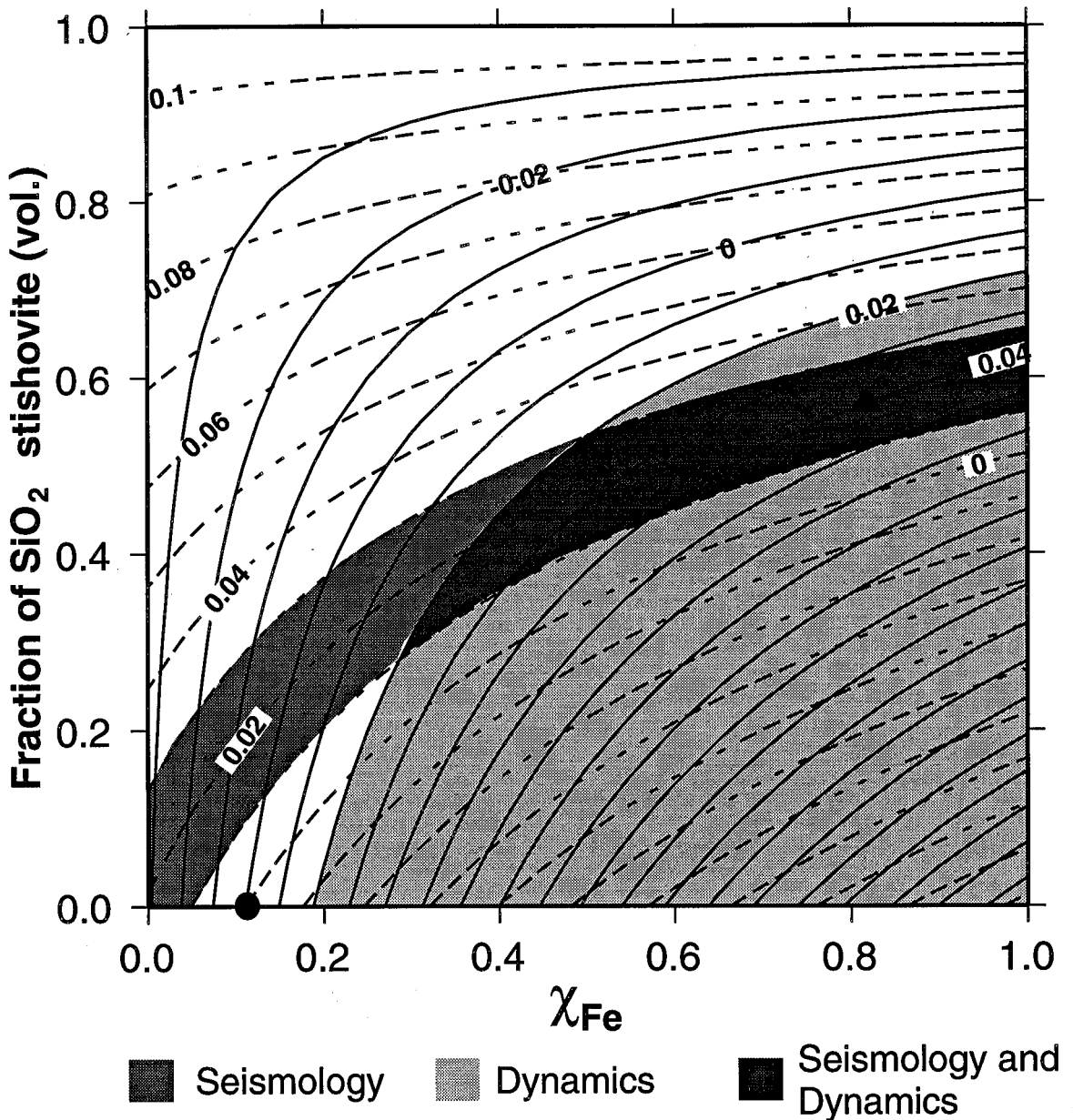
Figure 3.5: Calculated relative change in density (solid contours) and shear velocity (dashed contours) of the adiabatic 1D model, resulting from a stishovite enrichment and change in Fe content. The light shaded area indicate the range of dynamically consistent compositions; the medium shade indicates seismologically consistent composition; the range of compositions that are consistent with both seismology and dynamics is marked by the dark shade. The filled circle indicates the composition of the adiabatic 1D model. The filled triangle marks the composition used to calculate seismic velocities for dynamic models with $\triangle \rho_0 / \rho_0 = 0.04$.

at its top.

The stishovite and iron enriched composition used for computing the shear velocity cross-sections (Figure 3.2) is marked in Figure 3.5 with a filled triangle. It corresponds to $\chi_{Fe} = 0.82$ and 58% (vol.) of stishovite. This composition provides a 2% velocity jump at the top of the chemical layer, and its density contrast (4%) is consistent with the value of $\triangle\rho_0/\rho_0$ used in the dynamic modeling. However, the only case that predicts the height of the discontinuity consistent with seismological observations in the seismically fast (cold) regions is model M10, where the layer was originally 400 km thick. All other cases predict a discontinuity too close (less than 100 km) to the CMB or the discontinuity is missing. This implies that, unless even higher density contrast is assumed for the basal material, the chemical layer must be about 400 km thick on average to be consistent with seismological observations.

What possible reasons may complicate seismological detection of the top of such a dense chemical layer in seismically slow regions? Source-receiver pair geography may play some role [*Kendall and Shearer*, 1994]. It is also very possible that the seismically slow regions in D" where no evidence for the discontinuity exists are chemically different from the rest of the basal material. One possibility is iron-rich phases coming from the core. This material, when mixed with the dense and seismically fast basal layer, would reduce its velocity and this reduction may be sufficient to neutralize the jump at the top of the basal layer. Hot upwellings may facilitate this process. Another possible mechanism that may potentially complicate detection is defocusing of seismic waves by a convex top boundary of the layer, expected in the upwelling regions. However, our models show a very smooth material interface with very low curvature. Such an effect is unlikely to play any significant role.

A viable alternative to a chemical layer is a phase transition. This interpretation of the seismic discontinuity is favored by *Nataf and Houard* [1993] and was considered by *Wysession* [1996]. No relevant phase change has been experimentally confirmed. But the hypothetical possibilities include the breakdown of silicate perovskite into the constituent oxides [*Wysession*, 1996] or some, not yet known, transition in perovskite or magnesiowüstite. As was demonstrated by *Sidorin et al.* [1998], a rather small

change in the effective shear velocity of the mineral assemblage will suffice to explain the seismic observations. Thus a phase transition in some of the minor constituents of the lower mantle can be responsible for the observed seismic triplication.

3.6 Conclusions

Our current state of knowledge on D" does not allow us to accept or rule out a chemical origin of the seismic discontinuity at the top of the D" region. Tighter constraints are required on the high pressure properties of minerals relevant to the lower mantle, the phase diagrams and the change of volume and elastic moduli associated with various transitions. We still poorly understand the extent of material exchange between the core and the mantle and the scope and rate of chemical reactions at the CMB, as well as the evolution of the Earth as a whole. However, dynamic modeling, seismic observations and general considerations argue against a simple chemical layer. Some of the arguments are the following:

1. Dynamic models suggest that at least a 2% density contrast is required in order for a chemical layer to survive for geologically significant periods of time. This, combined with a seismic observations of a 2-3% velocity increase, requires a very large impedance change. A complex change in composition is probably required, since enrichment or depletion in a single mineral is unlikely to be able to produce the required impedance contrast.

2. An even higher density contrast (4% or more) and initial thickness of about 400 km are required to ensure the layer exists under the downwellings. A mechanism able to form a layer of such thickness throughout the history of the Earth is not known. Estimates show that neither subducted material, nor the products of reactions with the core can supply enough material. Refractories emplaced from the core, although they may have the required density contrast, are expected to have lower velocities than normal mantle and thus are unlikely candidates.

3. Dynamics of a dense layer implies that the material interface in the downwelling

regions is accompanied by a high vertical temperature gradient. This means that the discontinuous velocity increase will occur in a region with negative vertical gradient of seismic velocity. Such a model would require a higher velocity jump ($> 3\%$) than the *Lay and Helmberger* [1983] model in order to produce sufficiently strong reflections, consistent with seismic observations. This requires an even higher impedance contrast.

4. It is difficult to explain why a seismic discontinuity has not been confirmed on top of D" in any seismically slow (hot) region of the world. A chemical layer of significant thickness in the downwelling regions, completely thinned out in the upwelling regions, is not dynamically plausible. Dynamic models predict a very smooth material interface in the upwelling regions, so any defocusing effects cannot be important.

5. A simple chemical layer cannot explain other seismological observations relevant to D", such as the high heterogeneity or anisotropy.

If D" is a chemical layer, it is most likely chemically heterogeneous and its dynamics is much more complex than shown by our models or any other models to date. Its morphology is probably influenced by other processes so far ignored and, perhaps, still unknown processes that are yet to be discovered.

Chapter 4 Dynamic Study of Seimologically Observed Geographical Patterns of the D" Triplication

4.1 Abstract

We have formulated dynamic models of processes hypothesized to give rise to observed seismological structure at the base of the mantle. One-dimensional seismic models are determined from thermo-chemical convection calculations from which synthetic waveforms are computed. Of the three scenarios studied, (1) a thermal slab, (2) a thermal slab interacting with simple chemical layer, and (3) a thermal slab interacting with a phase transition, the strength of seismic phases computed from (3) best correlates with the global geography of the observed D" triplication. Seismic structures predicted by (1) or (2) are inconsistent with the global geography and strength of the triplication. Our successful model motivates a new class of 1-D seismic models with two mild gradients and a small discontinuity. To test this hypothesis, we searched for seismic models that both contain these features and fit D" seismic observations. Our preferred model contains a gentle positive gradient initiated 350 km above the CMB and a 1% jump in S-velocity near 200 km. A strong negative gradient begins about 100 km above the CMB, similar to previous studies representing the lower thermal boundary layer. With the reduced first-order discontinuity, the P-wave triplication becomes too small to observe and provides a simple explanation for the observed weakness of the P in proportion to the S triplication.

4.2 Introduction

The lowermost mantle, D", contains substantial variations in seismic velocity both radially and laterally on ~ 10 km to $> 10^3$ km scales. One of the most significant observations is a triplication caused by an apparent velocity jump a few hundred kilometers above the core mantle boundary (CMB) [*Lay and Helmberger*, 1983]. This triplication is indicated by a phase, Scd and Pcd, occurring in the distance range of 70° to 90° between direct body wave arrivals and core reflections. Although the triplication is most pronounced in S waves, it has been detected in a number of locations with P waves [*Weber*, 1993]. The seismic triplication has most often been modeled as a sharp 2-3% jump in velocity 200-300 km above the CMB. Although the Scd and Pcd phases have been detected in a number of regions around the world, the triplication is best displayed beneath downwelling circum-Pacific subduction zones [*Lay et al.*, 1998]. There is some indication that Scd occurs beneath the mid-Pacific [*Garnero et al.*, 1993; *Russel and Lay*, 1998], an area which has been devoid of subduction since at least the Mesozoic.

A number of models for the origin and state of the D" discontinuity have been advanced. It has been suggested that D" is a chemically distinct layer at the base of the mantle with a sharp velocity increase at the material interface. Other interpretations include the contrast between the ambient mantle and subducted slabs or a solid-solid phase transition (see [*Wysession et al.*, 1998] for review). Although the details have yet to be established, each model should yield predictions as to how the local seismic velocity characteristics (for example, detailed structure determined from modeling Scd phases) are related to larger-scale seismic geography (tomography) of the lower mantle. One interpretation of the sharp discontinuity atop D" is that it represents a jump in major element chemistry and density [*Lay and Helmberger*, 1983; *Davies and Gurnis*, 1986; *Christensen*, 1996b]. This model has been favored because it is thought that thermal structures would be too diffuse to cause a triplication. The dynamics of a chemically distinct layer at the base of the mantle has been considered in the past using different mechanisms by which such a layer is formed, such as a chemical

reaction or infiltration from the core [*Hansen and Yuen*, 1988; *Kellogg and King*, 1993; *Kellogg*, 1997], an ancient pre-existing layer [*Davies and Gurnis*, 1986; *Hansen and Yuen*, 1988; *Sidorin and Gurnis*, 1998; *Tackley*, 1998], or a continuous segregation of oceanic crust from subducted slabs [*Gurnis*, 1986; *Christensen and Hofmann*, 1994]. The dynamic results are always the same – within less than ∼ 100 Myr, the dense material is swept away from downwellings into upwellings if the density contrast is moderate. For large density contrasts (≥ 6%) the layer survives under the downwellings but is thinned out, while its thickness in the upwelling regions increases.

Tomography now provides information on the global dynamic context of a particular region of the mantle. This information can give insight into the origin of D", generally, and the validity of the chemical layer hypothesis, specifically. Long period inversions of large scale structure in the lowermost mantle show that the circum-Pacific belt is relatively fast while beneath the central Pacific and Africa the velocities are slow [*Masters et al.*, 1996; *Li and Romanowicz*, 1996; *Su et al.*, 1994]. This long wavelength structure is consistent with seismically fast regions being cold and generated by subduction [*Engebretson et al.*, 1992; *Ricard et al.*, 1993; *Richards and Engebretson*, 1992]. Higher resolution bodywave tomography shows that these fast lower mantle anomalies are relatively narrow linear features extending radially below seismogenic Benioff zones to the CMB below the circum-Pacific [*van der Hilst et al.*, 1997; *Grand et al.*, 1997]. These linear high shear velocity structures are structurally similar to downwellings obtained in convection models (e.g., [*Bunge et al.*, 1996; *Tackley et al.*, 1993]) and to slabs displayed in simple convection models with plates and whole-mantle convection [*Bunge et al.*, 1998; *Davies*, 1997; *King and Hager*, 1994; *Sidorin and Gurnis*, 1998; *Zhong and Gurnis*, 1995, 1997]. When slabs reach the CMB in such convection models, they spread out forming broad low temperature anomalies (a few thousand km's across and a few hundred km's high) atop the CMB.

The seismically fast structure over the CMB, shown beneath the Caribbean, for example, by *Grand et al.* [1997] occurs in a region where Scd is an easily detected arrival [*Lay and Helmberger*, 1983; *Kendall and Nangini*, 1996; *Ding and Helmberger*, 1997]. Considering the dynamic models described above and the tomography showing

penetration of some slabs completely through the lower mantle [*Grand et al.*, 1997; *van der Hilst et al.*, 1997], we would expect that a chemical layer would be pushed away from beneath circum Pacific subduction zones. However, it is beneath circum-Pacific subduction zones where the triplication is best displayed [*Lay et al.*, 1998]. The precise nature of seismic waveforms predicted by the chemical layer model (or indeed any dynamic model) has never been determined so that we cannot immediately rule out this possibility.

It is not clear how old slabs will influence the occurrence of the Scd phase or how the phase will behave in the presence of a chemical layer below subducted slabs. It is not known which class of dynamic models (if any) will give rise to a strong Scd arrival beneath downwellings while having a weak Scd arrival below upwellings. Consequently, since one-dimensional seismic models inferred from waveform studies are not unique, we introduce a new approach at interpreting D" by starting with dynamic models. We transform the temperature, composition, and solid phase resulting from dynamic models into seismic velocities and use such seismic structures to compute synthetic waveforms. A comparison between dynamic models and seismic tomography suggests that a new class of 1-D models (consisting of two gradual changes and a small jump in velocity) are more appropriate than those used in past purely seismological studies. These velocity models are then used to compute synthetics which are then tested against observed seismic record sections for the Caribbean.

4.3 Synthetic Record Sections from Convection Models

We formulate models of thermal-chemical convection with imposed plate kinematics in a two-dimensional cylindrical geometry with temperature dependent viscosity using the finite element method following the procedure described in Chapter 3. The calculations are for transient flow in which slabs descend through an incompressible and initially isothermal fluid with a hot thermal boundary layer (100 Myr old) at the

Table 4.1: Parameters used in dynamic models

Parameter	Value
Radius of the Earth	6371 km
Rayleigh number	1.4×10^7
Temperature variation across the mantle	2900 K
Temperature dependence of viscosity[a]	
μ_0	3×10^{21} Pa·s
c_1	41.50
c_2	1.03

[a]Arrhenius law temperature dependence is used for viscosity: $\mu(\theta) = \mu_0 \exp\{c1/(\theta + c_2) - c1/(1/2 + c_2)\}$, where θ is dimensionless temperature. At low temperatures a cutoff of 3×10^{22} Pa·s is used.

base. Since well defined oceanic plates and trench roll back are essential attributes of the convection models, subduction becomes well developed. The parameters governing these calculations are shown in Table 4.1. The temperature-dependence of viscosity gives three orders of magnitude variation across the hot thermal boundary layer and one order of magnitude across the slab; the effective viscosity of slabs is expected to be reduced considerably because of the stress dependence of silicate rheology [*Christensen*, 1984; *Moresi and Gurnis*, 1996] which has not been incorporated into the present models. This model differs from that used in Chapter 3 in terms of the temperature-dependence of viscosity and the inclusion of an exothermic phase transition just above the CMB.

An adiabatic model of elastic and thermodynamic parameters of the lower mantle (Chapter 2) is taken as a starting model for the radial 1-D shear velocity. The computed temperature, chemistry and phase are used to add the non-adiabatic perturbations to the adiabatic velocities and produce a 2-D velocity field using a technique described in detail in Chapter 2. PREM values [*Dziewonski and Anderson*, 1981] are assumed for the seismic velocity in the upper mantle. The phase transition is modeled using techniques widely used in geodynamics [*Christensen*, 1995]; it is characterized by an ambient height above the CMB (pressure), ambient temperature, Clapeyron

slope, and density difference. We have explored a number of cases (Table 4.2) of a purely thermal slab interacting with (a) a thermal boundary layer, (b) dense basal layers, and (c) an exothermic phase transition just above the CMB.

We start with a purely thermal slab interacting with a basal thermal boundary layer with no change in chemistry or phase. In this nominal model (Case 1), the oceanic plate moves with a velocity of 5 cm/yr and the subducting lithosphere has an age of 130 Ma. After 315 Myr of subduction, a seismic velocity structure has formed (Figure 4.1a) which is similar to that suggested from seismic studies within and below subduction zones [*van der Hilst et al.*, 1997; *Grand et al.*, 1997]. Slabs and the thermal anomalies generated atop the CMB are time-dependent, on a time scale > 10–50 Myr, as the slab folds and buckles in a manner akin to the way slabs have been hypothesized to buckle in the transition zone [*Gurnis and Hager*, 1988; *Christensen*, 1996a; *Davies*, 1997].

Radial sections of the computed seismic velocity field are made through two portions of the slab and an area distant from it (Figure 4.1a), and 1-D synthetics are computed for each of the profiles using the Cagniard de Hoop generalized ray theory (GRT). In all locations the seismic velocity has a negative gradient in the lowermost ~100 km of the mantle caused by the hot-thermal boundary layer. Over a radial span of 300 km seismic velocity deviates from the adiabatic profile by ≈1–2%. Only a model associated with cross-section C produces an extra phase (indicated as St, Figure 4.1a) arriving between S and ScS and observed at distances from about 80° to 85°. We interpret this phase as the energy turning about 300 kilometers above CMB where the thermal structure of the slab creates a significantly high seismic velocity gradient. We find that the folding of the slab plays an important role in generating this phase, as the local effective low-velocity zone at the axis of a fold (as in cross-section C on Figure 4.1a) tends to amplify the arrivals from the high-gradient zone below it. However, this phase is weak, has a relatively long period, and arrives very close to S, so that it will most likely be lost in the direct S and thus cannot be the phase generally referred to Scd. Moreover, this weak phase only occurs in a small distance range and completely disappears if Section C in Figure 4.1a moves ≈100 km

Table 4.2: Summary of Scd predictions from various dynamic models

Case	Type[a]	Plate velocity, cm/yr	Age at subduction, Myr	Initial layer thickness or ambient phase transition elevation, km	Density change	S velocity change	Scd presence[b]	
							downwellings	upwellings
1	T	5	130	—	—	—	rarely	never
2	T	2.5	260	—	—	—	rarely	never
3	T	10	65	—	—	—	rarely	never
4	T	5	260	—	—	—	rarely	never
5a	C	5	130	250	4%	1%	rarely	rarely
5b	C	5	130	250	4%	2.75%	rarely	always
6a	C	5	130	250	6%	1%	rarely	rarely
6b	C	5	130	250	6%	2.75%	rarely	always
7a	P	5	130	250	1%	1%	usually	rarely
7b	P	5	130	250	1%	2.75%	always	usually

[a]T – purely thermal model; C – model with a basal dense chemical layer; P – model with a phase change with Clapeyron slope $\gamma = 6$ MPa/K.

[b]The spatial persistence and relative amplitude of Scd phase are characterized using the following qualitative scale: never, rarely, usually and always.
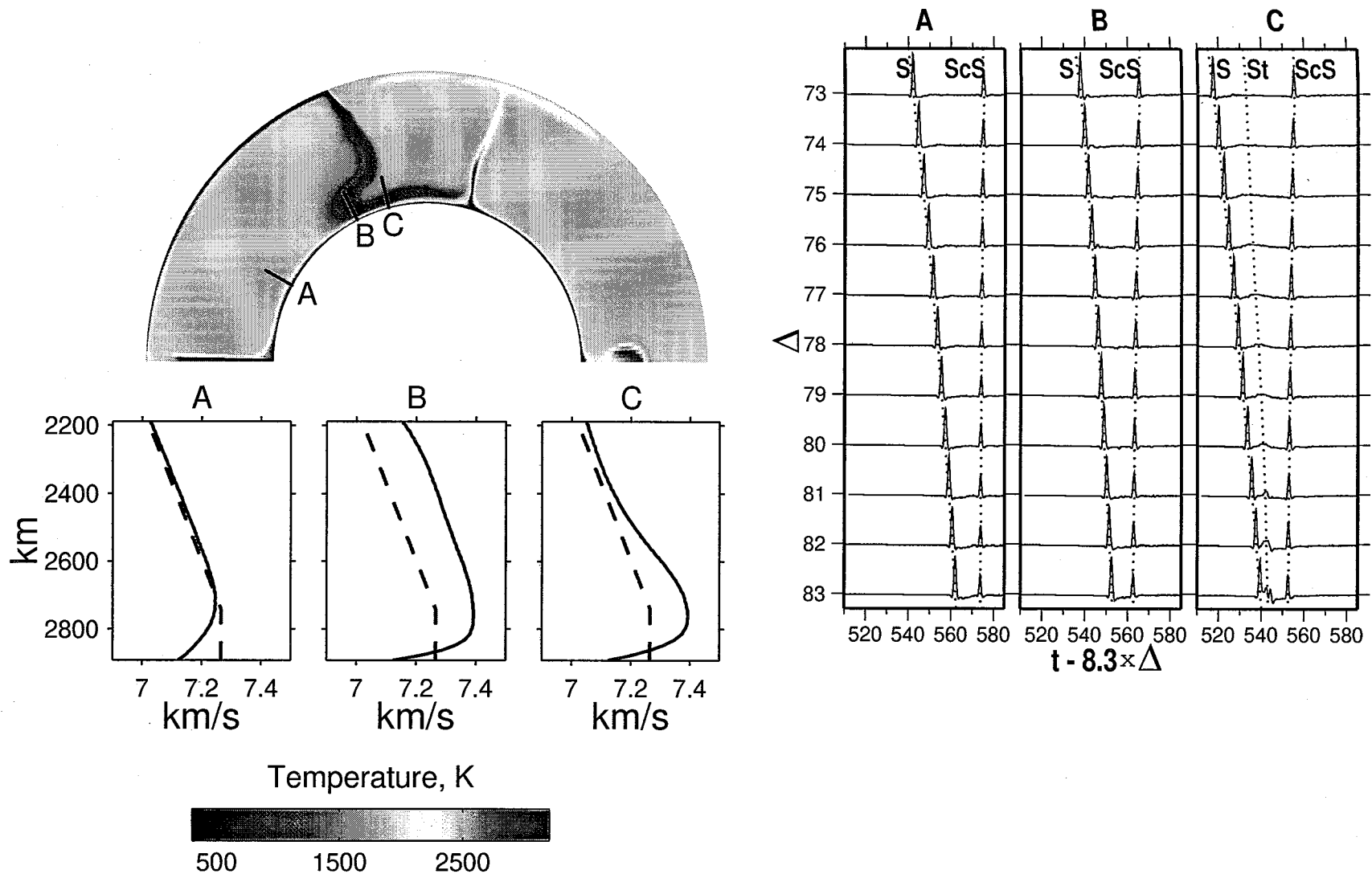
Figure 4.1: Temperature structure after 315 Myr of subduction and computed seismic velocities for the indicated radial profiles (left) with the corresponding waveforms (right). For each velocity profile the red line shows the computed shear wave velocity and the dashed blue line gives PREM [*Dziewonski and Anderson*, 1981] values for reference.

a) Case 1 — purely thermal model.
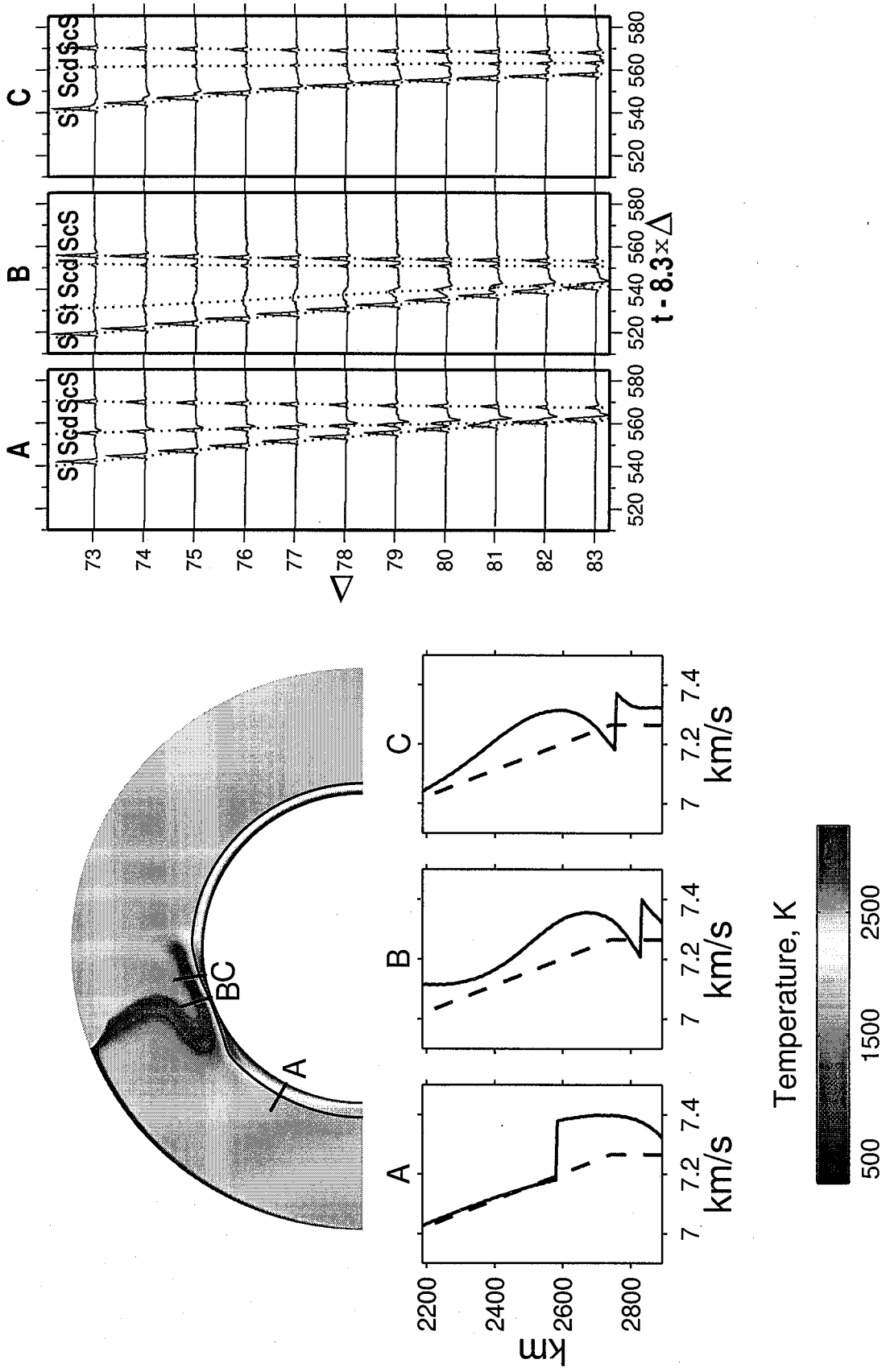
Figure 4.1 (*continued*): **b)** Case 6 — basal chemical layer. The top of the chemical layer is outlined by the solid black line; the layer was initially 250 km thick and has a density contrast of 6% and shear velocity contrast of 2.75%.
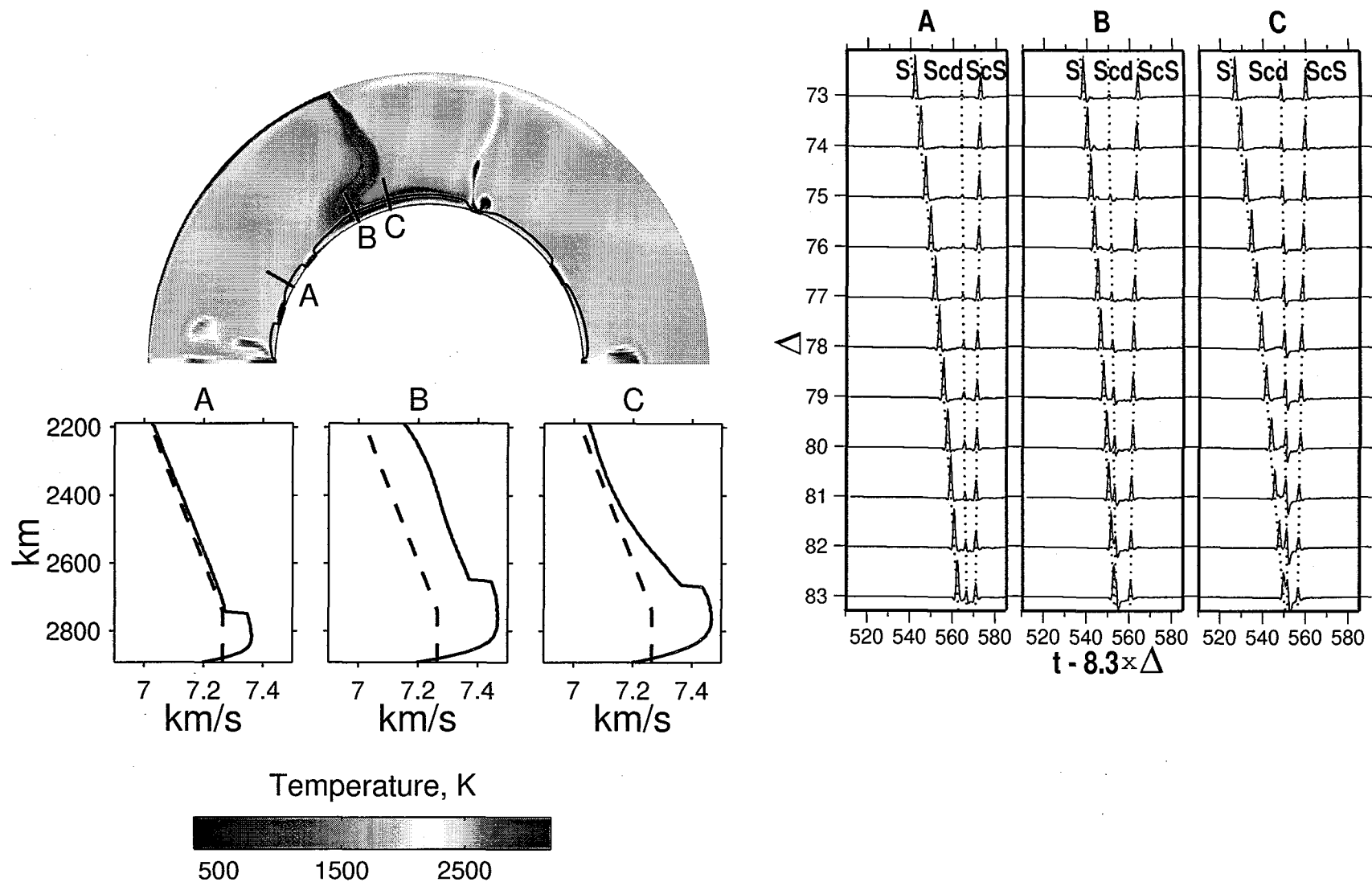
Figure 4.1 (*continued*): **c)** Case 7 — basal solid-solid phase transition. The phase boundary is outlined by the solid black line; the ambient-temperature elevation of the transition above CMB is 150 km, the Clapeyron slope is 6 MPa/K and the associated density and shear velocity changes are 1%.

in either direction. We have varied the age of the lithosphere at subduction between 65 and 260 Myr and the plate velocity between 2.5 and 10 cm/yr (Cases 2-4) but have been unable to produce a phase significantly stronger than phase St shown on Figure 4.1a, cross-section C.

We now turn to the interaction of a slab with pre-existing chemical layers at the base of the mantle while using the same characteristics for the subducting oceanic plate as our nominal model (5 cm/yr velocity and 130 Ma age). We assume the layer to be 250 km thick initially. When a 4% density contrast is used for the basal material (Case 5), we find that after $\approx$ 300 Myr of subduction the slab has pushed the chemical layer aside, so that the radial cross-sections through the slab are very similar to the cross-sections observed for the purely thermal cases discussed above and the corresponding synthetic waveforms do not show any evidence for the Scd phase.

If the density contrast of the basal material is increased to 6% (Case 6), the layer still exists under the slab after 315 Myr, although it is significantly thinned (Figure 4.1b). We calculated a series of radial seismic velocity cross-sections and corresponding synthetic waveforms. Three of them, two for different locations in the downwelling region and one for a region with no subducted material are presented in Figure 4.1b. A 2.75% shear velocity increase is assumed for the basal layer, in line with most 1-D seismic models that successfully predict the D" triplication. The shear velocity profile in a region without subduction (cross-section A in Figure 4.1b) with a 2.75% velocity jump in S velocity 300 km above the CMB has a mild negative gradient down to the CMB and mimics most 1-D velocity models of the D" discontinuity. As expected, this velocity model produces a very strong Scd arrival on the synthetic seismogram. In the downwelling regions, however, the seismic velocity structures can be quite complex. The cold slab resting atop the chemical layer produces a strong vertical temperature gradient across the material interface. As such, the temperature gradient corresponds to a negative seismic velocity gradient. Just above the seismic velocity jump at the material interface there is a substantial local low-velocity zone which shadows the triplication from the interface (cross-sections B

and C in Figure 4.1b). The Scd arrivals for both cross-sections corresponding to the downwelling region are very weak and have amplitudes comparable to phase St, which is also observed for one of the cross-sections (B). We have been unable to reproduce the observed geographical pattern of Scd, i.e., strong below downwellings and weak or absent below upwellings, for any combination of anomalous density or shear velocity contrast associated with the basal layer (Table 4.2).

An alternative model for the D'' triplications is a solid-solid phase transition which has hitherto not been studied dynamically. We explore how an exothermic phase transition located a few hundred kilometers above the CMB influences the seismic velocity structure at the base of the mantle and the appearance of the Scd phase. An exothermic phase transition is explored because it will be elevated below cold downwellings, and we suspect easier to detect seismically, while below upwellings it will be depressed and more difficult to detect. Since there are as of yet no experimental constraints on phase transitions at CMB pressures, our results should be considered illustrative rather than definitive. The characteristics of the phase transformation obviously determine the resulting seismic structure and the corresponding waveforms. However, no systematic analysis of the parameter space has been undertaken in this study and a single model, that we believe performs reasonably well, is presented as an illustration. We assume an exothermic phase transition with a Clapeyron slope of 6 MPa/K, an ambient height of 150 km, and a density change of 1% (Case 6). Again, the subducting plate is moving at 5 cm/yr and the age of the lithosphere is 130 Ma. The phase transition is elevated over broad horizontal scales where slabs have folded atop the CMB (Figure 4.1c). Since the transition occurs within a thermal boundary layer characterized by substantial lateral variations in temperature driven by cold slabs and starting plumes, there are strong spatial and temporal fluctuations in transition depth causing the seismic triplications to intermittently appear and disappear. Although the location of the phase transition may have insignificant spatial variations in the downwelling regions, the triplication is intermittent because of spatial variations in the radial thermal gradient (Figure 4.1c, B and C). Where the 1% jump in shear velocity is superimposed on a PREM-like velocity gradient (Figure 4.1c, A and

B), a very weak Scd arrival is observed. In contrast, when the local radial gradient is relatively high, just a 1% discontinuity appears to be sufficient for producing a strong Scd phase (Figure 4.1c, C). This model provides a successful match to the geographic distribution of Scd inferred from seismic data, i.e., strong beneath downwellings and weak below upwellings.

4.4   Discussion and Conclusions

We have formulated geodynamic models of three competing physical models of the processes which could give rise to the prominent Scd phase. The results of the synthetic waveform modeling for all the dynamic cases considered are summarized in Table 4.2. Although a detailed interpretation is premature, of the three scenarios studied, a thermal slab, a simple chemical layer, and a phase transition, synthetics computed from the phase transition (with associated changes in density and shear velocity of 1%, Case 7a) best correlate with the global geography of D" triplication observations. Synthetics from thermal slabs or thermal slabs interacting with a chemical layer are inconsistent with the global geography and strength of the triplication. Our successful model motivates a new class of 1-D seismic model with two mild gradients and a small discontinuity. One of such models, SGHD120, is shown in Figure 1.1. This model is as successful at matching the S wave triplication data as traditional models. Using similar parameterization for a P velocity model [*Sidorin et al.*, 1998] has the added advantage of providing a simple explanation for the weakness of the comparable Pcd phase [*Ding and Helmberger*, 1997].

One interesting aspect of the dynamic models is that the time-dependence evident in slabs folding atop the CMB will give rise to a strong intermittance in the appearance of the triplications and may help explain why in mantle downwelling regions the Scd can disappear locally, as they apparently have below isolated parts of the Caribbean [*Kendall and Nangini*, 1996].

A phase transition origin of D" has been conjectured previously and here we find that seismic models computed from the dynamic systems with an exothermic

phase transition under a certain range of conditions provide an excellent match to the observed waveforms. However, this model is not unique and a second and potentially more attractive origin of the hypothesized 1% sharp jump in seismic velocity model SGHD120 (Figure 1.1) is former oceanic crust embedded within the interior of the broader thermal halo of slabs. Our dynamic models of subduction have slabs being laid out horizontally directly atop the CMB so the potentially higher seismic velocity of the former basaltic component will be laid out over $\sim 10^3$ km and could, for example, come to an abrupt end as the slab folds onto itself (Figures 4.1a–4.1c). Of course, this horizontal lithologic boundary will occur within the halo of the slab. This class of models is computational difficult and a detailed analysis awaits further study.

The SH seismic model SGHD120 motivated by this study contains more parameters than previous attempts at modeling the D" triplication. Note that the earliest models explained the Scd phase with only two parameters, a velocity jump and thickness and they proved very effective for this same particular path [*Zhang and Lay*, 1984]. Thus, the model is not unique but simply explains the existence of a strong Scd with a much subdued Pcd by adding an extra set of parameters.

The new seismic model proposed here has most of the S-velocity increase in D" attributed to a gradient which appears to be indicative of cold slabs which have accumulated atop the CMB. The remaining 1% jump needs an explanation which we have assumed to be a phase-change and compatible with the colder environment. Moreover, if the seismically fast regions atop the CMB are indeed old accumulated slabs, substantial lateral variation in Scd strength will depend on the rate of subduction, age of the lithosphere subducted, and lapse time since arriving at the CMB.

Chapter 5 Dynamics of a Phase Change at the Base of the Mantle Consistent With Seismological Observations

5.1 Abstract

The phase change model for the origin of the D" seismic discontinuity is tested by comparing the results of convection modeling with seismic observations. We compute a number of global dynamic models that incorporate a phase change at the base of the mantle with different characteristics and transform the resulting temperature field and the distribution of phases to seismic velocities. Over 900 2-D synthetic waveforms are computed for each of the models from which S, ScS and Scd phases are picked. The distribution of the relative amplitudes and differential travel time residuals for these phases is statistically compared with the distribution of data from four well studied regions (northern Siberia, Alaska, India and Central America) in a search for the characteristics of a phase transition that best match these seismic observations. We find that the best fit among the models considered is obtained for phase transitions characterized by a Clapeyron slope of about 6 MPa/K and an elevation above the core-mantle boundary of about 150 km under adiabatic temperature, or 127 GPa and 2650 K on a (P,T) diagram. Dynamic models demonstrate that the value of Clapeyron slope and the density difference between the phases can have significant influence on the dynamics of plumes but probably only a minor influence on the dynamics of subducted slabs. We find that the thermal structure of subducted slabs can be important in giving rise to the seismic triplication – the strongest Scd arrivals in our models are observed in the area of subduction. The folding of the slab at the base of the mantle leads to patterns in differential travel time distributions consistent

with seismic observations and suggests that the largest heterogeneity occurs at the top of the D" layer or just above it. Analysis of the spatial autocorrelation functions of the differential travel time residuals suggests that their characteristic peaks reflect the patterns of slab folding and may provide constraints on the rheology of slabs at the base of the mantle.

5.2   Introduction

A recent study by *Lay et al.* [1997] addressed variations in the structure of the D" discontinuity considering the correlations and spatial patterns in Scd-S, ScS-Scd, and ScS-S differential travel time residuals for raypaths sampling the lowermost mantle in three different regions of the world. The study suggested a strong lateral heterogeneity at scale lengths of 600-1500 km at the base of the mantle with significant heterogeneity at smaller (200-500 km laterally) scales. The strongest heterogeneity was prescribed to the region just above or within the top thin layer of D". Although these observations alone may have important dynamic implications, the analysis was unable to distinguish between the volumetric velocity anomalies and the topography of the D" discontinuity. Even when the velocity structure is well constrained, it does not allow a unique determination of the variation of material properties, such as elastic moduli, density or viscosity, all of which to some extent control the dynamics of mantle flow. The data that is used to study the D" seismic structure, for example, are either not sensitive to the density variations (as SH reflections off the discontinuity) or are heavily contaminated by either noise or superposition of other phases (as SV or P reflections). Consequently, seismological modeling fails to distinguish between thermal and compositional influences on the velocity field.

To provide further constraints on the system, a multi-disciplinary approach is required, where dynamically consistent seismic velocity predictions are compared with the seismological observations. Dynamic models that are able to reproduce the seismologically observed general trends and behavior of the seismic travel times and amplitudes, while still not unique, can significantly narrow the range of possibilities

for the dynamic mechanisms responsible for certain seismic features, such as, the D" discontinuity. Moreover, the dynamic models can also suggest which new or additional seismological observations can be made to distinguish between competing models.

Following such an approach, in Chapter 2 we presented a technique to predict seismic velocities consistent with dynamics, experimental mineral physics and geochemical constraints. In Chapter 4 we used this technique to produce radial seismic velocity profiles for three classes of dynamic models simulating different mechanisms for the origin of the D" discontinuity. The velocity profiles were used to produce SH synthetics which were analyzed for the presence of the Scd phase. We demonstrated that thermal gradients from subducted slabs alone atop the CMB cannot produce a sufficiently strong Scd arrival. A chemical layer model with a sufficient velocity contrast can cause a strong triplication, but the geographical pattern of the strength of the arrivals and the depth of the discontinuity are opposite to the seismological observations: in the seismically fast regions associated with a subducted slab the model predicts a very weak Scd phase and the discontinuity is depressed relative to the slow regions, where Scd arrivals are strong. The study favored a solid-solid phase change model and demonstrated that such a model with a velocity contrast of just 1% can predict both the geographical pattern and the amplitudes of the arrivals consistent with observations.

In this study, we elaborate on the results of Chapter 4 [1998] by modeling the dynamics of a phase change at the top of D". We consider a range of convection models with different characteristics of the phase change. The results of the convection calculations are used to produce seismic velocity fields. We then generate 2-D synthetics and analyze the waveforms for the presence of Scd phase, its lateral variations and correlation with dynamic features. Due to the complexity of both the modeled and observed wavetrains, we choose a statistical approach to compare the predicted relative amplitudes and differential travel times with the seismological observations. The predicted scale length of the heterogeneity in the computed velocity models are compared with those observed by *Lay et al.* [1997] in different regions of the world. This analysis is used to reject certain models and select a class of models with the

characteristics of the phase change that dynamically produce the most seismologically consistent velocity fields.

5.3 Dynamic models

We compute a variety of cases of convection models in a 2-D cylindrical coordinate system (r, ϕ). A solid-solid phase change is introduced close to the bottom of the model domain, with its characteristics varying between model cases. In the Boussinesq approximation of an incompressible fluid, the governing non-dimensional equations are:

$$\nabla \cdot (\mu \nabla \boldsymbol{u}) = -\nabla p + \frac{1}{\zeta^3} \alpha(r) Ra \left(T - \frac{1}{\alpha(r)} B_{\mathrm{ph}} \, \Gamma_{\mathrm{ph}} \right) \hat{\boldsymbol{r}}, \tag{5.1}$$

$$\frac{\partial T}{\partial t} = -(\boldsymbol{u} \cdot \nabla) T + \nabla^2 T + H, \tag{5.2}$$

$$\nabla \cdot \boldsymbol{u} = 0, \tag{5.3}$$

where all the quantities are dimensionless and $\boldsymbol{u}$ is velocity, r is radius, $\hat{\boldsymbol{r}}$ is a unit vector in the radial direction, p is pressure, T is temperature, t is time, μ is dynamic viscosity, α is coefficient of thermal expansion, and ζ is depth of the core-mantle boundary. We do not consider the effects of internal heating in this study and assume $H = 0$ in (5.2).

In equation (5.1), Γ_{ph} is a function that characterizes the phase of the mantle material at a particular location and can take values from 0, corresponding to the ambient, low-pressure phase, to 1, corresponding to the high-pressure phase. It can be written as [*Christensen and Yuen*, 1984]:

$$\Gamma_{\mathrm{ph}}(r, \phi) = \frac{1}{2} \left[1 + \tanh \left(\frac{1}{w_{\mathrm{ph}}} r_{\mathrm{ph}} \right) \right], \tag{5.4}$$

where w_{ph} is the non-dimensional width of the phase transition and r_{ph} is given by

$$r_{\mathrm{ph}}(r, \phi) = (1 - r) - (\zeta - h_{\mathrm{ph}}) - \gamma_{\mathrm{ph}} \left[T(r, \phi) - T_{\mathrm{ph}} \right] . \tag{5.5}$$

In equation (5.5) h_{ph} is the dimensionless elevation of the phase change above the CMB corresponding to dimensionless temperature T_{ph}, and γ_{ph} is the dimensionless Clapeyron ratio.

Dimensionless parameters r, $\boldsymbol{u}$, p, T, t, μ and α in equations (5.1)–(5.3) and w_{ph}, h_{ph}, T_{ph} and γ_{ph} in equations (5.4)–(5.5) refer to the corresponding dimensional values by means of the following scaling relations:

$$r^* = R_0 r \,, \tag{5.6}$$

$$\boldsymbol{u}^* = \frac{\kappa}{R_0} \boldsymbol{u} \,, \tag{5.7}$$

$$p^* = \frac{\kappa \bar{\mu}}{R_0^2} p \,, \tag{5.8}$$

$$T^* = T_S + \triangle T\, T \,, \tag{5.9}$$

$$t^* = \frac{R_0^2}{\kappa} t \,, \tag{5.10}$$

$$\mu^* = \bar{\mu} \mu \,, \tag{5.11}$$

$$\alpha^* = \bar{\alpha} \alpha \,, \tag{5.12}$$

$$w_{\mathrm{ph}}^* = R_0 w_{\mathrm{ph}} \,, \tag{5.13}$$

$$h_{\mathrm{ph}}^* = R_0 h_{\mathrm{ph}} \,, \tag{5.14}$$

$$T_{\mathrm{ph}}^* = T_S + \triangle T T_{\mathrm{ph}}, \tag{5.15}$$

$$\gamma_{\mathrm{ph}}^* = \frac{\rho_0 g R_0}{\triangle T} \gamma_{\mathrm{ph}} \,, \tag{5.16}$$

where R_0 is the radius of the Earth, κ is the thermal diffusivity, $\bar{\mu}$ and $\bar{\alpha}$ are the volume averaged mantle viscosity and thermal expansivity, respectively, $\triangle T$ is the non-adiabatic temperature increase across the mantle, T_S is the temperature at the surface of the Earth, ρ_0 is the average mantle density, and g is the gravitational acceleration (Table 5.1). Asterisks in (5.6)–(5.16) denote dimensional values and will be dropped in all subsequent equations for clarity.

Parameter Ra in equation (5.1) is the thermal Rayleigh number that characterizes

Table 5.1: Values of parameters used in convection computations

Parameter	Symbol	Value
Radius of the Earth	R_0	6371 km
Depth of the CMB	D	2891 km
Gravity acceleration	g	10 m/s^2
Average mantle density	ρ_0	4.0 g/cm^3
Average mantle viscosity	$\bar{\mu}$	3.16×10^{21} Pa·s
Thermal diffusivity	κ	10^{-6} m^2/s
Average thermal expansivity	$\bar{\alpha}$	1.535×10^{-5} K^{-1}
Temperature increase across the mantle	$\triangle T$	2900 K
Velocity of subducting plate	U_{plate}	5 cm/yr
Trench migration velocity	U_{trench}	0.5 cm/yr

the vigor of convection of the system and is given by

$$Ra = \frac{g\bar{\alpha}\rho_0 \triangle T D^3}{\kappa\bar{\mu}},$$ (5.17)

where D is the depth of the core-mantle boundary (Table 5.1).

Parameter B_{ph} in (5.1) characterizes the intrinsic buoyancy of the high-pressure phase with respect to the thermal buoyancy and is given by

$$B_{\mathrm{ph}} = \frac{\triangle\rho_{\mathrm{ph}}}{\rho_0\bar{\alpha}\triangle T},$$ (5.18)

where $\triangle\rho_{\mathrm{ph}}$ is the density increase associated with the transition to the high-pressure phase.

Calculations are performed for a half-annulus (Figure 5.1), where the inner radius corresponds to the CMB and the outer radius corresponds to the surface of the Earth. Free slip conditions are used at the bottom; reflection boundary conditions are used on the two side walls. At the top, plates are simulated by imposing velocity boundary conditions, where the amplitudes of the plate velocities are determined from a free slip calculation (e.g., [*Gurnis and Davies*, 1986]). *Han and Gurnis* [1999] have shown that although such boundary conditions do substantial work on the system, the work is dissipated within the lithosphere. Consequently, the approach is quite adequate
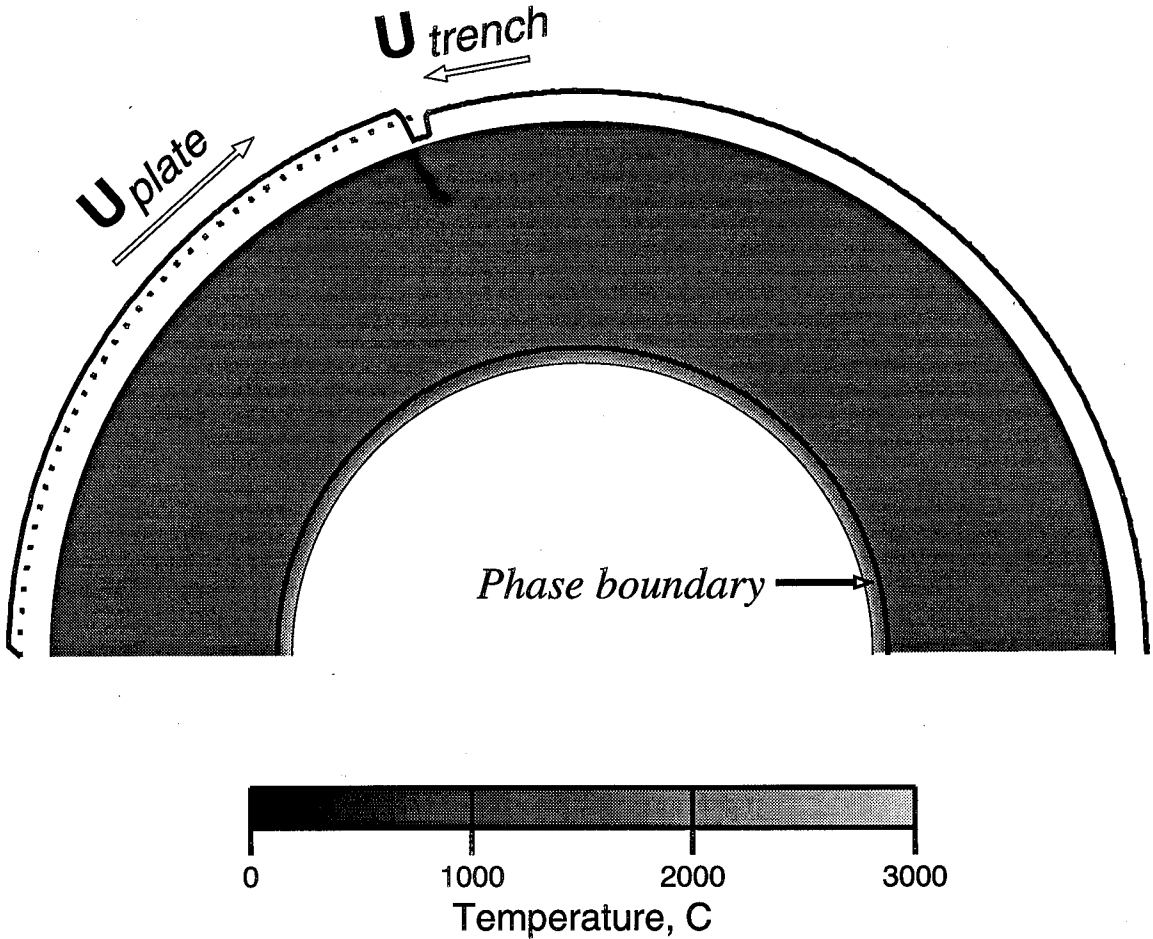
Figure 5.1: Temperature field after 20 million years of subduction. The imposed surface velocity conditions are indicated at the top (the dotted line shows zero velocity).

for studies including the dynamics of the bulk of the fluid layer. A velocity overshoot is applied in the back-arc basin to facilitate subduction and detachment of the slab from the overriding plate [*Christensen*, 1996a; *Davies*, 1997]. The subducting plate is moving at $U_{\text{plate}} = 5$ cm/yr and a trench rollback is added with the migration velocity of the trench $U_{\text{trench}} = 0.5$ cm/yr. The velocity of the overriding plate is taken equal to U_{trench}.

The mantle is initially isothermal with superimposed top and bottom thermal boundary layers. The thermal boundary layer for the oceanic lithosphere of the subducting plate is computed using an infinite half-space cooling model. The age of the lithosphere at the initial trench location is approximately 160 million years. For the bottom boundary layer and the continental lithosphere (overriding plate) an

initial age of 100 million years is used. The total temperature variation across the mantle is taken $\triangle T = 2900$ K, with equal partitioning of the variation between the lower and bottom boundary layers.

The depth dependence of the dimensionless coefficient of thermal expansion is given by

$$\alpha(r) = \frac{2.93}{1 + 10.5(1 - r)^{0.85}} , \tag{5.19}$$

and is consistent with the experimental data for olivine at the surface and predictions of experimental mineral physics for a silicate perovskite and magnesiowüstite assemblage in the lower mantle (Chapter 2).

A depth and temperature-dependent dynamic viscosity, μ is used in (5.1). The depth dependence includes an order of magnitude increase at the 670 km boundary between the upper and lower mantle. The temperature dependent part (Figure 5.2) is given by

$$\mu(T) = \exp \left\{ \frac{c_1}{c_2 + T} - \frac{c_1}{c_2 + 0.5} \right\} . \tag{5.20}$$

Since stress dependence is expected to significantly reduce the effective viscosity of the subducting lithosphere [*Christensen*, 1984] but is not accounted for in the computations, a cutoff of 10 is applied at low temperatures. We use $c_1 = 41.5$ and $c_2 = 0.77$ in (5.20). These values provide a substantially stronger temperature dependence of viscosity than used in Chapters 3 and 4, producing a more realistic 4 orders of magnitude variation in the bottom thermal boundary. As in Chapters 3 and 4, viscosity is normalized to ensure that the volume average of $\log \mu$ is 0 when averaged over the entire duration of the simulation.

Equations (5.1)–(5.3) are solved using a finite element code ConMan [*King et al.*, 1990] which has been modified for the cylindrical geometry by *Zhong and Gurnis* [1993]. The computations were carried out on a mesh with 400 elements in the azimuthal direction and 100 elements in the radial direction. The mesh was refined both vertically in the top and bottom thermal boundary layers and laterally around the trench, so that the resolution at these regions was about 12 km in either direction.

We consider a number of models by varying γ_{ph} from -10 to $+10$ MPa/K and
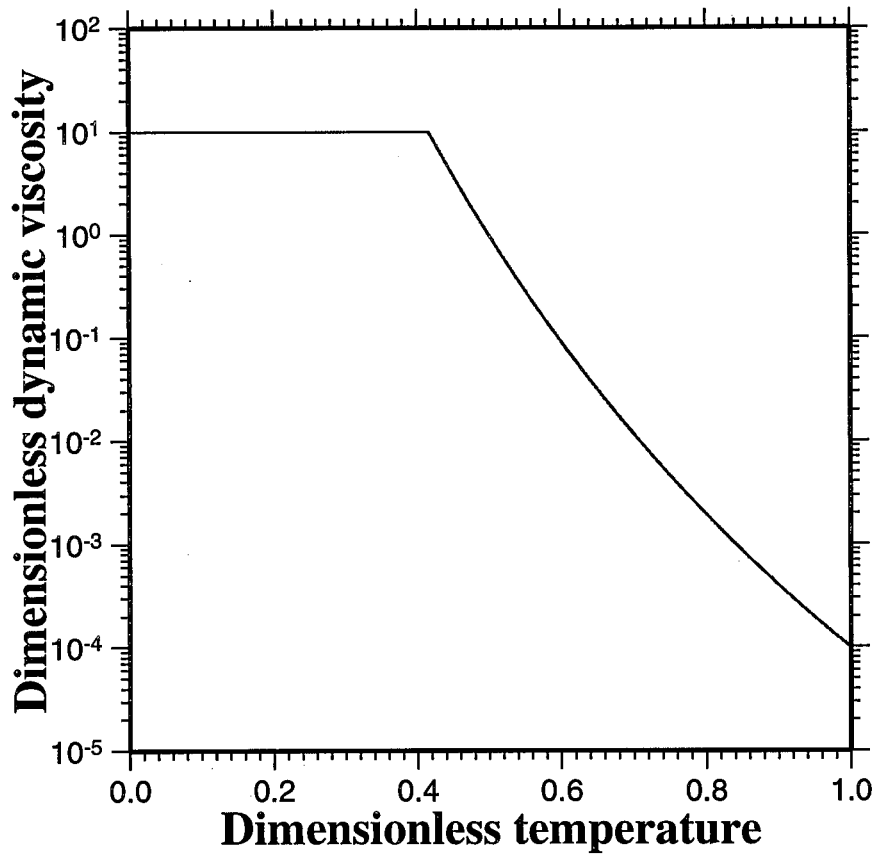
Figure 5.2: Temperature dependence of viscosity.

h_{ph} from 100 to 300 km. In order to produce a sharp seismic discontinuity, we use a narrow phase transition with $w_{\mathrm{ph}} = 3$ km. The density change associated with the phase transition is taken to be either 0% (passive phase) or 1%.

All models were integrated for a total time of 340 million years. Figure 5.3 illustrates the general influence of the basal phase change on the dynamics of the system. In the case of a passive phase change with $\gamma_{\mathrm{ph}} = 6$ MPa/K, $h_{\mathrm{ph}} = 150$ km (Figure 5.3a), the phase change does not have any influence on the dynamics but will have a substantial influence on the predicted seismic signature. As the slab subducts to the base of the mantle, it spreads atop the core-mantle boundary with some folding and buckling developing in the bottom part of the slab. The slab rests almost horizontally at the base of the mantle and is steeply dipping in the mid-mantle.

The bottom boundary layer grows in thickness and eventually becomes gravitationally unstable, giving rise to hot plumes. Large plume heads erupting from the CMB and quickly rising to the surface are followed by relatively thin hot tails. In some cases, as a new instability is created in the bottom boundary layer, a new plume head erupts in the same location, following an existing plume tail. In other cases, new plumes erupt from different regions of the CMB with the old tails eventually remixed with the bulk of the flow. The strongest and the most stable (with multiple heads erupting in pulses from approximately the same location at the CMB) plume always seems to emerge just at the tip of the slab. It is also always the first plume to emerge, caused by the local thickening of the hot thermal boundary layer by the slab.

The phase boundary is elevated through the flat lying slab and reaches its greatest height where the slab first reaches the CMB. In the hot areas, the phase boundary is depressed and the phase transition does not occur in the hot plume tails or when new plume heads erupt from the CMB. The continuity of the boundary becomes intermittent in hot areas with most variation occurring near plumes or the boundary between the flat lying slab and erupting plume.

Our next model has the same Clapeyron slope (6 MPa/K) and elevation of the phase transition above the CMB (150 km), but the high-pressure phase is assumed
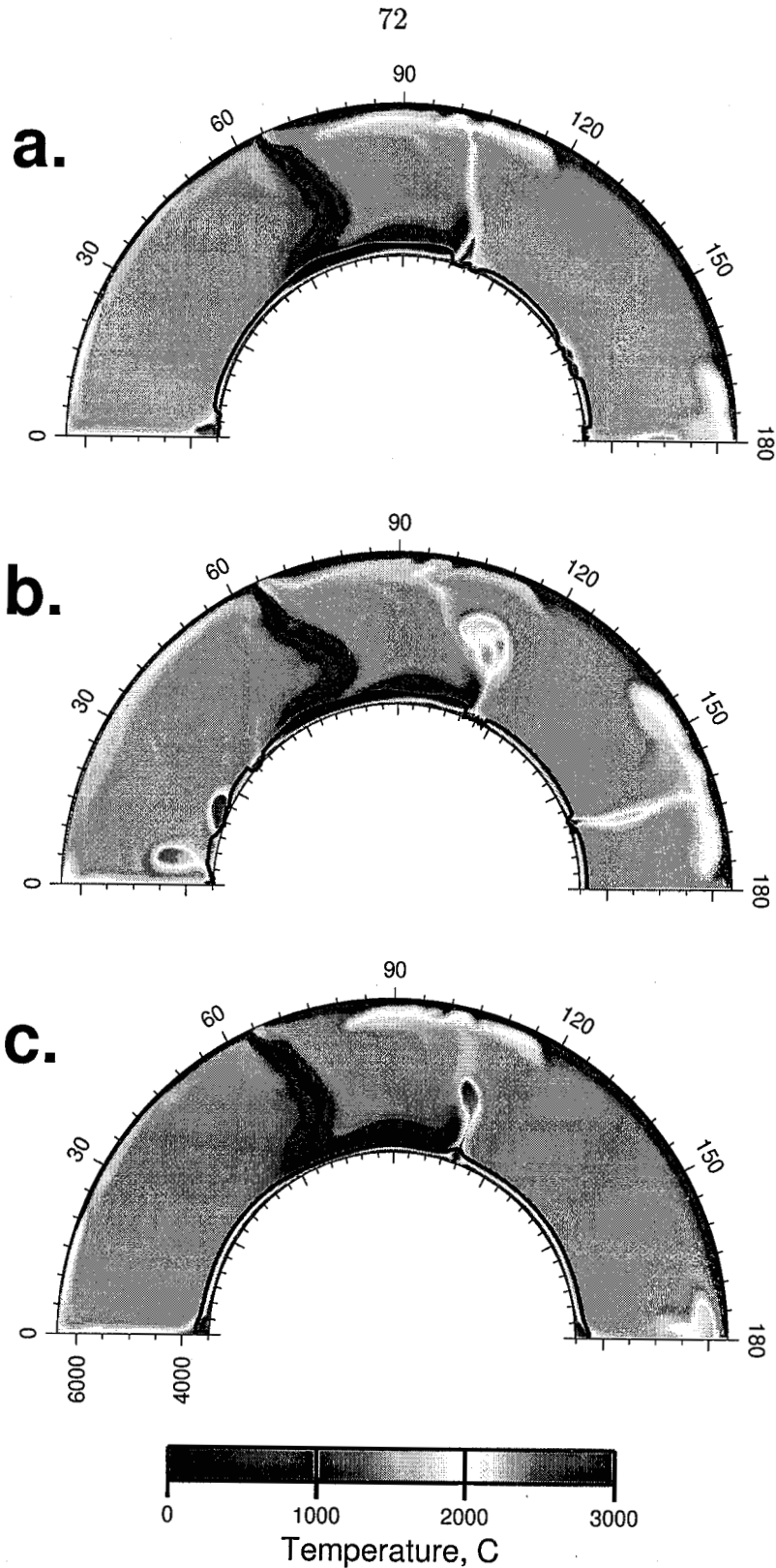
Figure 5.3: Temperature fields and location of the phase boundary after 340 million years of subduction for three different models: a) $\triangle\rho_{ph}/\rho_0 = 0$, $\gamma_{ph} = 6$ MPa/K, $h_{ph} = 150$ km; b) $\triangle\rho_{ph}/\rho_0 = 0.01$, $\gamma_{ph} = 6$ MPa/K, $h_{ph} = 150$ km; c) $\triangle\rho_{ph}/\rho_0 = 0.01$, $\gamma_{ph} = -6$ MPa/K, $h_{ph} = 150$ km.

to be 1% denser than the low-pressure phase. For this model the overall pattern of convection is only moderately changed (Figure 5.3b). Plumes become stronger and more common, as can be observed in Figure 5.3b, where after the same time of integration a second plume head has emerged at the tip of the slab and the head of the rightmost plume is much wider and spread beneath the surface than in the case of a passive phase change (Figure 5.3a). On the other hand, the effect of a greater phase density on the subducting slab is subtle. This is probably explained by the high viscosity of the slab and the continuity of the plate tectonic model which continuously supplies a substantial amount of negative buoyancy at a steady rate. The strength of the basal phase change only weakly influences the driving force on the lower mantle slab.

Using a negative Clapeyron slope $\gamma_{ph} = -6$ MPa/K with a 1% density contrast (Figure 5.3c), again, has a limited effect on the dynamics of the slab. However, such a phase change significantly inhibits the formation of plumes. This observation agrees well with the results of a study of *Breuer et al.* [1998] for the Martian mantle which has been interpreted by them as "thermal barriers" which are created by the phase change due to latent heat consumption. The phase boundary now becomes a global feature, depressed in the cold region associated with the slab but elevated where plumes emerge from the CMB. It generally appears smoother than in the cases of a positive γ_{ph} because of the smoother temperature gradients which exist a few hundred kilometers from the CMB.

5.4 Synthetic waveforms

To select a class of dynamic models consistent with seismological observations, we transform the temperature field obtained from the convection models into a seismic velocity field. A PREM-like structure is used for the upper mantle and a technique presented in Chapter 2 is applied to compute the elastic parameters and density in the lower mantle (Figure 5.4). The computations start from an adiabatic model of the lower mantle, obtained to provide the best fit to PREM and based on the mineral

physics data and geochemical constraints. The results of convection computations (the temperature field and the distribution of the phases) are then used to add the non-adiabatic perturbations to the adiabatic parameters. Following the results from [*Sidorin et al.*, 1998], we assume a 1% shear velocity increase across the phase boundary. As the shear velocity is controlled by both density, ρ, and shear modulus, G, different changes in the shear modulus are required for a passive and a denser phase change to provide a 1% velocity jump. We estimated that a roughly 2% jump in shear modulus is needed for cases with no density difference between the phases and 3% jump for a 1% density change.

Using the computed seismic velocity fields, we produce synthetic waveforms which are compared with the observations. We limit our analysis to the horizontally polarized shear wave (SH) as some of the best seismological observations of the D″ triplication pertain to the Scd$_\text{H}$ phase. A combination of a WKM method and generalized ray theory (GRT) is used to compute the waveforms in a 2-D seismic velocity field [*Ni et al.*, 1999]. A 600 km deep point source is assumed in all computations.

To study the spatial variations of the computed waveforms, we compute waveforms for a set of raypaths with a fixed epicentral distance $\triangle$ but different locations of the source and receiver. This representation of the wavefield is widely used in exploration geophysics and is known as a constant offset section. The construction of such section is illustrated in Figure 5.4a, where a source-receiver pair with a fixed separation $\triangle = 80°$ is moved around the domain by shifting it by a constant azimuth increment $\triangle\phi = 40°$. Any location of the source-receiver pair can be characterized by the azimuthal coordinate ϕ_refl of the ScS bouncing point and so the corresponding waveforms can be plotted as a function of ϕ_refl that characterizes the location at the CMB that is sampled by the paths. To allow sampling of the deep mantle near the side walls of the model, the seismic velocity field was symmetrically continued to a full annulus in a way consistent with the reflecting boundary conditions used on the side walls in the convection model. This continuation allows us to cover the whole model domain with seismic rays so that ϕ_refl can vary from 0° to 180°. We computed constant offset sections for $\triangle = 75°$, 77°, 79°, 81° and 83° using an azimuth increment $\triangle\phi = 1°$.
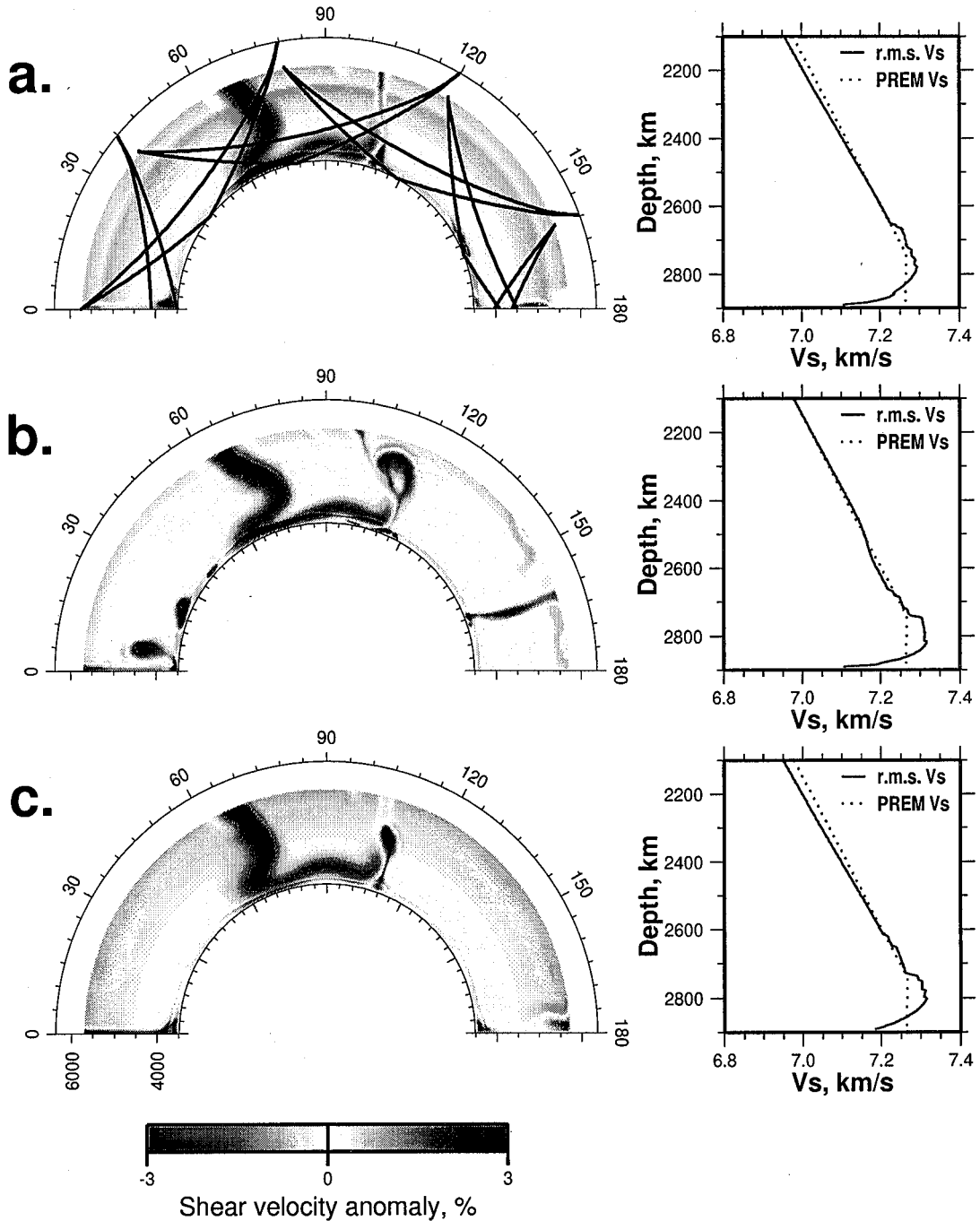
Figure 5.4: Shear velocities computed for the convection models in Figure 5.3. A 1% velocity jump is assumed at the phase boundary. A r.m.s value of the shear velocity at each depth (shown on the right with PREM values for a reference) was subtracted to produce the anomaly at any given point plotted on the left. The top figure illustrates the procedure used to compute a constant offset section: a source receiver pair with a fixed separation ($\triangle = 80°$) is shifted by a constant azimuth increment $\triangle\phi$ to compute waveforms for different values of the ScS bouncing point ϕ-coordinate, ϕ_{refl}; for each location of the source-receiver pair S and ScS rays are plotted.

This set of epicentral distances corresponds to the range where Scd is a sufficiently strong arrival and is still distinguishable from the direct arrival.

Three constant offset sections for $\triangle = 75°$, 79° and 83° computed for a model with $\triangle\rho_{\rm ph} = 0$, $\gamma_{\rm ph} = 6$ MPa/K and $h_{\rm ph} = 150$ km are given in Figure 5.5, with a part of the section for $\triangle = 79°$ enlarged in Figure 5.6. The sections clearly show an intermittent D" triplication, with Scd arrival being sufficiently strong only in a limited region, primarily in the area with $50° < \phi_{\rm refl} < 100°$. Comparison with the seismic structure in Figure 5.4a reveals that this area corresponds to a broad fast shear velocity anomaly associated with the subducted slab. Away from the slab, Scd can still be observed for $\triangle = 83°$, although with a considerably reduced amplitude, with no trace of an Scd found for smaller epicentral distances.

Although lacking the additional complexity of source mechanisms and instrument response, the computed waveforms display strong variations in amplitudes and arrival times of various phases, especially Scd. While such variations are commonly observed, it proves difficult to make a direct comparison of the modeling results with the waveform data and some other technique must be used. We choose a statistical approach here, where the first moments of differential travel times and relative amplitudes distributions are compared for the computed results and data.

To facilitate this comparison, the phases (S, ScS and Scd) are picked automatically (see dashed lines in Figure 5.6) from the synthetic seismograms using a simple algorithm. The direct phase and phase reflected from the core present no difficulties, while certain problems exist with Scd phase. On many waveforms the phase is weak (or completely absent) and may be lost in the noise. In addition, on some waveforms an additional arrival, St, is observed (Figure 5.6) between S and ScS, linked by *Sidorin et al.* [1998] to the seismic structure produced by thermal gradients within a folding slab. When more than one phase is suggested for Scd by the phase-picking algorithm, the one with a significantly higher amplitude or, if the amplitudes are comparable, the sharper phase (the phase with a higher absolute value of acceleration) is accepted. To minimize the erroneous picks we set a threshold, rejecting a Scd pick if the amplitude of the phase is less than 10% of the amplitude of the direct arrival.
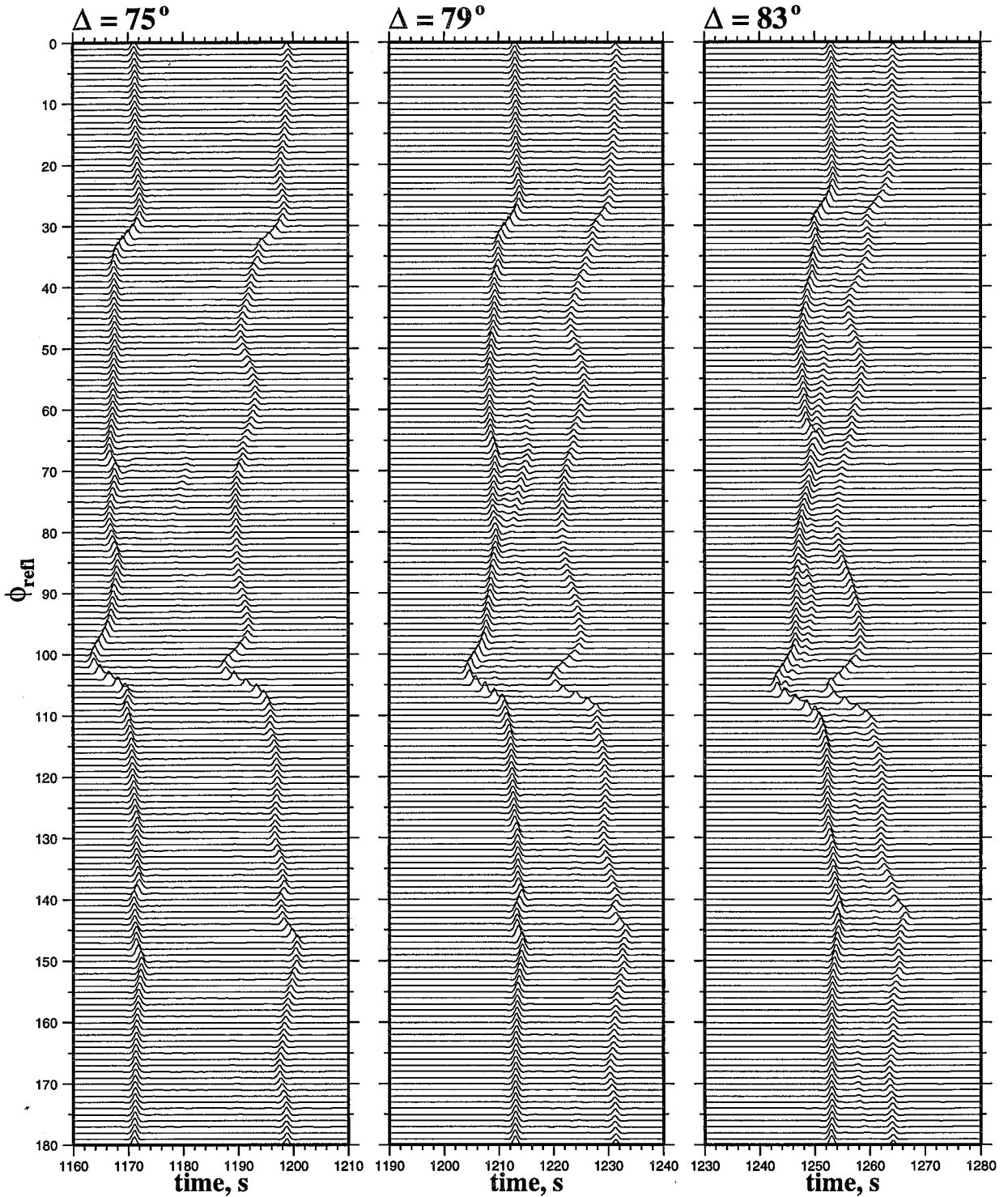
Figure 5.5: Constant offset sections for $\triangle = 75°$ (left), $\triangle = 79°$ (middle) and $\triangle = 83°$ (right) computed for a model with $\triangle \rho_{ph}/\rho_0 = 0$, $\gamma_{ph} = 6$ MPa/K, $h_{ph} = 150$ km. The first arrival is the direct S, the last arrival is the core reflection, ScS. Scd arrivals can be observed between S and ScS in some regions.
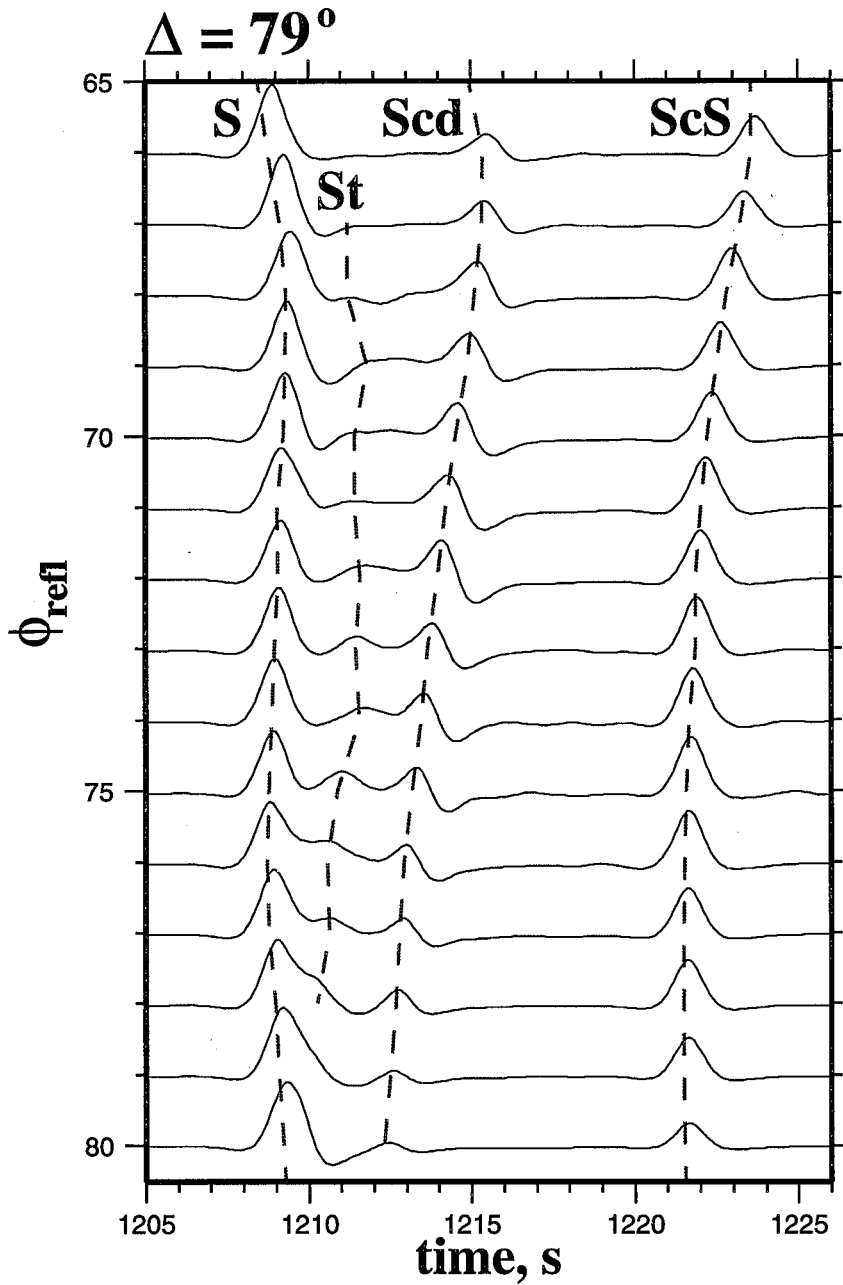
Figure 5.6: Constant offset section for $\triangle = 79°$ for a model with $\triangle\rho_{ph}/\rho_0 = 0$, $\gamma_{ph} = 6$ MPa/K, $h_{ph} = 150$ km, enlarged for $65° \leq \phi_{refl} \leq 85°$. The four phases (S, St, Scd and ScS) are indicated by the dashed lines (the picks were obtained automatically).

The first-order moment of the amplitudes and travel times distributions for the data can be characterized by a 1-D seismic velocity reference model that is produced to provide the best fit to the observations. Several such models have been advanced for various regions of the world with a clear evidence for a D" triplication. In this study we consider four such regions: northern Siberia, Alaska, India and Indian Ocean, and Central America, characterized by their respective 1-D reference models SGLE, SYLO, SYL1 and SLHA (Figure 1.1).

We introduce three parameters – $\triangle M_1^A$, $\triangle M_1^T$ and $\triangle M_2^T$ that we use to characterize the overall statistical misfit between the amplitudes and travel times of waveforms produced for a computed model and the data for a given region of the world. Parameter $\triangle M_1^A$ will be used to characterize the difference between the first central moments of relative amplitudes distributions for the synthetics and the data. Parameters $\triangle M_1^T$ and $\triangle M_2^T$ will be used to characterize the difference between the first moments and the second moments, respectively, of the differential travel times distributions.

5.4.1 Comparison of relative amplitudes

Figure 5.7 shows Scd/S amplitude ratios computed for the model with a passive phase with $\gamma_{ph} = 6$ MPa/K and $h_{ph} = 150$ km. The amplitude ratios are normalized by the respective ratios for four different 1-D reference models and are plotted as a function of the ScS bounce point coordinate, ϕ_{refl}. There are obviously large variations in the relative Scd amplitudes and, at least in some regions, these amplitudes are consistent with the relative amplitudes observed for the paths through northern Siberia, Alaska, India and Central America. Using this observation we restrict the analysis of the computed models to the range $50° < \phi_{refl} < 90°$. This region in the models corresponds to the most distinct Scd arrivals and its lateral extent is comparable to that of many areas in the world with stable observations of the D" triplication [*Lay et al.*, 1997]. This is also the region of a broad fast velocity anomaly at the base of the mantle caused by the thermal signature of the subducted slab, so that the dynamic context of this region is similar to the four geographical regions that we consider, each
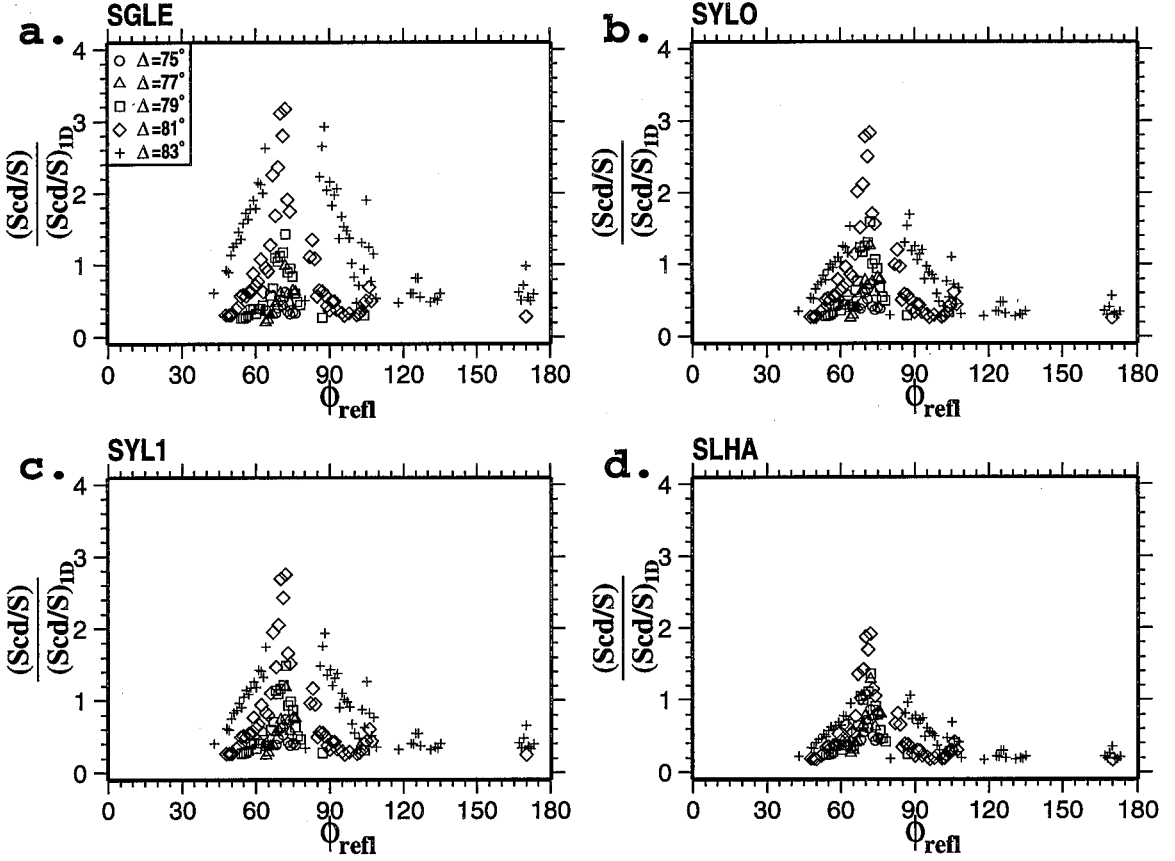
Figure 5.7: Scd/S amplitude ratios computed for the model with $\triangle \rho_{ph}/\rho_0 = 0$, $\gamma_{ph} = 6$ MPa/K, $h_{ph} = 150$ km. The amplitude ratios are normalized by the respective ratios (for the corresponding epicentral distances) for four different 1-D reference models: a – SGLE, b – SYLO, c – SYL1, d – SLHA. The amplitudes are plotted as a function of the ScS bounce point coordinate, ϕ_{refl}, with different symbols corresponding to different epicentral distances.

of which has either ongoing subduction or substantial subduction since the Mesozoic.

No systematic study has yet addressed the Scd/S amplitude variations in the waveforms that display the D" triplication. In fact, the effects of the deep structure would be difficult to isolate in such variations due to variable radiation patterns, station effects and attenuation along the raypaths. Although the relative amplitudes provide weaker constraints on the 1-D reference models than the differential travel times, for the purposes of our analysis we assume that Scd/S in the observed waveforms are scattered (with no systematic shift) around the $(Scd/S)_{1D}$ values of the 1-D reference model for the corresponding region, so that $\langle (Scd/S)_{data}/(Scd/S)_{1D} \rangle = 1$. Using this

assumption we introduce the parameter $\triangle M_1^A$ as

$$\triangle M_1^A(\text{model}, \text{ref1D}) = \left| 1 - \left\langle \frac{(\text{Scd/S})_\text{model}}{(\text{Scd/S})_\text{ref1D}} \right\rangle \right| . \qquad (5.21)$$

Parameter (5.21) gives a quantitative measure of closeness of the average amplitude ratios for a computed model to those for the real data in a given region (characterized by the 1-D reference model ref1D). Large values of $\triangle M_1^A$ correspond to large deviations of relative amplitudes from the 1-D reference model amplitudes that represent the average values for the data in the particular region.

5.4.2 Comparison of differential travel times

A comprehensive study of the Scd-S, ScS-Scd and ScS-S differential travel times distribution in three different regions (northern Siberia, Alaska and India) was recently carried out by *Lay et al.* [1997]. It was demonstrated that the differential travel times $(\delta T_X)_\text{ref1D} = T_X - (T_X)_\text{ref1D}$ (where X is Scd-S, ScS-Scd or ScS-S) have a zero mean (first-order moment of the distribution) for Siberia and Alaska, while for India the 1-D reference model (SYL1) has a baseline shift so that the corresponding mean values are approximately $\langle \delta T_{\text{Scd}-\text{S}} \rangle_\text{SYL1} = 1.7$, $\langle \delta T_{\text{ScS}-\text{Scd}} \rangle_\text{SYL1} = -1.8$ and $\langle \delta T_{\text{ScS}-\text{S}} \rangle_\text{SYL1} = -0.1$. For the purposes of our analysis, however, we choose to use the median estimates as they are more robust and tolerant to points with large departures from the bulk of the set, such as is expected in the case of misidentified phases. The median of the differential travel times for Siberia and Alaska approximately coincide with the mean estimates and are equal to zero. In the case of India, the medians of the differential travel times with respect to model SYL1 are $m_e \left(\delta T_{\text{Scd}-\text{S}} \right)_\text{SYL1} = 1.5$, $m_e \left(\delta T_{\text{ScS}-\text{Scd}} \right)_\text{SYL1} = -1.5$, $m_e \left(\delta T_{\text{ScS}-\text{S}} \right)_\text{SYL1} = 0.3$. A study for the Central America [*Lay and Helmberger*, 1983] suggests that model SLHA has no baseline shift and the differential travel times have zero medians.

Using these estimates, summarized in Table 5.2, we introduce parameter $\triangle M_1^T$ as

$$\triangle M_1^T(\text{model}, \text{ref1D}) =$$

$$\frac{1}{\sqrt{3}} \left\{ \sum_{X=\{\text{Scd}-\text{S}, \text{ScS}-\text{Scd}, \text{ScS}-\text{S}\}} [m_e \left(\delta \text{T}_X \right)_{\text{model}} - m_e \left(\delta \text{T}_X \right)_{\text{ref1D}}]^2 \right\}^{1/2} . \quad (5.22)$$

This parameter serves as a measure of the average shift between the median travel times from a computed model and the data (characterized by the reference 1-D model ref1D). Large values of $\triangle M_1^\mathsf{T}$ correspond to a large shift between the median travel times for the computed model and the data for a particular region.

Similar to the approach used by *Lay et al.* [1997] for regional data, in Figure 5.8 we present the correlations of the differential travel times for a model with a passive phase and $\gamma_{\text{ph}} = 6$ MPa/K, $h_{\text{ph}} = 150$ km. Such representation of the travel times scatter is informative because it allows us to make comparisons between the travel times for a computed model and for a particular geographical region. First, the shift of the medians of the computed travel times (represented by large solid circles) from the respective medians for the data (Table 5.2) characterizes the baseline shift for the computed model. Second, implications can be derived from the analysis of the correlations of the individual travel times. And, finally, the scatter of the travel times around the medians presents an important characteristic of the structure producing the waveforms and can be used to compare models. We characterize this scatter by the difference, $\triangle_{90\%}(\delta T_X)$, between the 95% and 5% quantiles of the distribution, which is computed by stripping 5% of the smallest and 5% of largest values in the data set and taking the range of variation in the remaining 90%. We prefer this measure of scatter to the more common variance for the same reasons as we chose medians over the means: higher robustness and tolerance to misidentified phases. We estimate the values of $\triangle_{90\%}(\delta T_X)$ for the data in the northern Siberia, Alaska and India from the analysis presented by *Lay et al.* [1997]. The value of $\triangle_{90\%}(\delta T_{\text{ScS}-\text{Scd}})$ for the Central America region is estimated from the results of [*Lay and Helmberger*, 1983] and the results of [*Lay*, 1983] are used to derive the value of $\triangle_{90\%}(\delta T_{\text{ScS}-\text{S}})$ for that region. No analysis of Scd-S travel times has been performed for Central America so the value of $\triangle_{90\%}(\delta T_{\text{Scd}-\text{S}})$ for the region is chosen to keep the approximate proportions between the various travel times scatter that are observed for the other three regions.
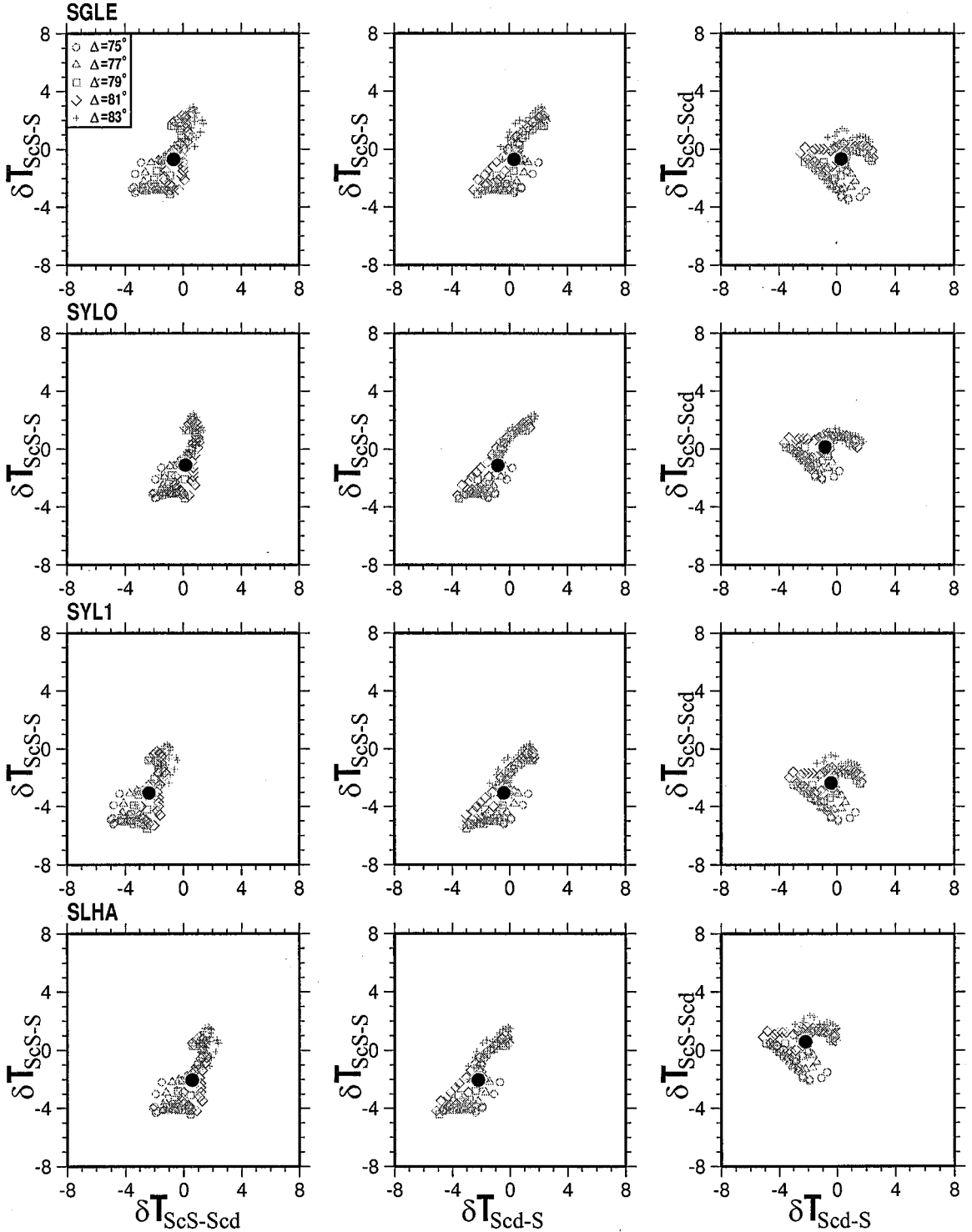
Figure 5.8: Correlation of differential travel times (in seconds) for a model with a passive phase and $\gamma_{ph} = 6\,\mathrm{MPa/K}$, $h_{ph} = 150\,\mathrm{km}$. The travel times were computed for five different epicentral distances (indicated by different symbols) for all the raypaths with $50° < \phi_{refl} < 90°$ and differenced with four different 1-D reference models. The large circles correspond to the median values.

Table 5.2: Median values of the seismologically observed differential travel times distribution around the 1-D reference models for the corresponding regions

Geographic region	Reference 1-D model	$m_e(\delta T_{\mathrm{Scd-S}})$	$m_e(\delta T_{\mathrm{ScS-Scd}})$	$m_e(\delta T_{\mathrm{ScS-S}})$
Northern Siberia[a]	SGLE	0s	0s	0s
Alaska[a]	SYLO	0s	0s	0s
India[a]	SYL1	1.5s	−1.5s	0.3s
Central America[b]	SLHA	0s	0s	0s

[a] Medians estimated using the data from [*Lay et al.*, 1997].

[b] Medians estimated using the data from [*Lay and Helmberger*, 1983].

Table 5.3 lists the values of $\triangle_{90\%}(\delta T_X)$ for the four geographical regions. To characterize the difference in scatter of the travel times produced by the computed structure and the data in a particular geographic region, we introduce parameter $\triangle M_2^{\mathsf{T}}$ as

$$\triangle M_2^{\mathsf{T}}(\text{model}, \text{ref1D}) =$$
$$\frac{1}{\sqrt{3}} \left\{ \sum_{X=\{\mathrm{Scd-S,ScS-Scd,ScS-S}\}} [\triangle_{90\%}(\delta \mathrm{T}_X)_{\text{model}} - \triangle_{90\%}(\delta \mathrm{T}_X)_{\text{ref1D}}]^2 \right\}^{1/2} . \quad (5.23)$$

Models that produce significantly smaller or larger differential travel times scatter than is observed in a given region characterized by a reference model ref1D will have larger values of $\triangle M_2^{\mathsf{T}}(\text{model}, \text{ref1D})$ than models that produce scatter of about the same amplitude.

Using parameters $\triangle M_1^{\mathsf{A}}$, $\triangle M_1^{\mathsf{T}}$ and $\triangle M_2^{\mathsf{T}}$, we introduce a penalty function

$$p(\text{model}, \text{ref1D}) =$$
$$\frac{1}{3} \left[\widehat{\triangle M_1^{\mathsf{A}}}(\text{model}, \text{ref1D}) + \widehat{\triangle M_1^{\mathsf{T}}}(\text{model}, \text{ref1D}) + \widehat{\triangle M_2^{\mathsf{T}}}(\text{model}, \text{ref1D}) \right] \quad (5.24)$$

that characterizes the overall statistical misfit between a computed model and seismic data. It allows to compare any two models in a class of computed models in terms of statistical proximity to the data in a given region of the world. The lower the value of $p(\text{model}, \text{ref1D})$ for a given model, the better fit the model provides to the seismic

Table 5.3: Scatter (difference between the 95% and 5% quantiles) of the differential travel times in the different geographical regions

Geographic region	Reference 1-D model	$\triangle_{90\%}(\delta T_{\text{Scd}-\text{S}})$	$\triangle_{90\%}(\delta T_{\text{ScS}-\text{Scd}})$	$\triangle_{90\%}(\delta T_{\text{ScS}-\text{S}})$
Northern Siberia[a]	SGLE	6.5s	4.5s	5.5s
Alaska[a]	SYLO	6.0s	4.5s	4.5s
India[a]	SYL1	5.0s	3.5s	5.5s
Central America	SLHA	6.5s[b]	5.0s[c]	6.0s[d]

[a] Scatter estimated using the data from [*Lay et al.*, 1997].
[b] Assumed value.
[c] Estimated using the data from [*Lay and Helmberger*, 1983].
[d] Estimated using the data from [*Lay*, 1983].

data observed in the region characterized by the 1-D reference model ref1D.

Parameters $\triangle\widehat{M_1^{\text{A}}}$, $\triangle\widehat{M_1^{\text{T}}}$ and $\triangle\widehat{M_2^{\text{T}}}$ in (5.24) represent the normalized values of $\triangle M_1^{\text{A}}$, $\triangle M_1^{\text{T}}$ and $\triangle M_2^{\text{T}}$, respectively. The normalization is performed for a class of computed models to ensure that parameters (5.21)-(5.23) in (5.24) vary in the range from 0 to 1 and thus have equal weights in the penalty function.

5.4.3   Comparison results

The penalty function introduced above presents a comparison criterion, based on which any two computed models can be compared in a sense of the quality of fit of predicted waveforms to the regional data. In Figure 5.9 we plot the comparison results for the models that have been computed. As a passive phase change does not produce any dynamic effects on the flow, a single convection model can be used to study in detail the influence of parameters γ_{ph} and h_{ph} on the resulting seismic structure and the corresponding waveforms. Filled circles in Figure 5.9 represent models computed for $\triangle\rho_{\text{ph}}/\rho_0 = 0$ (passive phase) and the open circles correspond to the few models where the high-pressure phase is 1% denser than the lower-pressure phase. The difference in the penalty functions for models with a passive phase and a denser phase is rather small for the same values of γ_{ph} and h_{ph} which is clearly seen in Figure 5.9, where the adjacent filled and open circles have similar sizes. This is in

agreement with our observation of the small effect of a minor (1%) density increase in the phase transition on the dynamics of the slab discussed earlier.

Variations in γ_{ph} and h_{ph}, on the other hand, lead to stronger variations in the seismic structure and the resulting waveforms. As Figure 5.9 suggests, a preference should be given to phase changes with a positive value of Clapeyron slope of about 6 MPa/K and the elevation of about 150 km above CMB under adiabatic conditions. A positive value of Clapeyron slope corresponds to exothermic phase changes, where latent heat is released when the phase change occurs. Such phase changes present a barrier to rising plumes, as when the phase change occurs in a rising plume, the latent heat is consumed which leads to the plume losing some of its buoyancy. The higher the temperature, the higher the pressure at which such a phase change occurs. Negative values of Clapeyron slope correspond to endothermic phase change, where latent heat is consumed. Such phase changes present barriers to downwellings (slabs) and for higher temperatures the phase transition pressure is lower. The absolute value of the Clapeyron slope characterizes the variation of the depth of the discontinuity with temperature.

Our best estimate of the elevation of the phase change above the CMB (150 km) corresponds to roughly 127 GPa and 2650 K on a (P, T) diagram. Models with these characteristics provide the best fit to the structure under the northern Siberia (model SGLE), closely followed by the structure under Alaska (model SYLO). The match for the structures under India and Central America is significantly worse.

5.4.4   Analysis of the predicted heterogeneity

To explore the scale lengths of the heterogeneity in our computed models, we use a method of *Lavely et al.* [1986] that was recently applied by *Lay et al.* [1997] to the data in three different regions. The idea behind the method is to approximate the spectrum of mantle heterogeneity by a spatial autocorrelation function of the travel times residuals. This is done by computing the mean and variance of the travel times residuals between all raypaths with a given lateral separation of the ScS reflection
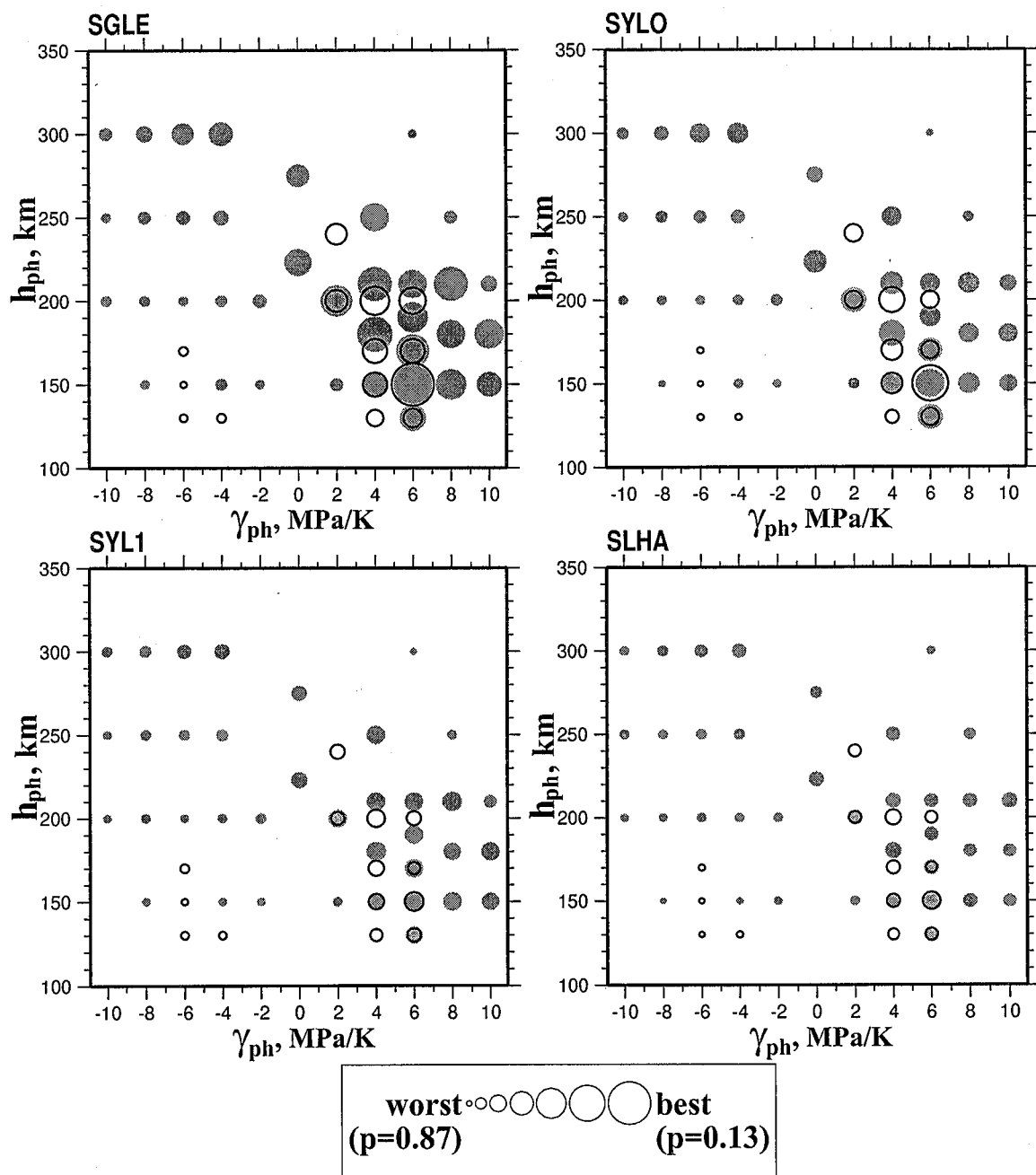
Figure 5.9: Comparison of computed models with different phase change characteristics. Each circle represents a model, with the size inversely proportional to the penalty function for that model and one of the four (SGLE, SYLO, SYL1 and SLHA) 1-D reference models. The larger the circle, the better fit the model provides to the data for a given geographical region characterized by the 1-D reference model. Light filled circles correspond to models with a passive phase change, dark open circles represent models where the high-pressure phase is 1% denser than the low-pressure phase. The value of the penalty function varies from 0.13 for the "best" model to 0.87 for the "worst" model.

points. The mean residuals and their standard deviations are plotted in Figure 5.10a as a function of the separation of the reflection points for a model with a passive phase and $\gamma_{ph} = 6$ MPa/K and $h_{ph} = 150$ km. A straightforward comparison with the analogous plots presented by *Lay et al.* [1997] for the raypaths sampling northern Siberia, Alaska is plagued by the 2-D nature of our models. Indeed, any observed low wavelength trends in the spatial correlation function cannot be expected to be reproduced by our models, as a small separation between the ScS reflection points implies a closeness of the raypaths in 2-D geometry, while in a 3-D case the velocity structure sampled by the two paths off the vertical plane defined by the reflection points, can be quite different. So the low power in the short wavelength part of the correlation functions in Figure 5.10 is not surprising. Another important difference between our results for the computed models and the data analysis of *Lay et al.* [1997] is a much higher value of the standard deviation of the travel time residuals suggested by our models. However, with all the limitations of our models, the analysis of the spatial correlations reveals several important trends, such as the peak at 15°-20° observed for ScS-S, ScS-Scd and Scd-S residuals. This peak is relatively sharp for ScS-S and Scd-S residuals and is somewhat broader for the ScS-Scd residuals. Analysis of the slab structure in Figure 5.3a suggests that this characteristic scale of heterogeneity may reflect the folding pattern of the horizontally lying slab where the separation between adjacent folds approximately corresponds to the location of the maxima in the autocorrelation functions (Figure 5.10a).

Another interesting observation that can be made from Figure 5.10a is the relatively flat autocorrelation function for ScS-Scd residuals. This agrees with the results of the spatial correlation study of the travel time residuals performed by *Lay et al.* [1997] and has been interpreted as indicative of a significant heterogeneity at short scales. The relatively small amplitudes of ScS-Scd autocorrelation function are in accord with the results presented in Figure 5.8, where the ScS-Scd differential travel time residuals display less scatter than the ScS-S and Scd-S residuals. This is again in good agreement with the observations [*Lay et al.*, 1997] and implies that most of the heterogeneity in the D" is concentrated just above the discontinuity or in a thin
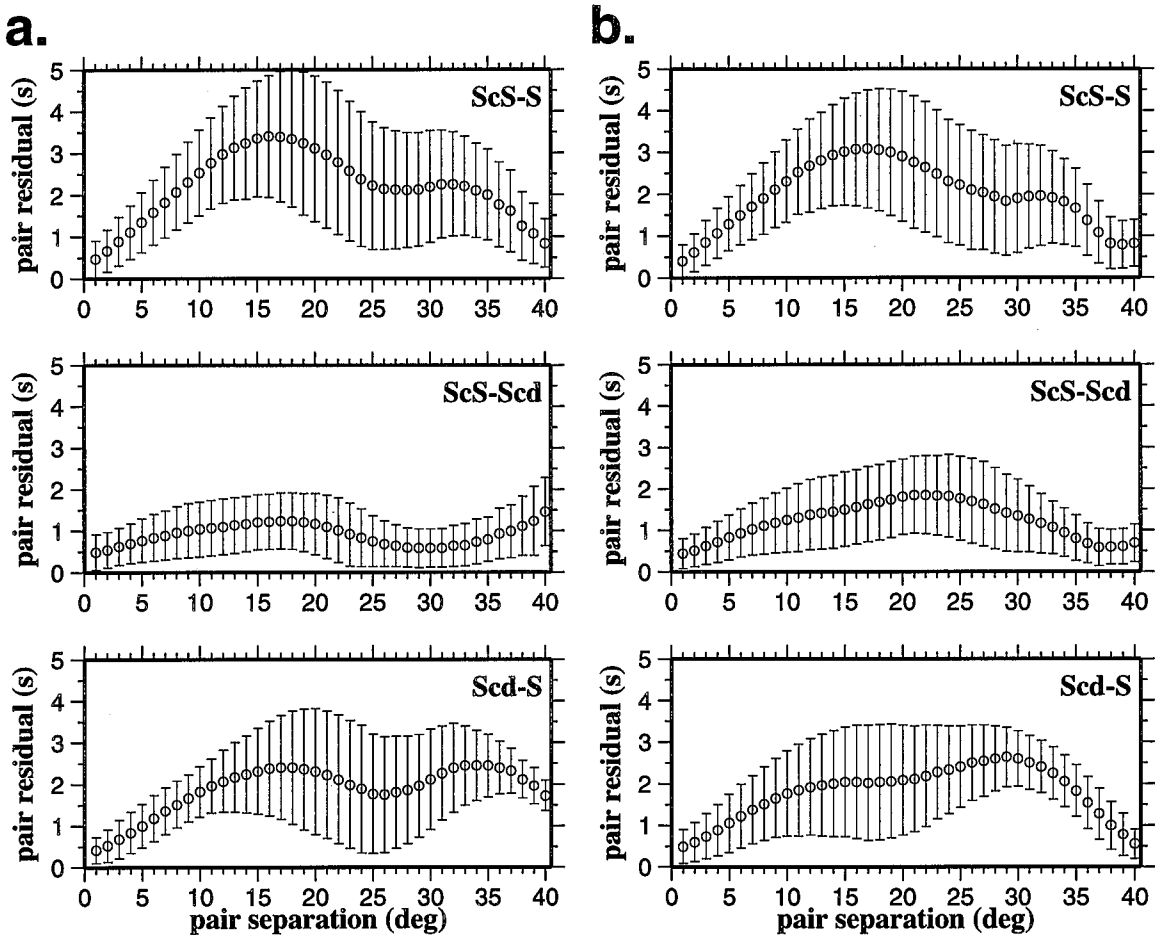
Figure 5.10: Spatial correlation of the differential travel times residuals for two computed models. The travel times were obtained from seven different constant offset sections corresponding to distances $\triangle$ from 75° to 83° and residuals were computed with respect to the reference model SGLE. The circles represent the mean absolute values of residuals for all pairs of raypaths with a given separation between the ScS reflection points and $50° \leq \phi_{refl} \leq 90°$. The standard error is indicated by the vertical bars. **a** – correlations for a model with a passive phase and $\gamma_{ph} = 6$ MPa/K, $h_{ph} = 150$ km; **b** – for a model with a passive phase with a phase boundary having constant height above the CMB ($\gamma_{ph} = 0$ MPa/K, $h_{ph} = 223$ km) equal to the average height of the phase boundary for the model used in a, computed in the region $50° \leq \phi_{refl} \leq 90°$.

layer just below it – in a region that is sampled by both ScS and Scd raypaths.

The spatial correlation analysis also allows us to decouple the effects of the discontinuity topography variations from the volumetric heterogeneity. This can be done by repeating the correlation analysis for a model with a flat phase boundary with the elevation above the CMB equal to the average elevation of the phase boundary in the model with $\gamma_{\mathrm{ph}} = 6$ MPa/K and $h_{\mathrm{ph}} = 150$ km. The autocorrelation functions for such a model, characterized by $\gamma_{\mathrm{ph}} = 0$ MPa/K and $h_{\mathrm{ph}} = 223$ km, are presented in Figure 5.10b. Comparison of Figure 5.10b with Figure 5.10a reveals some minor differences in the ScS-S and Scd-S autocorrelations with more pronounced changes in the trends of the ScS-Scd spatial correlation. This comparison suggests that the volumetric anomalies have the dominant effect on the computed ScS-S and Scd-S travel times. Even for the ScS-Scd autocorrelation function the change caused by including topography variations into the seismic velocity field is within the standard error of the travel time residuals and thus cannot be considered statistically meaningful.

5.5 Discussion

Most purely seismological models explaining the D" triplication use a value of 2-3% for the amplitude of the shear velocity jump. Based on the dynamic implications for the structures at the base of the mantle, *Sidorin et al.* [1998] suggested that the triplication is conditioned by both the discontinuous velocity increase and the velocity gradient just above the discontinuity and demonstrated that a model with just a 1% velocity jump overlaid by a higher than PREM gradient can explain the triplication observations under Western Caribbean at least as well as models with a 3% discontinuity. The double structure in this class of models naturally emerges from the thermal and possibly chemical complexity of the region that gives rise to large variations in the velocity gradients, and can explain the intermittent nature of the D" triplication. Although the discontinuity may be a ubiquitous feature, Scd arrivals of sufficient amplitude will only be observed in the regions where the discontinuity is overlaid by a significantly high velocity gradient. Such regions with high positive radial gradients

of the shear velocity are expected, for example, in the areas of subduction, where the best observations of the Scd phase have been made.

While a phase change is a plausible mechanism for the velocity discontinuity, other possibilities exist. A simple global chemical layer at the bottom of the mantle is an unlikely candidate as a quite complex change in chemistry may be required to both dynamically stabilize the layer and make it seismically faster than the overlying mantle [*Sidorin and Gurnis*, 1998]. In addition, the geographical pattern of predicted Scd arrivals does not agree with the seismological observations. However, the chemical contrast caused by oceanic crust within subducted slabs may provide the required velocity jump and can be a viable alternative to the global phase change.

A phase change mechanism has previously been hypothesized as the cause of the D" discontinuity (see review by *Wysession et al.* [1998]). However, despite remarkable advances in the experimental mineral physics little is known about the phase diagrams of the lower mantle minerals. Even for the major constituents (silicate perovskite and magnesiowüstite) the questions of stability under D" conditions remain a subject of debate. The suggestion of instability of silicates at high pressures dates back to [*Birch*, 1952] and was more recently supported by *Stixrude and Bukowinski* [1990] and *Meade et al.* [1995], who demonstrated that silicate perovskite dissociates into SiO_2 and $(Mg,Fe)O$ under the conditions pertinent to the D" region. However, other studies, including theoretical calculations [*Stixrude and Cohen*, 1993] as well as experimental work [*Knittle and Jeanloz*, 1987; *Tsuchida and Yagi*, 1989; *Serghiou et al.*, 1998] argue against such a decomposition and suggest that $(Mg,Fe)SiO_3$-perovskite is stable under the lower mantle conditions. The existence of any phase transition under D" condition for magnesiowüstite, the other major element in the composition of the lower mantle, is also uncertain. Although FeO experiences at least one phase change in the range of pressures and temperatures corresponding to the lower mantle [*Jeanloz and Ahrens*, 1980], no evidence for a phase change has been observed for $Mg_{0.6}Fe_{0.4}O$ under shock compression up to 200 GPa [*Vassiliou and Ahrens*, 1982]. The uncertainty in the experiments conducted under simultaneous high pressure and temperature conditions is such that it does not currently allow one to categorically rule out a phase transition

in either silicate perovskite or magnesiowüstite under D" conditions. This is especially true because the results of this study and the study by *Sidorin et al.* [1998] suggest that a minor change in the elastic properties will suffice to explain the D" seismic triplication.

Another possible explanation for the discontinuous increase in the shear velocity atop D" is a phase transition in some of the minor constituents of the lower mantle. A consideration of the cosmic abundances suggests substantial amounts of CaO and Al_2O_3 in the lower mantle. This is probably especially true for the base of the mantle, where a higher concentration of refractory elements is expected [*Ruff and Anderson*, 1980]. Phase transitions have been discovered in both CaO and Al_2O_3 [*Jeanloz and Ahrens*, 1980; *Funamori and Jeanloz*, 1997]. The transformation of corundum (α-Al_2O_3) to the Rh_2O_3 (II) structure occurs under conditions comparable to those expected at the top of D", while the B1$\rightarrow$B2 transition in CaO has been observed at mid-mantle pressures ($\approx$ 70 GPa). However, the abundances of free CaO or Al_2O_3 at the base of the mantle are unknown. Moreover, not only is the elements partitioning between various phases under the D" conditions unknown, the relative concentrations of the elements are highly uncertain as well and depend on the model of Earth differentiation and history of the mantle evolution. It seems impossible, however, to rule out a phase transformation in one of the Al or Ca-bearing phases that would lead to a 1% increase in the shear velocity of the minerals assemblage.

A phase transition in stishovite or one of the post-rutile phases of SiO_2 [*Tsuchida and Yagi*, 1989; *Dubrovinsky et al.*, 1997] is a yet another candidate for the discontinuous velocity increase atop D". It has been suggested [*Knittle and Jeanloz*, 1991; *Kellogg and King*, 1993] that the chemical reactions between the core and mantle material may increase the concentration of free silica at the base of the mantle and thus a notable phase transition in silica may in principal produce a sufficient increase in the shear velocity of the mineral assemblage.

Our study cannot provide any constraint on the density change associated with the phase transformation that is a potential cause of the D" discontinuity. As we have demonstrated, the computed waveforms are to a large degree controlled by the

slab structure which is only slightly sensitive to the small (0-1%) density change in the phase transformation. A significantly higher density change would probably have a more important effect on the slab dynamics, but is unlikely. The structure of the major lower mantle constituents (Mg,Fe perovskite and magnesiowüstite) is already very closely packed and any large volume change associated with further structural modifications is hardly possible. In addition, these two minerals have been a subject of a great number of high pressure experiments and it is unlikely that a major phase transformation with a large volume change may have been overlooked. If the phase transformation is to occur in some of the minor elements of the mineral assemblage, it may require a very large density change in order to increase the average density by much more than 1%.

The constraints provided by the seismologically observed differential travel times and their variations allowed us to estimate the Clapeyron slope (6 MPa/K) and pressure (127 GPa) of the phase change that may give rise to the D" triplication. Our dynamic models that incorporated a phase change with these parameters provided a favorable fit to the data corresponding to northern Siberia and Alaska. The poor fit to the data in Central America and India is frustrating but understandable. The D" structure under Central America is especially complex (e.g., [*Kendall and Nangini*, 1996]) and can hardly be characterized by a single 1-D model (SLHA). The data coverage in India is very sparse [*Lay et al.*, 1997] so that the reference model (SYL1) may also be a poor representation of the "average" structure and the actual observations.

Our study suggests that at least for a 1% velocity contrast associated with the phase transformation most of the travel time variations are due to the volumetric anomalies. The largest of these anomalies are produced by the buckling and folding of the slab lying on the core-mantle boundary. This "topography" of the thermal signature of the slab is responsible for the topography of the phase boundary and, together, they determine the variations in the differential arrival times. This explains why the variations in ScS-Scd residuals are relatively small: both Scd and ScS sample the same largely heterogeneous region at the top of D".

A study by *Griffiths and Turner* [1988] demonstrated that the characteristic wave-

length of slab folding is primarily controlled by the rheology of the slab and the kinematics of subduction. If our interpretation of the maxima in the autocorrelation functions (Figure 5.10) is correct and the peak at 15°-20° indeed corresponds to the characteristic wavelength of the slab buckling, it is possible that the maxima in the autocorrelation function for the seismic data [*Lay et al.*, 1997] reflect the same physical processes. This information can then be used to constrain the rheology of the slab in the deep mantle, creating yet another loop of mutual constraints between geodynamics, mineral physics and seismology.

5.6 Conclusions

Using dynamical models with a phase change near the bottom of the mantle we obtained constraints on the characteristics of the phase change (P,T conditions and Clapeyron slope) that produce seismic structures and waveforms consistent with seismological observations. We found that dynamic models which provide the best fit to the seismic observations have a Clapeyron slope of the basal phase transition of about 6 MPa/K and the elevation of the phase boundary above the CMB of about 150 km under adiabatic temperatures. Dynamic models indicate that a phase boundary characterized by a negative Clapeyron slope is generally smoother than a phase boundary with a positive Clapeyron slope of the same absolute value. This reduced topography of phase boundaries with a negative Clapeyron slope produces variations in seismic differential travel times which are too small and inconsistent with observations. Likewise, phase changes with a too small ($<<$ 6 MPa/K) or too large ($>>$ 6 MPa/K) positive Clapeyron slope lead to too small or excessively large variations of differential travel times.

We found that the D" discontinuity modeled by the phase change in our computations produces the strongest triplication in the area of subduction and weak or absent Scd arrivals away from the slab. This pattern is consistent with the general geographical pattern of the D" triplication observations, where the strongest Scd arrivals have been reported in subduction areas. The dynamics of the slab appears to

be important in giving rise to the triplication, as the thermal structure of the slab produces volumetric seismic velocity anomalies and modifies the topography of the discontinuity. These anomalies and the phase boundary topography explain most of the variations in the differential travel times. The patterns in these variations, such as relatively small amplitude of ScS-Scd variations, are consistent with the results obtained by *Lay et al.* [1997] for the data in various regions and indicate that the largest heterogeneity is located at the very top of the D" layer or just above it. The characteristic peaks in the spatial autocorrelation functions of seismic differential travel time residuals may be representative of the characteristic wavelengths of folding of subducted slabs. If so, the analysis of spatial correlations of the seismic travel time anomalies may provide important constraints on the rheology of the slab at the base of the mantle.

Our analysis failed to provide any constraints on the density change associated with the phase transition that may be responsible for the D" discontinuity. Although the density change, together with Clapeyron slope, has a significant influence on the dynamics of plumes emerging from the CMB, its impact on the dynamics of subducting slabs is minor, which can be partly due to slab kinematics enforced in our models. Fully dynamic models of subduction with a more realistic rheology would be required to further investigate the general influence of this parameter. Plate kinematics, effects of internal heating, rheology – all these and other factors to some extent control the dynamics of the system and thus the seismic velocity field at any point in its evolution. However, the analysis of these parameters is out of the scope of this study and is left for future investigation.

Although a phase change appears to be a viable mechanism for the D" seismic discontinuity, other possibilities, such as the chemical contrast associated with the subducted oceanic crust in slabs, cannot be ruled out and deserve further study.

Chapter 6 Geographical Patterns of D"
Triplication Inferred From Tomography
Models

6.1 Abstract

The relative strength of the D" triplication has large regional variations due to the heterogeneity at the base of the mantle. We argue that the triplication is conditioned by both the larger-scale seismic structure, imaged by body-wave seismic tomography and an abrupt velocity increase (D" discontinuity) which cannot be resolved by tomographic techniques. Higher resolution waveform analysis suggests strong variations in differential travel times and amplitudes of the associated phases. In Chapter 5 we show that a phase change mechanism for the velocity jump can in general explain the geographical patterns in the triplication strength. Assuming such a mechanism for the velocity jump, we predict the elevation of the discontinuity above the core-mantle boundary at any given location using thermal anomalies inferred from tomographic inversions. The discontinuity is imposed on the large scale structure predicted by tomographic models with an appropriate compensation for the velocity increase. Using this composite seismic structure, we compute 2-D synthetic waveforms for a variety of 2-D sections with available seismological observations. The regions that are considered include Alaska, Northern Eurasia, India, Central America and Central Pacific. By comparing the variations in the computed differential travel times with observations, we select characteristics of the phase transition that are most compatible with seismological data. A phase transition that provides best agreement with data is characterized by a shear velocity jump of 1.5%, ambient elevation above the core-mantle boundary of about 200 km and a positive Clapeyron slope of about 6 MPa/K. A mo-

del with such a phase transition imposed on the global shear wave velocity structure provides a satisfactory match to the seismologically observed patterns of differential travel times for Alaska, Eurasia, India and Central America. It also explains the apparent intermittance of the D" discontinuity by predicting very weak triplication beneath Central Pacific and north-eastern Caribbean where there is little evidence for a D" triplication.

6.2   Introduction

An apparent velocity jump at the top of the D" layer at the base of the mantle gives rise to a seismic triplication. The main evidence for the triplication comes from the observed additional phase (Scd) arriving between direct S and the core reflection ScS at an approximate distance range of 65°-83°. The relative timing and amplitudes of the three phases (S, Scd and ScS) experience significant variations (discussed in Chapter 5) on many different scale lengths. Systematics of global variations have been captured by various 1-D reference models produced for various regions around the world with an evidence for the triplication (Figure 1.1). Consistently strong Scd arrivals are produced by the structures beneath Northern Eurasia, Alaska, India and Central America, while the structure in Central Pacific shows a very weak signal reflected off the D" discontinuity. The observed variations in Scd-S and ScS-Scd differential travel times have previously been used (e.g., [*Gaherty and Lay*, 1992; *Kendall and Shearer*, 1994; *Lay and Helmberger*, 1983; *Young and Lay*, 1987, 1990]) to infer the elevation of the D" discontinuity above the CMB in various regions and it has been suggested that up to 300 km topography of the discontinuity is possible.

The cause of these large variations in the depth of the discontinuity is unknown and depends on the physical mechanism producing the seismic velocity jump. In addition to being able to explain the inferred topography of the discontinuity, a plausible physical model must explain the observed intermittency of the seismic triplication. In Chapter 4 we considered several possibilities (thermal gradients, chemical interfaces or a solid-solid phase transition) and concluded that a phase change model pro-

vides the best correlation with the observed strength patterns of the D" triplication. In Chapter 5 we demonstrated that seismic velocity fields computed from dynamic models incorporating a phase change at the base of the mantle can provide sufficient variations in both predicted differential travel times and relative amplitudes to be compatible with observations. We also showed that the strength of the triplication is conditioned by both the amplitude of the velocity jump and the local vertical and lateral velocity gradients produced by the large-scale seismic structure. However, the dynamic models used were generic in nature and did not correspond to any particular region in the world. While producing 3-D spherical models compatible with plate tectonics reconstructions and using realistic rheology appears more plausible every day, such realistic models are not available just yet.

The large-scale structure of the mantle has been extensively imaged recently using seismic tomography techniques and this offers the ability to make predictions of the geographic variations in D" structure. The resolution of this imaging is still poor, but the fact that most tomography models agree with each other on a larger scale is encouraging. These models carry considerable information about the local velocity gradients in the mantle (although some degree of smoothing is unavoidable in tomographic inversions). None of the currently existing inversions incorporates Scd phases and so no information about the D" discontinuity is contained in the tomography models. Any travel time anomaly arising from such a discontinuity is attributed to a volumetric velocity anomaly at the base of the mantle. This ambiguity in the interpretation of the observed travel time anomalies is caused by the poor ray coverage in some regions and limited resolution of the tomographic inversion. It leads to non-uniqueness in tomographic inversions as they have limited resolution and are unable to distinguish between two different seismic velocity structures that produce similar travel time anomalies. So one can "refine" the tomography models by adding a discontinuity at a certain level and compensating its influence on travel times by adjusting the local volumetric anomaly. However, one needs some physical model that would predict the depth of the discontinuity at any given location. Based on the conclusions of Chapter 4, we choose a phase transition as a cause of the velocity

jump and use the thermal anomalies inferred from seismic tomography to predict its depth variations.

Seismic velocity anomalies imaged by tomography are likely results of thermal heterogeneities. However, the observed disagreement between S and P velocity models may suggest some degree of chemical heterogeneity at the base of the mantle [*van der Hilst and Kárason*, 1999; *Wysession et al.*, 1999]. Fortunately, in most regions S and P velocities vary in phase, which may imply thermal origin of velocity perturbations so that the local thermal anomaly can be inferred from the observed seismic velocity anomaly. This technique, although prone to some error due to neglecting of chemical heterogeneity and poor constraints on thermoelastic properties, has been widely used to estimate the thermal structure of the mantle [*Jordan et al.*, 1993; *Mégnin et al.*, 1997; *Morgan and Shearer*, 1993; *Ricard et al.*, 1989]. We use this approach to add a discontinuity to the velocity field obtained by tomographic inversions. Using this composite seismic structure we compute synthetic waveforms for a variety of 2-D cross-sections. The question we address in this study is whether such a synthetic velocity model including a first order discontinuity combined with the seismically imaged large scale structure can predict some of the observed patterns in differential travel times and relative amplitudes of the D" triplication.

Important constraints on the structure of the D" are provided by the differential travel times T_{Scd-S} and $T_{ScS-Scd}$. The average values of these differentials can be indicative of the dominant depth of the D" discontinuity while their variations within a region can characterize the topography of the discontinuity. However, significant tradeoffs exist between the depth of the discontinuity, its amplitude and the local velocity structure. Such tradeoffs cannot be resolved by 1-D modeling and, in fact, it has long been speculated (e.g., [*Lay et al.*, 1997]) that the observed variations in T_{Scd-S} and $T_{ScS-Scd}$ can possibly be due to the local volumetric anomalies rather than be caused by the topography of the discontinuity. Placing a discontinuity in context of the velocity structure produced by tomography may provide a tool for testing this hypothesis and resolve the ambiguity in the interpretation of the travel time variations.

6.3 Incorporating a first order discontinuity in tomography models

We use Grand's [*Grand et al.*, 1997] shear velocity tomography model and impose a 1.5% discontinuity at the base of the mantle. The discontinuity is modeled by a phase transition which, as in Chapter 5, is characterized by an ambient (corresponding to adiabatic temperatures or, in seismic velocity space, to PREM values) elevation above the CMB, h_{ph}, and Clapeyron slope, γ_{ph}. The Clapeyron slope controls how the local elevation of the phase transition varies as local temperatures deviate from the adiabat (or seismic velocities deviate from PREM).

The tomography model is parameterized by blocks with lateral dimensions of $2° \times 2°$. The blocks comprise spherical layers whose thickness (radial resolution) varies between 75 and 250 km; the poorest resolution (250 km) is at the bottom of the mantle. The seismic anomaly is prescribed to the blocks as a perturbation with respect to PREM. For a continuous model, we smear the anomalies by assigning them to the centers of the blocks and using tri-linear interpolation in-between. The interpolated velocity structure is mapped onto a fine resolution ($0.2° \times 0.2° \times 2$ km) mesh to ensure that the topography of the predicted discontinuity is adequately well resolved. Each vertical column of this fine mesh is then pertubed, as illustrated in Figure 6.1, by imposing the discontinuity and introducing an appropriate compensation. For any vertical cross-section and at any depth h, the local velocity value is computed using

$$V(h) = V_{\mathrm{PREM}}(h) \left(1 + \triangle V(h) \right) , \qquad (6.1)$$

where $V_{\mathrm{PREM}}(h)$ is the PREM value at depth h and $\triangle V(h)$ is the local interpolated velocity perturbation. Similar to (5.4) we add a discontinuity to (6.1) using

$$V'(h) = V(h) \left\{ 1 + \frac{1}{2} \frac{\beta}{100} \left[1 + \tanh \left(\frac{1}{w_{\mathrm{ph}}} r_{\mathrm{ph}} \right) \right] \right\} , \qquad (6.2)$$

where β is the amplitude of the velocity jump in % (1.5%), w_{ph} (5 km) is the width

of the phase transition, and r_{ph} is given by

$$r_{\mathrm{ph}}(h) = h - h_{\mathrm{ph}} - \frac{\gamma_{\mathrm{ph}}}{\rho(h)g}\triangle T(h)\,. \qquad (6.3)$$

In equation (6.3) g is the gravity acceleration in the mantle, $\rho(h)$ is density at depth h (Figure 2.1) and $\triangle T(h)$ is the non-adiabatic temperature perturbation estimated using (2.21), that can be rewritten as

$$\triangle T(h) = -2\frac{\triangle V(h)}{\alpha(h)V_{\mathrm{PREM}}(h)(\Gamma - 1)}\,, \qquad (6.4)$$

where $\alpha(h)$ is the depth dependent coefficient of thermal expansion (Figure 2.4) and Γ characterizes temperature dependence of the shear modulus in the mantle (Chapter 2, page 8). We use $\Gamma = 6$.

The addition of the velocity discontinuity affects the predicted travel times. In order to make our composite model consistent with the original tomography model, we apply a negative velocity gradient at the base of the mantle. Such a gradient is qualitatively consistent with the predictions of dynamic models where it is produced by a thermal boundary layer above the CMB. A constant value is used for the velocity at the CMB and the gradient is computed to provide the appropriate compensation for the increase in the slowness integral,

$$I = \int_{surface}^{CMB} \frac{dh}{V(h)}\,, \qquad (6.5)$$

over the entire vertical profile caused by the inserted discontinuity. When the discontinuity is too close to the CMB and an appropriate compensation cannot be made the negative gradient zone starts immediately below the imposed discontinuity. The value of seismic velocity at the CMB is then varied to achieve the appropriate travel time compensation.

The limited resolution of tomography inversions dampens the recovered signal and tends to reduce the amplitude of inferred anomalies in mantle structure. Unfortunately, the degree of this reduction cannot be easily estimated. A study of the

low-velocity structure at the base of the central Pacific [*Breger et al.*, 1998] suggests that tomographic models underestimate the anomalies there by about a factor of 3. While this may be the case in some regions, it is unlikely to be true globally, as it would imply extended areas in the deep mantle with slower than -10% and faster than $+10\%$ anomalies. While the former can be attributed to areas with partial melt or iron enrichment, the latter cannot be easily reconciled with the possible composition models of the lower mantle (see discussion in Chapter 2) as anomalies of such magnitude are obviously of non-thermal origin. To explore the effects of possible smearing of the structure by tomographic inversions on the predicted travel times, we introduce parameter ϵ – a factor by which we globally scale the tomographic perturbations (so that a $x\%$ anomaly becomes a $\epsilon x\%$ anomaly).
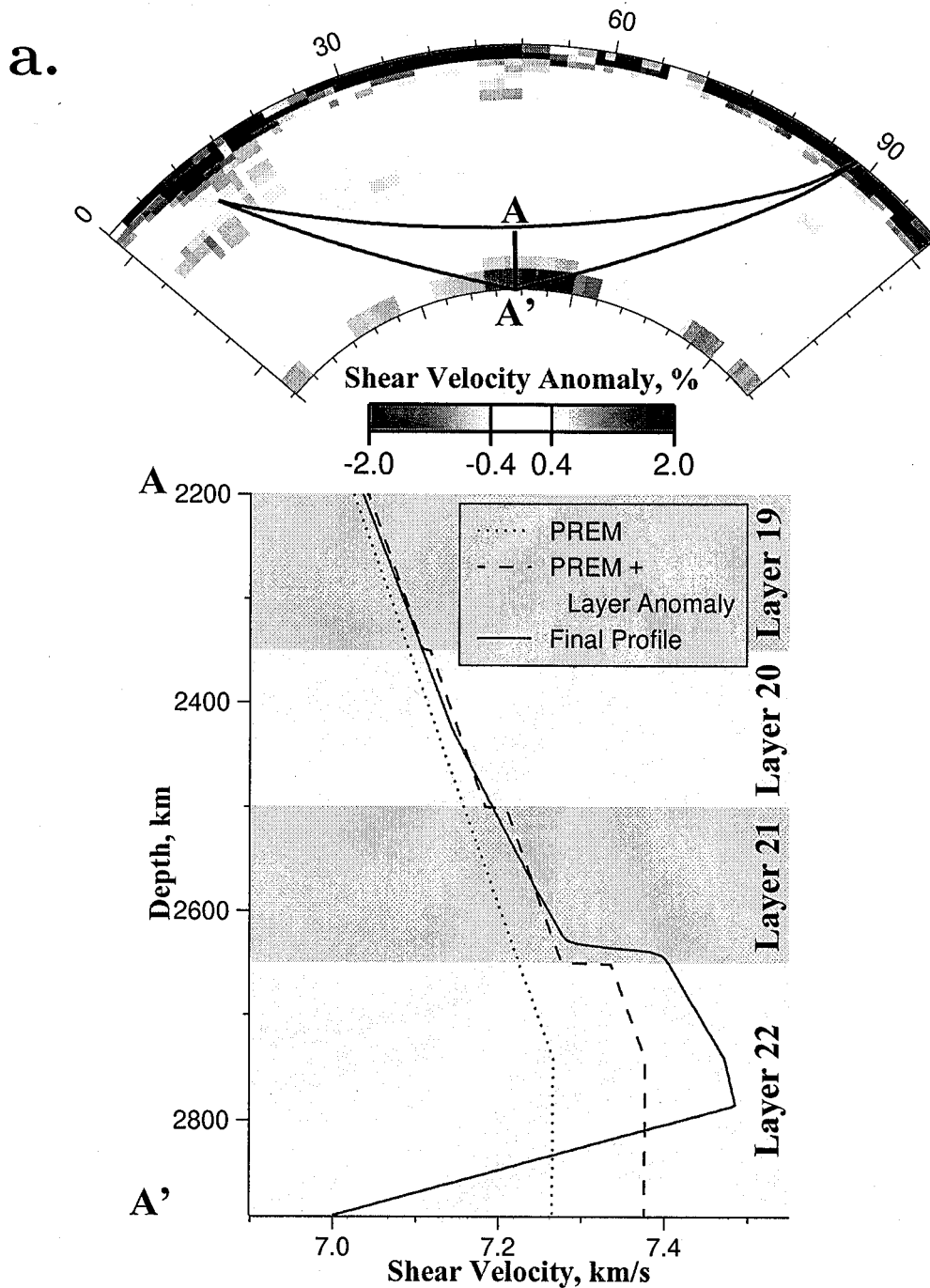
Figure 6.1: Velocity cross-section through Grand's tomography model along two paths across Central America. The direct S phase and core reflection (ScS) are shown. The bottom panel illustrates the perturbation of a vertical velocity cross-section (using ScS bounce point location as example) used to incorporate a discontinuity and the appropriate compensation. The shade indicates the four lowermost layers in the tomography model parameterization. The epicentral distance is about the same (77°) in both cases.

a: cross-section along the path from event 940808 to station Mt. Saint Helens (SHW); Scd samples D" beneath Western Caribbean – a region with strong evidence for a D" triplication;
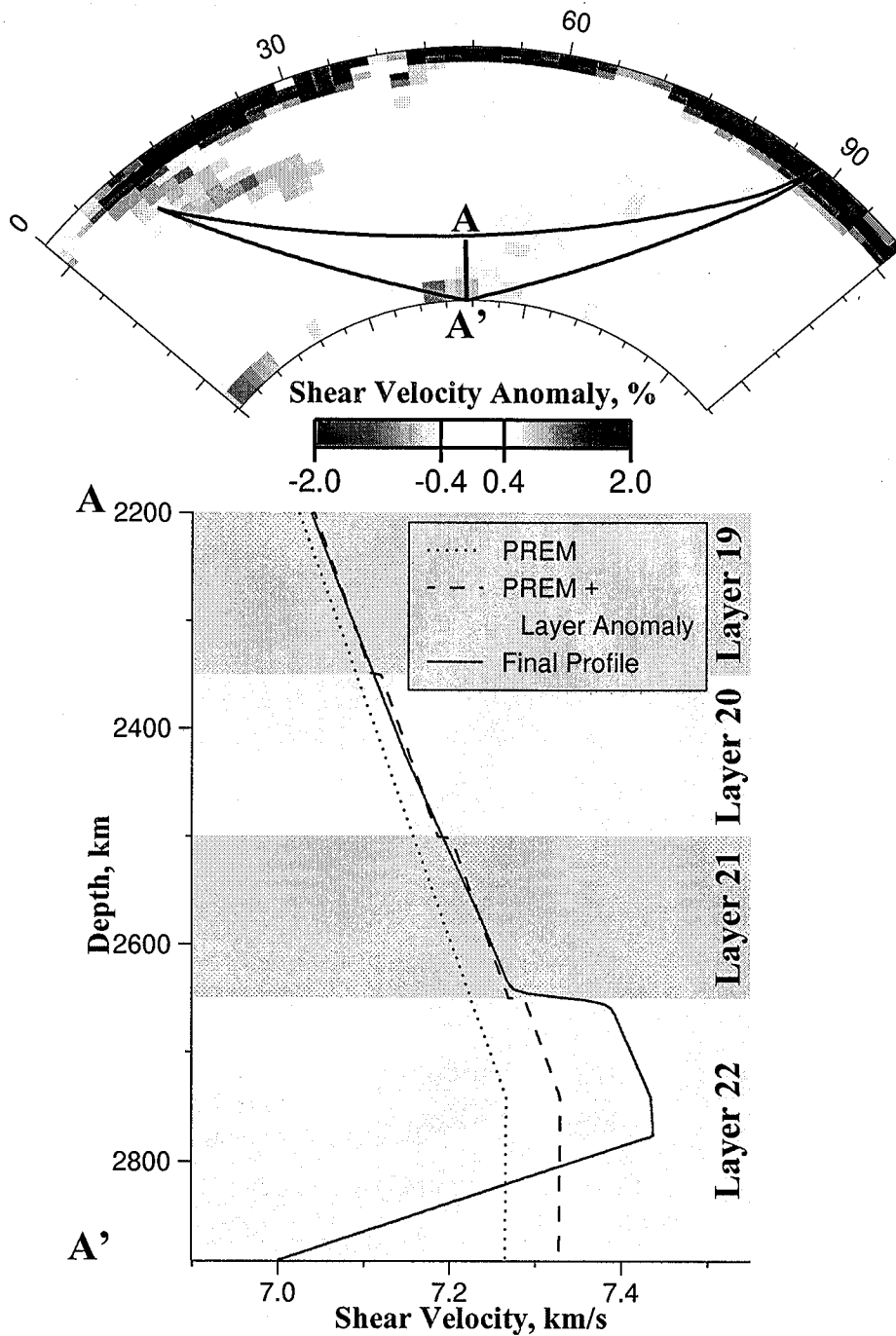
Figure 6.1 (*continued*): **b:** cross-section along the path from event 940110 to station Frobisher Bay (FRB); Scd samples D" beneath Eastern Caribbean – a region lacking D" triplication observations.

6.4 Differential travel times analysis

To explore how well the composite model described above predicts the observed travel time patterns, we compute 2-D synthetics for a variety of ray paths sampling D" in five different regions. Four of these regions (Alaska, Northern Eurasia, India and Central America) exhibit strong evidence for the D" discontinuity (marked Scd arrivals). The evidence for the discontinuity in the fifth region (Central Pacific) is slim and special processing of the data is required to separate the Scd signal from the noise. The events that are used to compute the synthetics are listed in Table 6.1. For Alaska, Eurasia and India we use only those ray paths that were studied by *Young and Lay* [1990], *Gaherty and Lay* [1992], and *Young and Lay* [1987], respectively. There is no single comprehensive database for the D" triplication beneath Central America and Central Pacific. In addition, the D" structure beneath Central America appears to be more variable than in other regions, which is reflected in the numerous 1-D reference models proposed for the region [*Lay and Helmberger*, 1983; *Kendall and Nangini*, 1996; *Ding and Helmberger*, 1997; *Sidorin et al.*, 1998]. To address this variation, we compute synthetics for ray paths from three South American events (Table 6.1) to all possible World-Wide Standard Seismograph Network (WWSSN) and Canadian National Seismograph Network (CNSN) stations in North America in the 68°-85° distance range. For the D" structure beneath the Central Pacific, all ray paths from three Fiji-Tonga events (Table 6.1) to North American stations in the same distance range are used. The source-receiver configuration as well as surface projections of ScS bounce points are shown in Figure 6.2.

We use the same technique [*Ni et al.*, 1999] as in Chapter 5 to compute 2-D synthetic waveforms for all the paths. A cross-section is made through the high resolution velocity mesh along each ray path and a combination of WKM and GRT methods is used to compute the synthetics. We vary the characteristics (h_{ph} and γ_{ph}) of the imposed phase change, analyze the predicted differential travel times for the agreement with observations and search for the best combination of parameters h_{ph} and γ_{ph}. All synthetics are computed for a source depth of 600 km and the observed

Table 6.1: Seismic events used in the study

Event	Latitude, deg	Longitude, deg	Depth, km	Event region
640318	52.56	153.67	424	Sea of Okhotsk
640804	46.57	151.36	86	Kuriles
650921	28.96	128.23	195	Ryukyu
670704	43.10	142.58	157	Kuriles
670813	35.43	135.49	367	Sea of Japan
671012	52.15	152.57	466	Sea of Okhotsk
671201	49.45	154.40	144	Kuriles
680228	32.95	137.85	348	Izu-Bonin
680514	29.93	129.39	162	Ryukyu
690331	38.49	134.52	397	Sea of Japan
690413	6.10	129.90	152	Java
690815	21.57	143.10	320	Izu-Bonin
700813	8.90	118.00	117	Java
700905	52.28	151.49	560	Sea of Okhotsk
710129	51.69	150.97	515	Sea of Okhotsk
720306	50.14	148.80	569	Sea of Okhotsk
720527	54.97	156.33	397	Sea of Okhotsk
720821	49.47	147.08	573	Sea of Okhotsk
721104	8.20	112.30	126	Java
730131	28.22	139.30	508	Izu-Bonin
730728	50.45	148.92	585	Sea of Okhotsk
730910	42.48	131.05	552	Sea of Japan
740222	33.17	136.98	391	Izu-Bonin
740311	48.31	153.16	154	Kuriles
740517	6.50	106.80	126	Java
740921	52.19	157.44	119	Kuriles
751221	51.93	151.57	546	Sea of Okhotsk
751228	8.00	115.10	196	Java
760710	47.31	145.75	402	Sea of Okhotsk
761212	28.04	139.67	503	Izu-Bonin
770101	7.90	109.00	80	Java
770513	28.42	139.59	448	Izu-Bonin
780315	26.45	140.76	278	Izu-Bonin
780523	31.07	130.10	160	Ryukyu
780621	48.27	148.06	380	Sea of Okhotsk
780902	24.81	121.87	115	Taiwan
790507	6.30	106.00	106	Java
790816	41.85	130.86	566	Sea of Japan
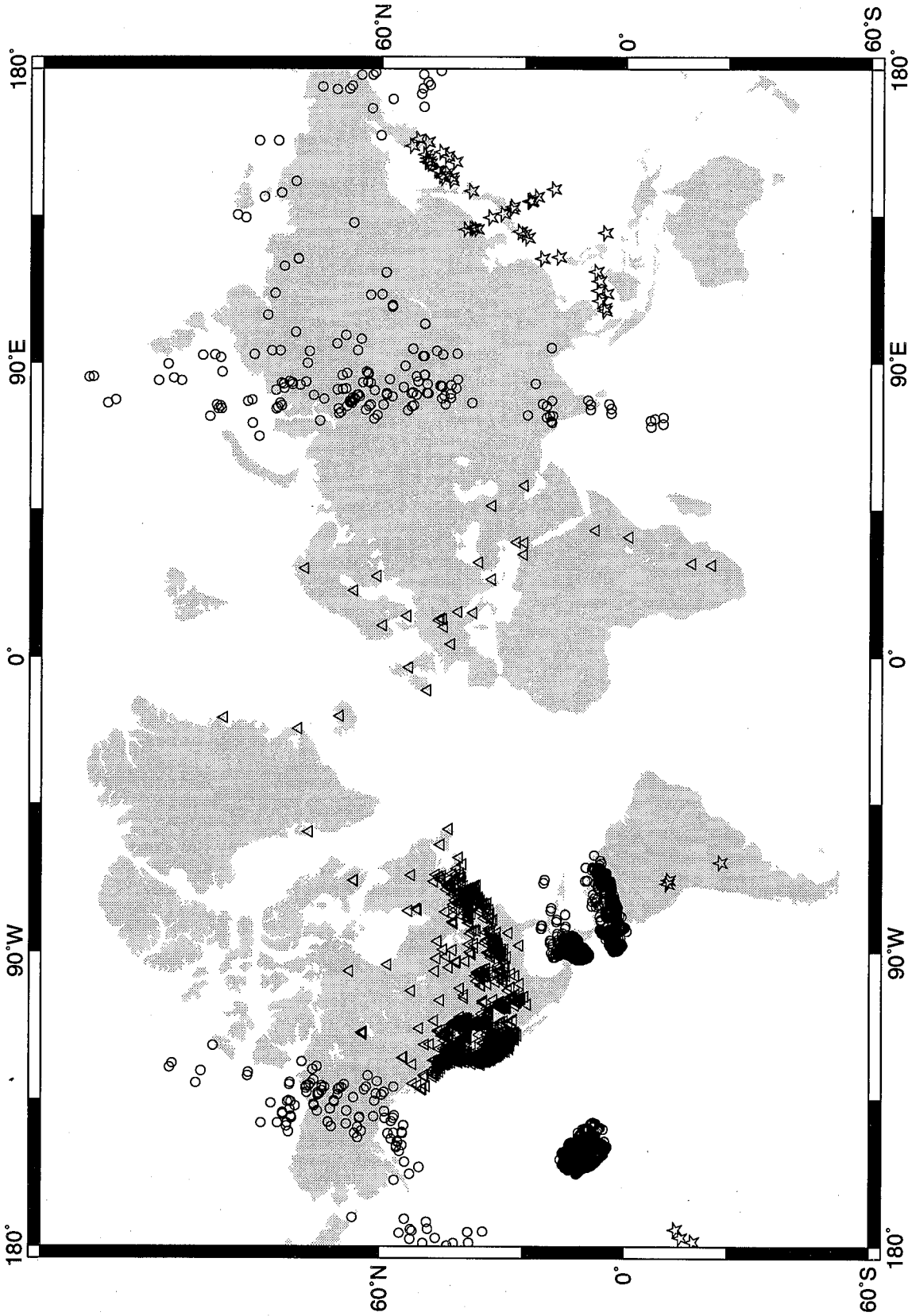
Figure 6.2: Events (stars) and stations (triangles) used in the study. Circles show the surface projections of ScS bounce points for the paths that are considered.

Table 6.1 (continued)

Event	Latitude, deg	Longitude, deg	Depth, km	Event region
800331	35.49	135.52	362	Sea of Japan
811007	-20.75	-178.63	620	Fiji-Tonga
811127	42.93	131.19	525	Sea of Japan
830703	20.19	122.41	221	Philippine Islands
830724	53.91	158.36	190	Kamchatka
831008	44.21	130.74	551	Sea of Japan
840201	49.05	146.63	580	Sea of Okhotsk
840420	50.12	148.75	582	Sea of Okhotsk
840423	47.44	146.73	398	Izu-Bonin
840425	-17.31	-177.23	415	Fiji-Tonga
840615	-15.82	-174.83	247	Fiji-Tonga
840709	5.80	111.30	534	Java
940110	-13.31	-69.39	589	South America
940510	-28.50	-62.90	599	South America
940808	-13.60	-68.20	600	South America

travel times are corrected for the same depth.

We first consider the ray paths that sample D" beneath Alaska and Eurasia as these two regions have the most comprehensive and robust data sets. We start by imposing a flat discontinuity ($\gamma_{ph} = 0$) at 250 km above CMB onto Grand's tomography model ($\epsilon = 1$). Due to a large size of the dataset (more than 130 source-receiver pairs in each of the two regions) and significant scatter, direct comparison of the predicted and observed travel times is not particularly descriptive. Instead, we choose a two-step approach, where we first obtain a least-squares fit to the computed differential travel times and then test if the fitting curves provide a satisfactory fit to the data. The first step is illustrated in Figure 6.3 where T_{Scd-S} differential travel times computed for one of the models (characterized by $\gamma_{ph} = 6$ MPa/K and $h_{ph} = 200$ km) are plotted as a function of epicentral distance and the best fitting curves are indicated. Figure 6.4a presents the observed T_{Scd-S} differential travel times as well as the best-fitting curves computed for a model with a flat discontinuity at 250 km above CMB.
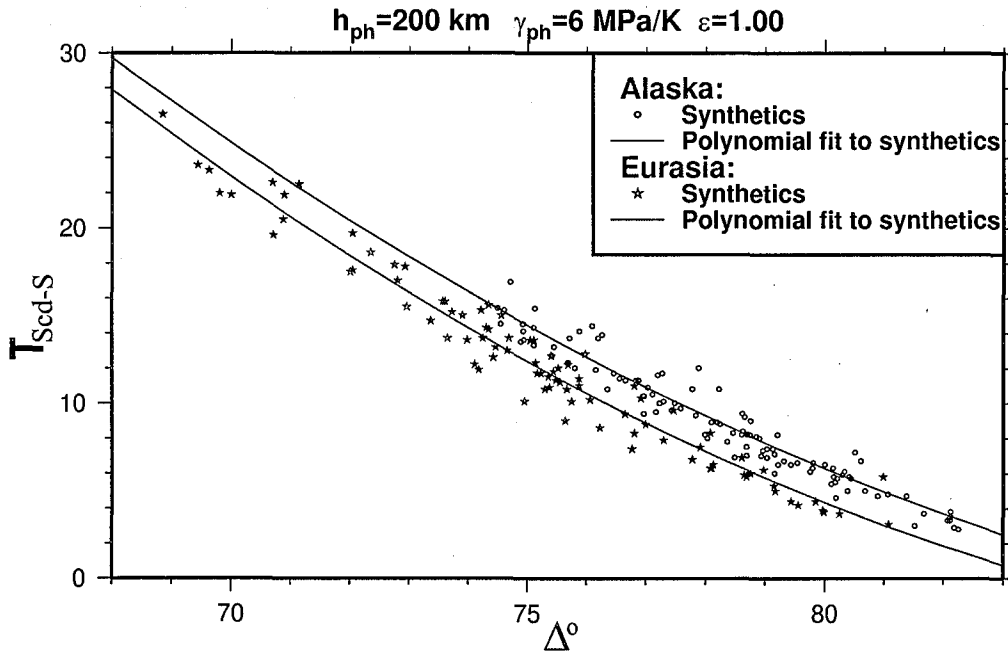
Figure 6.3: Scd-S differential travel times for Alaska and Eurasia computed for a model characterized by $h_{ph} = 200$ km, $\gamma_{ph} = 6$ MPa/K, $\epsilon = 1.0$. The curves provide a polynomial least squares fit.

It is more convenient for the analysis to present the data using a running mean. The comparison of the data for the two regions reveals a systematic difference of ~ 2 s in T_{Scd-S} differential travel times. However, the curves representing the synthetics computed for the respective regions are quite close to each other and obviously do not provide a satisfactory fit.

In order to test if anomalies larger than inferred by the tomography inversion [*Grand et al.*, 1997] can be responsible for the observed patterns in differential travel times variations, we use a factor of $\epsilon = 1.5\%$ to globally scale the tomographically inferred perturbations. In Figure 6.4b T_{Scd-S} differential travel times computed for such model with an incorporated flat phase transition at 250 km above CMB are compared with the data. The curves representing the synthetics for the two regions are better separated than in Figure 6.4a, but the fit to the data is still unsatisfactory. While further separation may be achieved by additional magnification of the anomalies, as we noted in section 6.3, extreme fast anomalies cannot be easily justified.

Figure 6.4c presents a comparison of T_{Scd-S} predictions from a model with a
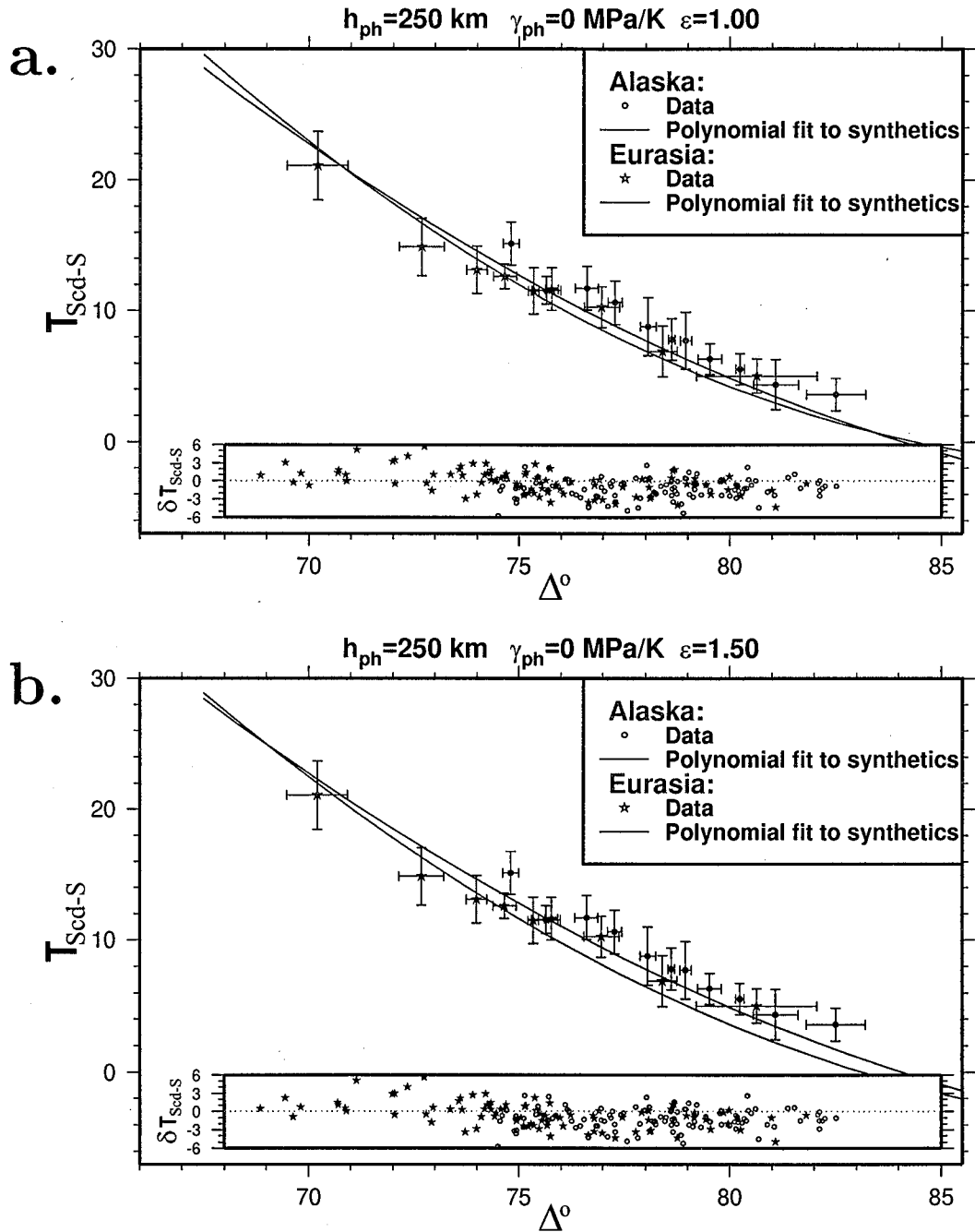
Figure 6.4: Observed Scd-S differential travel times for Alaska and Eurasia (for the convenience of analysis, a running mean is computed in groups of 10; the error bars indicate the standard error) and a polynomial fit to the synthetic differential travel times computed for the corresponding raypaths. The inset shows the misfit between the observed Scd-S differential travel times and Scd-S times obtained from synthetics. **a** – synthetics computed for a model characterized by $h_{ph} = 250$ km, $\gamma_{ph} = 0$, $\epsilon = 1$; **b** – synthetics computed for a model characterized by $h_{ph} = 250$ km, $\gamma_{ph} = 0$, $\epsilon = 1.5$;
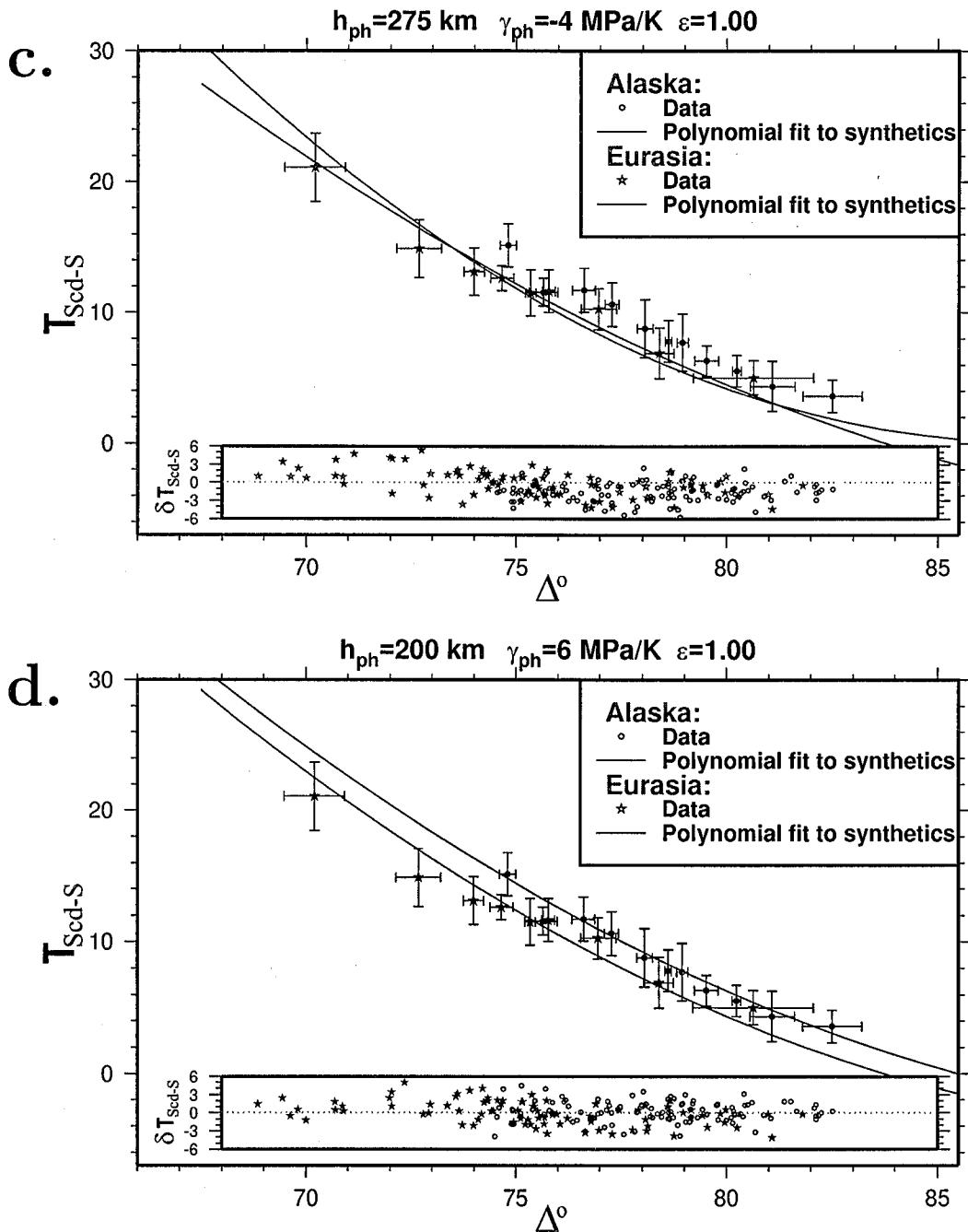
Figure 6.4 (*continued*): **c** – synthetics computed for a model characterized by $h_{ph} = 275$ km, $\gamma_{ph} = -4$ MPa/K, $\epsilon = 1$; **d** – synthetics computed for a model characterized by $h_{ph} = 200$ km, $\gamma_{ph} = 6$ MPa/K, $\epsilon = 1$.
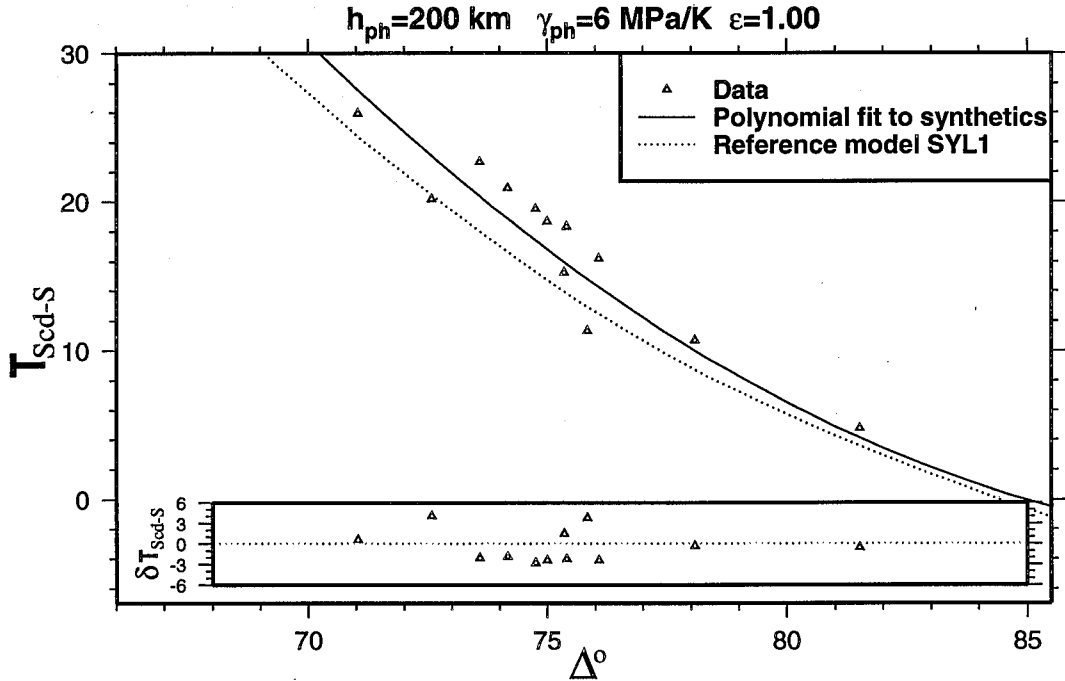
Figure 6.5: Observed Scd-S differential travel times for India and a polynomial fit to the synthetic differential travel times computed for the corresponding raypaths. The inset shows the misfit between the observed Scd-S differential travel times and Scd-S times obtained from synthetics. The synthetics are computed for a model characterized by $h_{ph} = 200$ km, $\gamma_{ph} = 6$ MPa/K, $\epsilon = 1$.

phase change characterized by a negative Clapeyron slope $\gamma_{ph} = -4$ MPa/K and $h_{ph} = 275$ km. Although the average depth of the discontinuity is about the same as in models shown in Figure 6.4a,b the computed T_{Scd-S} differential travel times are in worse agreement with the data. In contrast, a phase transition with a positive value of Clapeyron slope, $\gamma_{ph} = 6$ MPa/K, and $h_{ph} = 200$ km provides a good fit to the data for both Alaska and Eurasia (Figure 6.4d). Moreover, using the same values for the modelled structure beneath India, successfully reproduces the T_{Scd-S} differential travel times observed in that region (Figure 6.5). It is interesting to note that the agreement between the computed and observed travel times for India is noticeably better than between the data and predictions of model SYL1 [*Young and Lay*, 1987].

The insets in Figure 6.4 show the residual between the T_{Scd-S} differential travel times predicted by a particular model and observed differential travel times for the same path. These residuals characterize the quality of fit to the data for each model

and may be used as a metric in which various models are compared. We compute an r.m.s. misfit between the model predictions and the data using

$$\langle \delta T_{\text{Scd-S}} \rangle = \left[\frac{1}{N} \sum_{1}^{N} \left(T_{\text{Scd-S}}^{\text{synth}} - T_{\text{Scd-S}}^{\text{data}} \right)^2 \right]^{\frac{1}{2}}, \tag{6.6}$$

where N is the number of source-receiver pairs in a given region. Figure 6.6 presents the misfit (6.6) for a variety of models characterized by different values of γ_{ph} and h_{ph}. As it suggests, the best fit for the data sampling Alaska and Eurasia is obtained for models where the phase transition is characterized by a Clapeyron slope of $\sim$ 6 MPa/K and $h_{\text{ph}} \sim 200$ km. Models with these parameters also produce a rather good fit to the observations for India though the smallest value of $\langle \delta T_{\text{Scd-S}} \rangle$ is obtained for $\gamma_{\text{ph}} = -8$ MPa/K and $h_{\text{ph}} = 250$ km. However, the data coverage in India is sparse and the fit is poorly constrained.

In Figure 6.7 we present the overall misfit computed by carrying out the summation in (6.6) over all the source-receiver pairs in all three regions. Accordingly, the phase transition most consistent with seismic observations for Alaska, Eurasia and India is characterized by γ_{ph} of about 6 MPa/K and h_{ph} of about 200 km. We will further use the model with a phase change characterized by these values and refer to it as the "preferred model."

Our comparison of the computed models with the data is based on the $T_{\text{Scd-S}}$ differential travel times. The difference between ScS and Scd arrival times, $T_{\text{ScS-Scd}}$, also carries important information on the morphology of the discontinuity as well as the structure of the D" region. However, our estimates of $T_{\text{ScS-Scd}}$ are more poorly constrained than $T_{\text{Scd-S}}$ for several reasons. The D" layer appears to have a larger degree of heterogeneity than the rest of the mantle. Unfortunately, the basal region also has the least resolution in Grand's tomography model and the thickness of the lowermost layer in the model is as large as 250 km. In addition, our modification of the tomography model, while conserving the travel time in vertical columns, effects the timing of ScS phases, especially at large distances, where a substantial path is travelled within the the imposed negative gradient zone at the base of the mantle. An
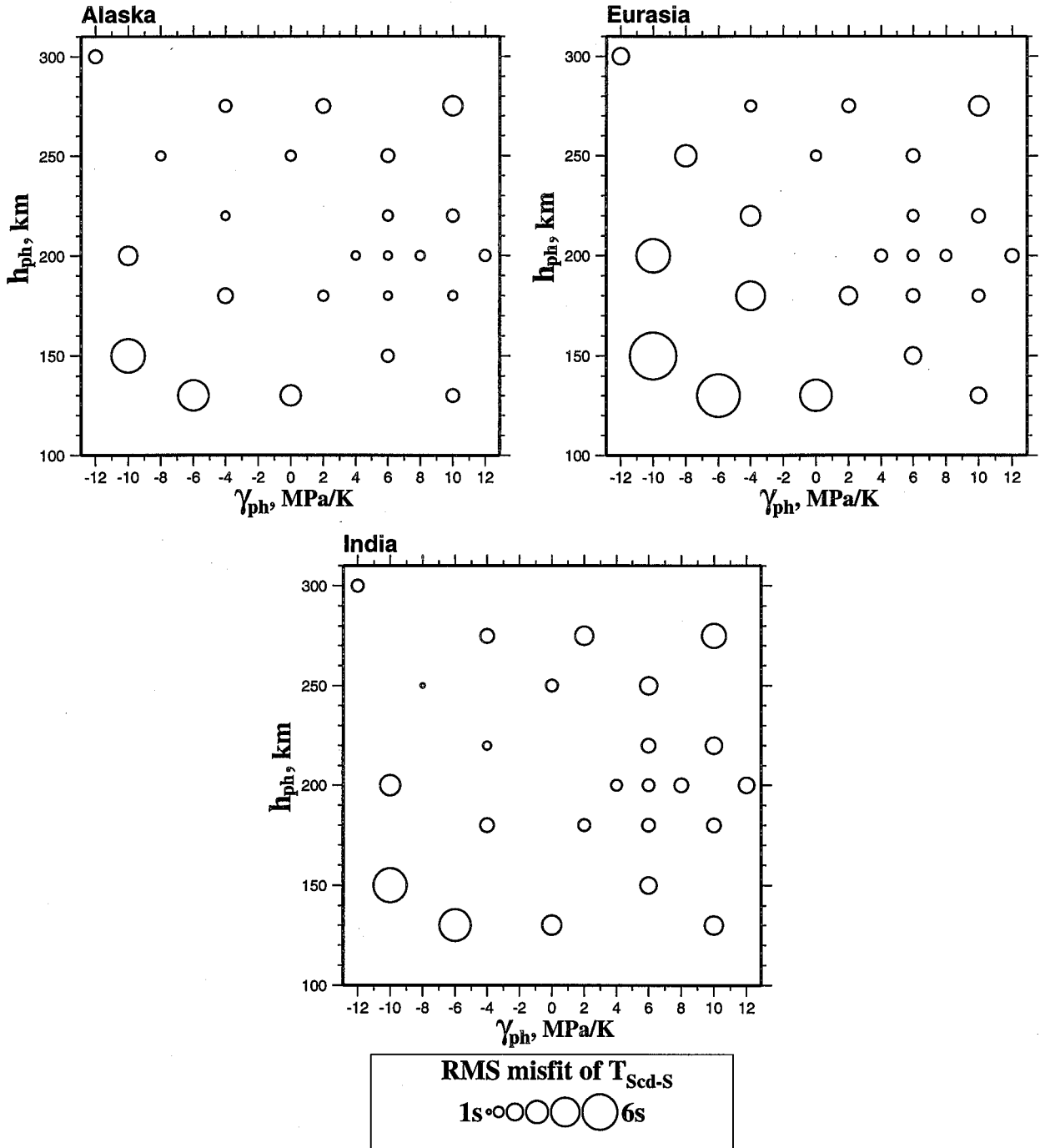
Figure 6.6: $T_{\text{Scd}-\text{S}}$ differential travel time misfit between data in three regions (left – Alaska, middle – Eurasia, right – India) and predictions of models with various phase change characteristics (Clapeyron slope, γ_{ph}, and ambient elevation, h_{ph}).
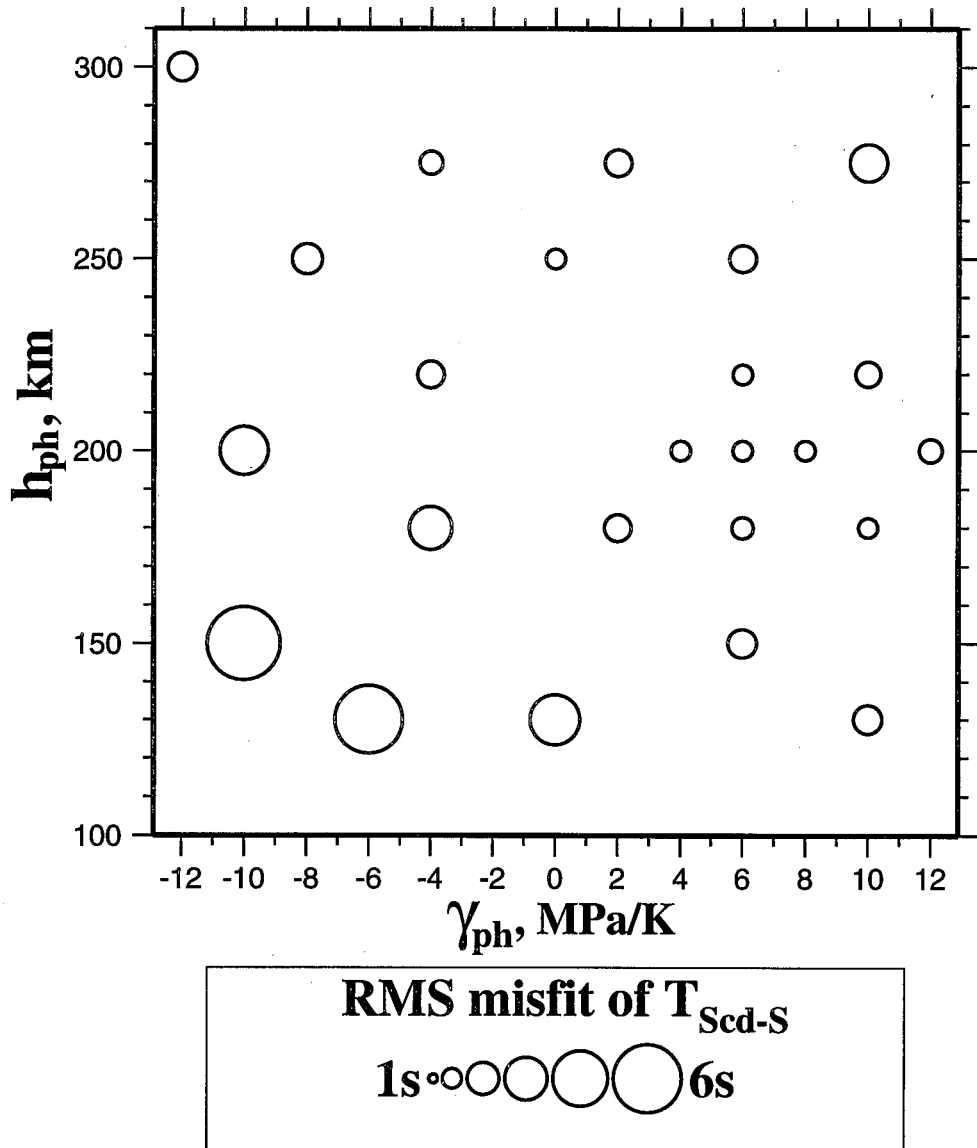
Figure 6.7: Overall T_{Scd-S} differential travel time misfit between data for Alaska, Eurasia and India, and predictions of models with various phase change characteristics (Clapeyron slope, γ_{ph}, and ambient elevation, h_{ph}).
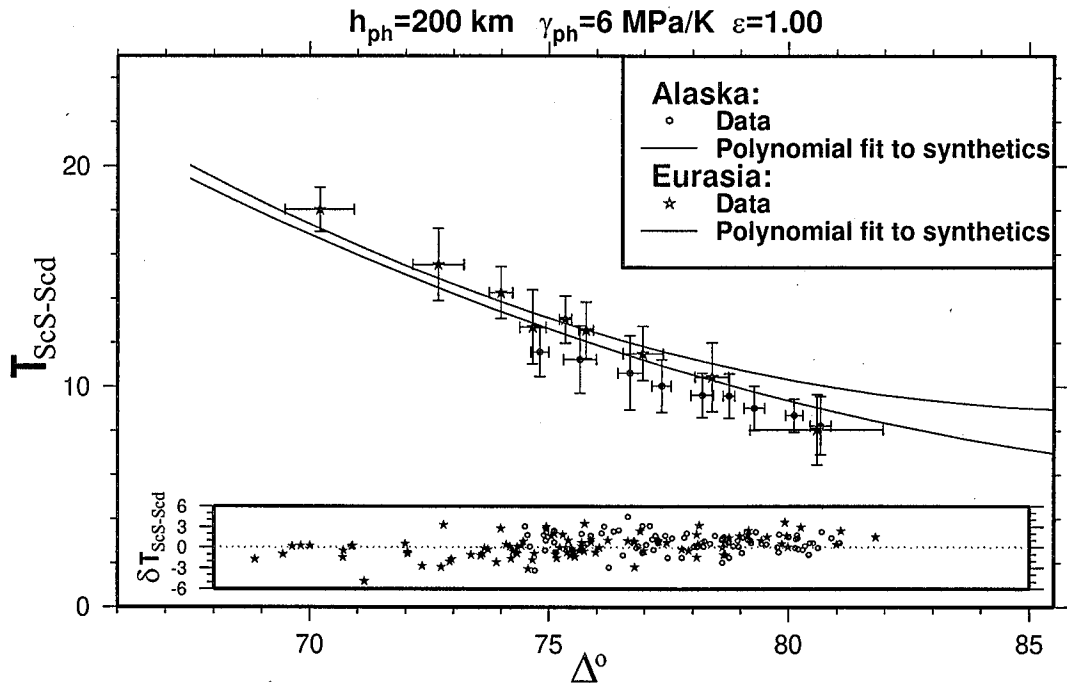
Figure 6.8: Observed ScS-Scd differential travel times for Alaska and Eurasia (for the convenience of analysis, a running mean is computed in groups of 10; the error bars indicate the standard error) and a polynomial fit to the synthetic differential travel times computed for the corresponding raypaths. The inset shows the misfit between the observed ScS-Scd differential travel times and ScS-Scd times obtained from synthetics. Synthetics are computed for a model characterized by $h_{ph} = 200$ km, $\gamma_{ph} = 6$ MPa/K, $\epsilon = 1$.

example of $T_{ScS-Scd}$ predictions for our preferred (based on T_{Scd-S}) model is given in Figure 6.8. The fit to the respective data sets is not as good as for T_{Scd-S} differential travel times, with increasing discrepancy at larger distances.

The elevation of the D" discontinuity above the CMB suggested by the 1-D reference models is 243 km beneath Alaska, 290 km beneath Eurasia and 280 km beneath India. It is interesting to explore how these seismologically inferred elevations compare to the predictions of our preferred model providing the best fit to T_{Scd-S} differential travel times. As Figure 6.5 suggests and as was discussed by Lay et al. [1997] model SYL1 does not provide satisfactory travel time predictions for the corresponding data. The distribution of the phase transition elevations by the Scd bounce points is given in Figure 6.9. According to the figure, about 40% of the considered ray paths beneath Alaska sample the discontinuity at about 225 km at the Scd bounce points with the

total range of the elevation variation from 180 to 250 km. For Eurasia, the peak of the distribution is at roughly 235 km. The topography of the discontinuity sampled by Scd bounce points is more significant with the elevation ranging from 160 to 300 km. The average elevation of the discontinuity is 222 km for Alaska and 235 km for Eurasia. These values are substantially lower than the ones inferred by 1-D seismological models although our preferred model provides at least as good fit to the data, if not better, as the 1-D reference models. This illustrates the non-uniqueness of the models and questions the legitimacy of the discussions of the D" discontinuity topography inferred from 1-D studies (e.g., [*Kendall and Shearer*, 1994; *Schimmel and Paulssen*, 1996]).

Not only do the 1-D studies fail to provide unequivocal constraints on the average elevation of the D" discontinuity, the very concept of the "average elevation" must be used with some caution. To illustrate this we computed the area distribution of the computed discontinuity elevations for the regions outlined in Figure 1.1. This is done by breaking down the regions into cells of equal area and computing the elevation of the discontinuity in each cell. The distribution of the obtained elevations is shown in Figure 6.9 (dashed line). For Alaska, this distribution is similar to the distribution of elevations computed at the Scd bounce points meaning that the data samples the discontinuity topography in the region fairly well. For Eurasia, however, the distributions are significantly different. The distribution computed for the equal-area cells is relatively flat and lacks the sharp peak observed in the distribution obtained for the locations of Scd bounce points. This means that the data excessively samples some small area, with few ray paths passing through other parts of the region. Fortuitously in this particular case the well sampled area happens to have a D" discontinuity at a depth close to the average depth in the region (the mean values of the two distributions agree to within 5 km). However, this analysis demonstrates that a non-uniform data coverage can bias the value of the inferred depth of the discontinuity and produce misleading results.

The surface projections of ScS bounce points for the paths sampling the structure beneath Central America are given in Figure 6.10. The D" triplication is well
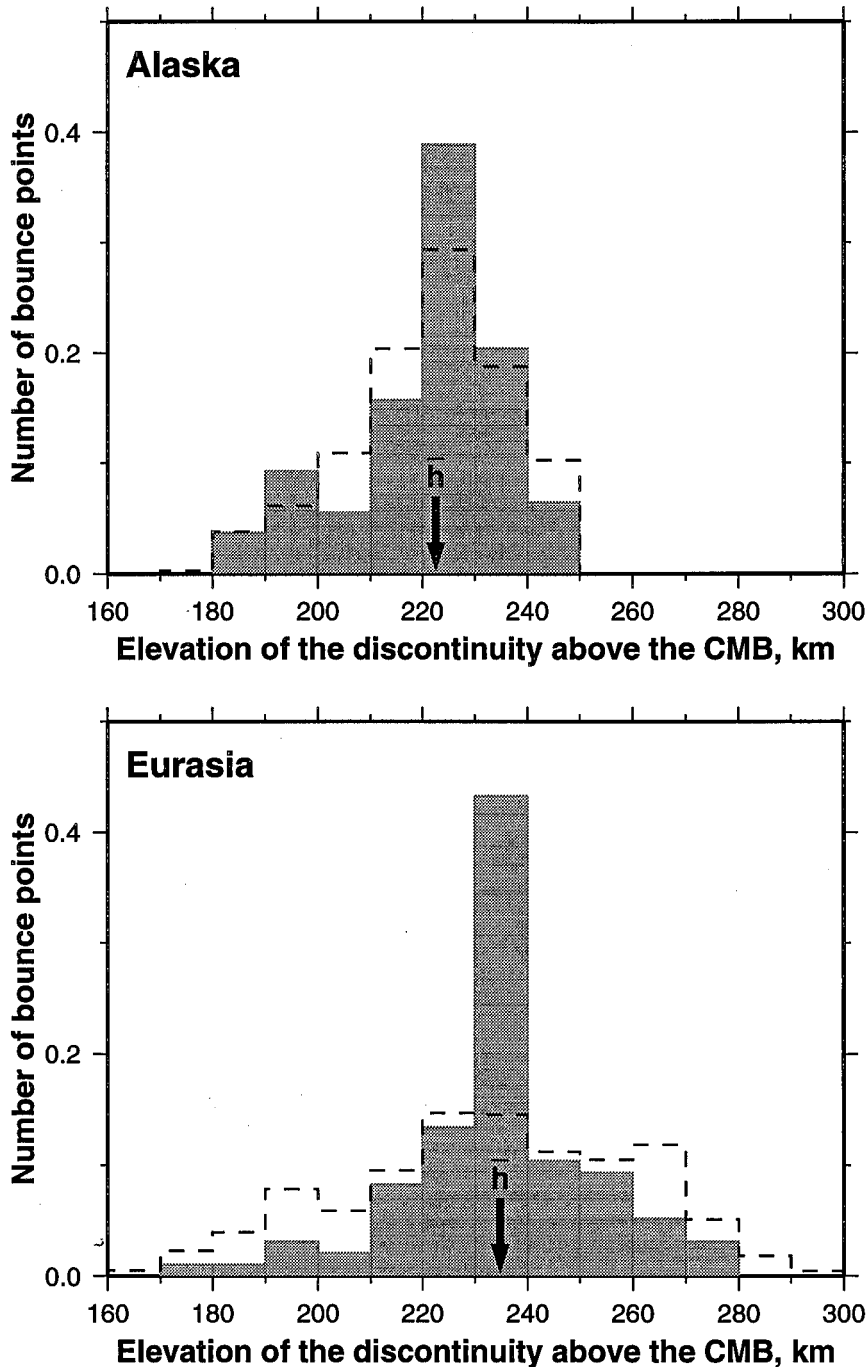
Figure 6.9: Histogram of computed phase change elevations above the CMB at Scd bounce points for Alaska (top) and Eurasia (bottom). The phase transition is charcaterized by $\gamma_{ph} = 6$ MPa/K and $h_{ph} = 200$ km. The mean values are indicated by arrows. The dashed line shows the distribution of the phase change elevations computed in equal-area cells covering the corresponding regions outlined in Figure 1.1.

pronounced in many parts of the region [*Ding and Helmberger*, 1997; *Kendall and Nangini*, 1996; *Lay and Helmberger*, 1983]. However, the triplication has not been detected in the limited data [*Kendall and Nangini*, 1996] sampling the north-eastern part of the region (bounce points indicated by squares in Figure 6.10). According to the study of *Kendall and Nangini* [1996] the inferred structure in the northern Caribbean (dark shaded region in Figure 6.10) is notably different from the structure in the southern Caribbean (light shaded region in Figure 6.10). This difference is reflected by the two separate 1-D reference models, SKNA1 (Southern Caribbean) and SKNA2 (Northern Caribbean), advanced to approximate the observed travel times in the respective region. Although these models are more poorly constrained than the models for Alaska or Eurasia, they may provide some indication of the travel time trends in the two regions.

Using our preferred model we compute $T_{\mathrm{Scd-S}}$ differential travel times separately for the two regions outlined in Figure 6.10. The results are plotted together with the predictions of 1-D reference models in Figure 6.11. Our modeling also suggests an offset in the differential travel times for the two regions and the predictions are quite similar to the values captured by the 1-D reference models for the respective regions.

The evidence for a D" triplication in the Central Pacific [*Garnero et al.*, 1993; *Kendall and Shearer*, 1994; *Russel and Lay*, 1998] is not convincing and in most cases only stacking data allows the detection of an intermediate arrival between S and ScS phases. This suggests that even if a D" triplication is present in the Central Pacific, it is significantly weaker than, for example, in Eurasia or Alaska. No consistent Scd arrival is observed in the synthetics that we compute for the preferred model (Figure 6.14).

6.5 Relative amplitudes analysis

In Chapters 4 and 5 we demonstrated that variations in the local structure accompanying a ubiquitous discontinuity may modulate the apparent strength of the D" triplication leading to considerable variations in relative Scd amplitudes. It is thus
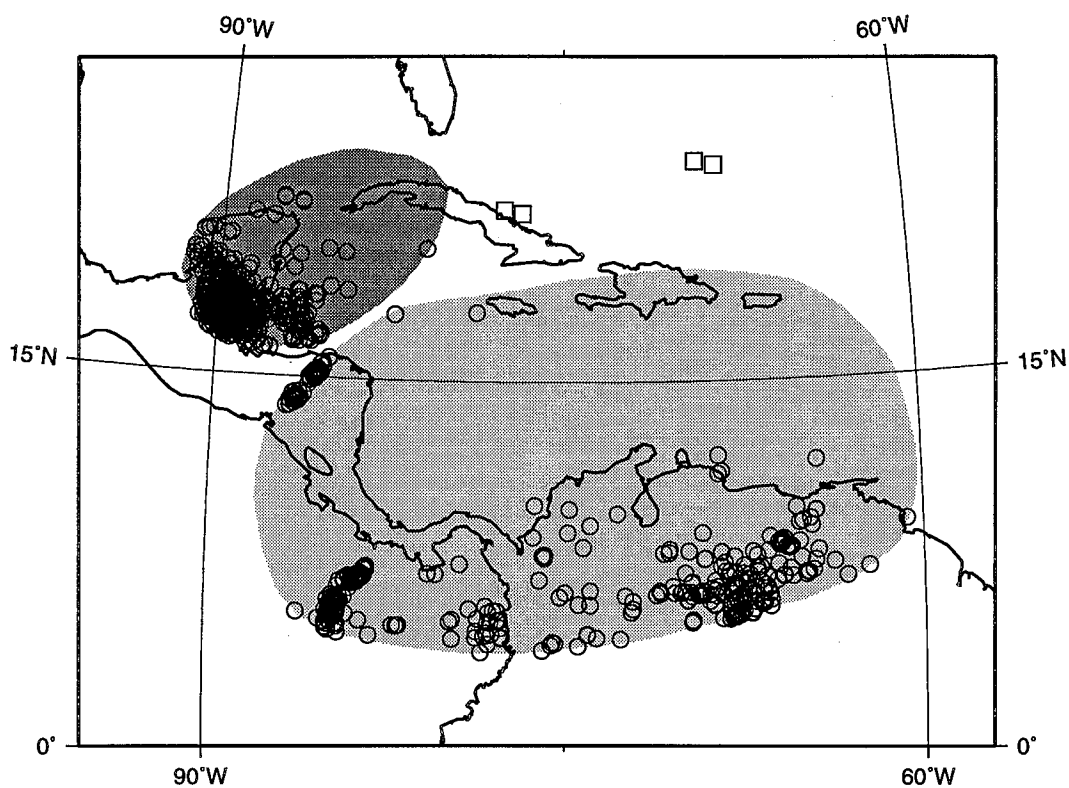
Figure 6.10: D" triplication observations beneath Central America. Circles represent surface projections of ScS bounce points; squares indicate surface projections of ScS bounce points for paths that do not have evidence for a D" triplication. The light shaded region represents the area where the observed travel times can be approximated by 1-D reference model SKNA1 [*Kendall and Nangini*, 1996]; the dark shaded region represents the area where the observed travel times can be approximated by model SKNA2 [*Kendall and Nangini*, 1996].
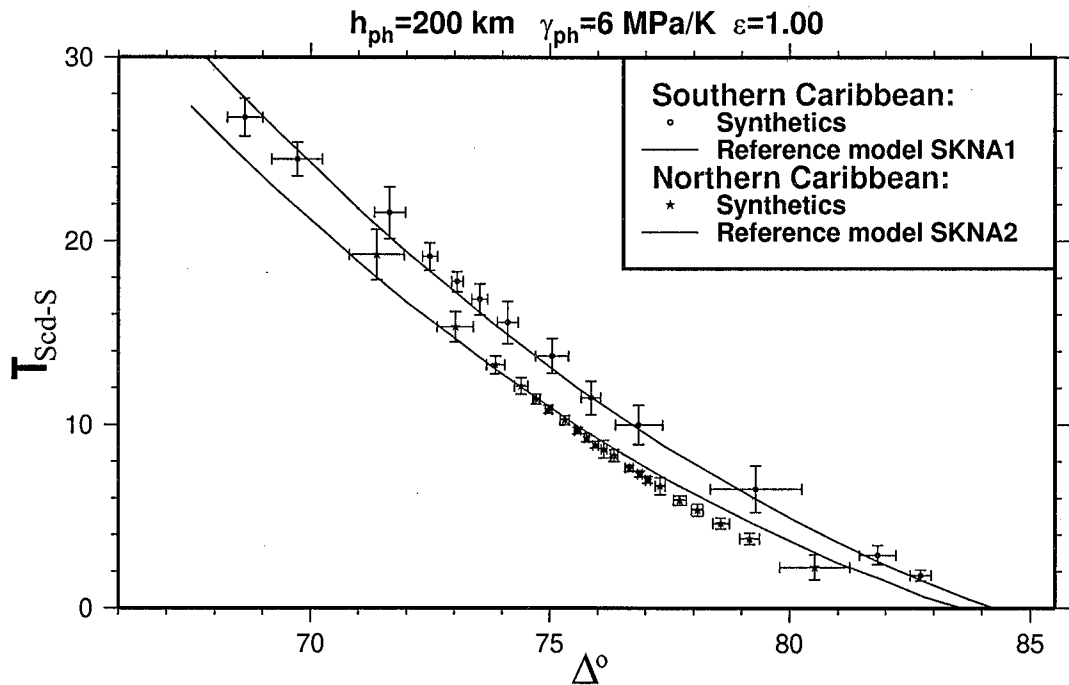
Figure 6.11: Scd-S differential travel times computed for two regions in Central America (for the convenience of analysis a running mean is computed in groups of 20; the error bars indicate the standard error) along with predictions of 1-D seismic reference models for those regions. The synthetics are computed for the preferred model ($h_{\mathrm{ph}} = 200$ km, $\gamma_{\mathrm{ph}} = 6$ MPa/K, $\epsilon = 1$).

interesting to explore if the currently existing tomography models provide sufficient detail in the lower mantle structure to account for the observed variations in relative Scd strength assuming a global phase transition with a 1.5% shear velocity jump. In Figure 6.1 we show two cross-sections through Grand's tomography model along two paths sampling D" beneath Central America. The paths have the same (to within 0.1°) epicentral distance and both sample faster than average structures at the base of the mantle. Also shown in Figure 6.1 are the vertical cross-sections through ScS bounce points. Note that the velocity profile in Figure 6.1a has a slightly higher gradient accompanying the discontinuity due to a faster velocity in the lowermost layer of the tomography model. In addition, the lateral extent of the fast velocity anomaly at the base of the mantle in Figure 6.1a is larger than in Figure 6.1b. A combination of these two factors leads to a pronounced difference in the predicted Scd amplitudes. The Green's functions computed for the two paths are shown in Figure 6.12. The path from event 940808 to station SHW samples D" beneath the Western Caribbean where there are strong observations of the D" triplication. The path from event 940110 to station FRB corresponds to one of the paths beneath Eastern Caribbean where a study by *Kendall and Nangini* [1996] did not detect any Scd. Figure 6.12 suggests that the variations of the local structure accompanying the discontinuity may be responsible for this apparent local disappearance of the D" discontinuity. An Scd signal as small as our model predictions for path 940110-FRB may be well below the detectability level, especially when noise is present.

Figure 6.13 shows a cross-section through Grand's tomography model for a path from event 840615 (Fiji-Tonga) to station Mammoth Lakes (MLAC) sampling the D" region beneath Central Pacific. The base of the mantle for paths across Central Pacific is characterized by a broad slow velocity anomaly which significantly reduces the local radial gradient of shear velocity and, for our preferred model of the phase transition characterized by a positive Clapeyron slope of 6 MPa/K, brings the discontinuity closer to the CMB. Although the amplitude of the velocity jump across the discontinuity remains 1.5%, the reduced vertical gradients have a dramatic effect on the amplitude of Scd making the phase barely detectable. The Green's function
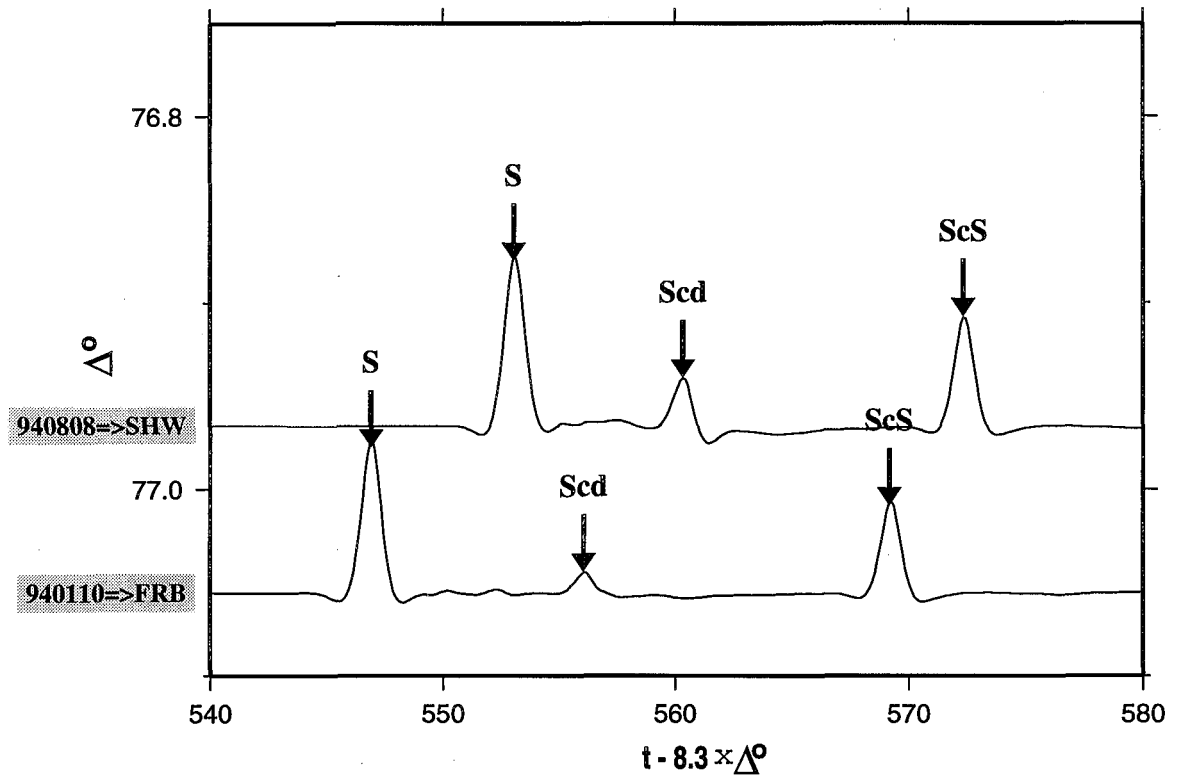
Figure 6.12: Synthetic Green's functions computed for two paths beneath Central America using the preferred model. The cross-sections through Grand's tomography model along the paths are given in Figure 6.1.

computed for this path is given in Figure 6.14. Such a weak Scd signal is representative of our predictions for all the paths across Central Pacific and may explain why the D" discontinuity beneath Central Pacific is so hard to detect.

The strength of the D" triplication can be characterized by the Scd/S amplitude ratio. In Figure 6.15 we present these ratios obtained from the synthetics computed for Central America and Central Pacific using the preferred model. For Central Pacific we use the amplitude of the strongest arrival observed between the direct S and core-reflected ScS phases. As noted above and can be seen in Figure 6.14, these arrivals are quite faint and have no consistency in timing and so are not Scd phases per se. As Figure 6.15 shows, the relative strength of Scd phase is substantially higher for Central America than for the Pacific, with the amplitude ratios increasing with distance for both regions. For a meaningful comparison of the relative strength of the triplication, this distance trend must be removed. We do this by normalizing the Scd/S ratios by the average distance trend. This average trend is obtained by computing polynomial fits to the amplitude ratios separately for each region and taking the average of the two. In Figure 6.16 we present the computed geographical patterns of the relative strength of the D" triplication. Each colored square in Figure 6.16 represents the average value of normalized by the average distance trend Scd/S amplitude ratios for all paths that have surface projection of ScS bounce points within the square. The figure suggests a very weak triplication for Central Pacific with much more pronounced Scd amplitudes for Central America. The strongest triplication is predicted for bounce points beneath Yucatan Peninsula and just east of it beneath the Cayman Trough. However, further east the computed amplitudes of Scd decrease which may explain why no evidence of a triplication has been found for that region [*Kendall and Nangini*, 1996].

6.6 Waveform modeling

A stronger test to the viability of our models can be performed by waveform modeling. The observed seismic waveforms carry a wealth of information about the earthquake
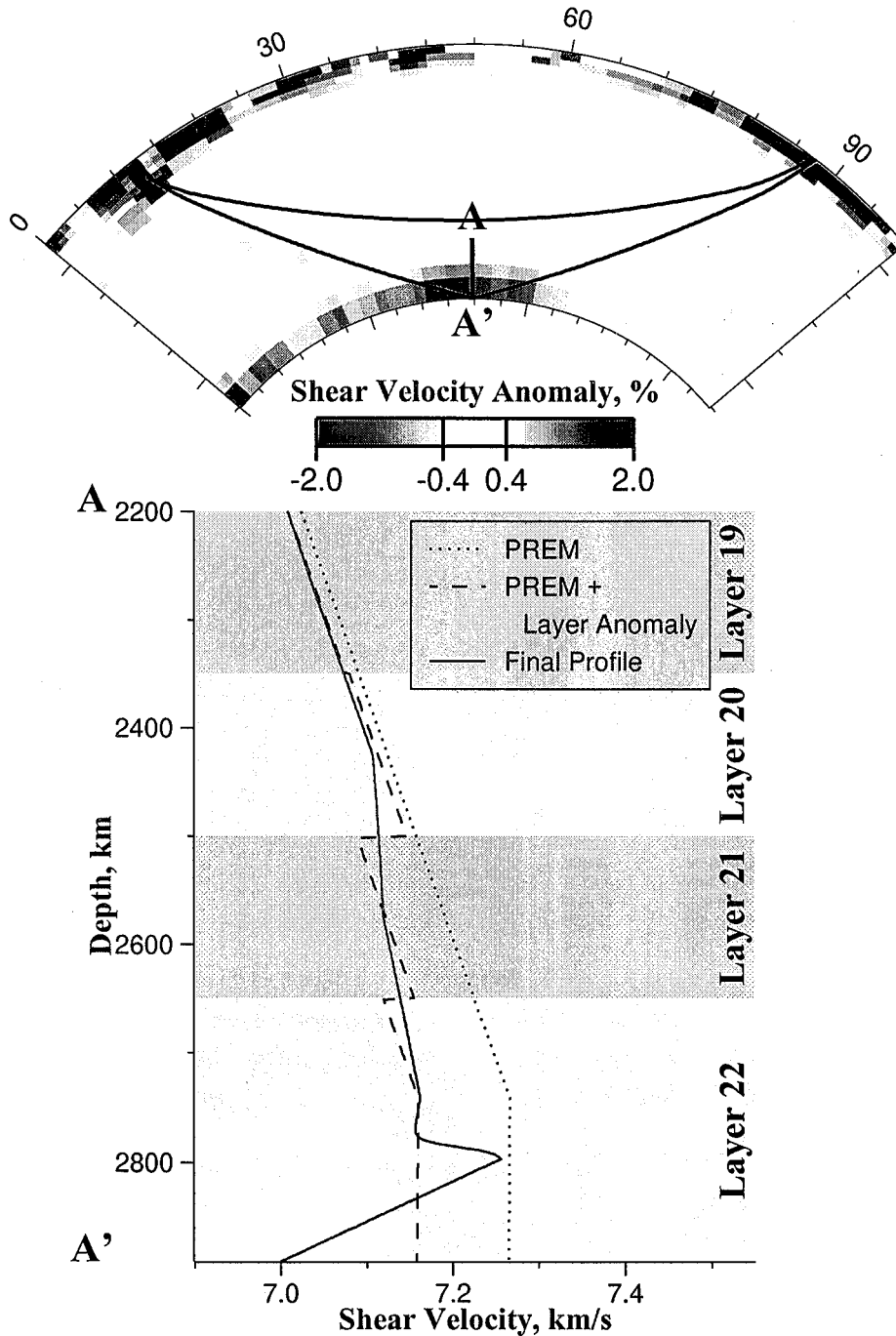
Figure 6.13: Velocity cross-section through Grand's tomography model along a path from event 840615 (Fiji-Tonga) to station Mammoth Lakes (MLAC). The path samples D" structure beneath Central Pacific. The direct S phase and core reflection (ScS) are shown. The bottom panel shows the vertical velocity profile through the ScS bounce point computed by imposing a a 1.5% discontinuity on Grand's tomography model. The shade indicates the four lowermost layers in the tomography model parameterization.
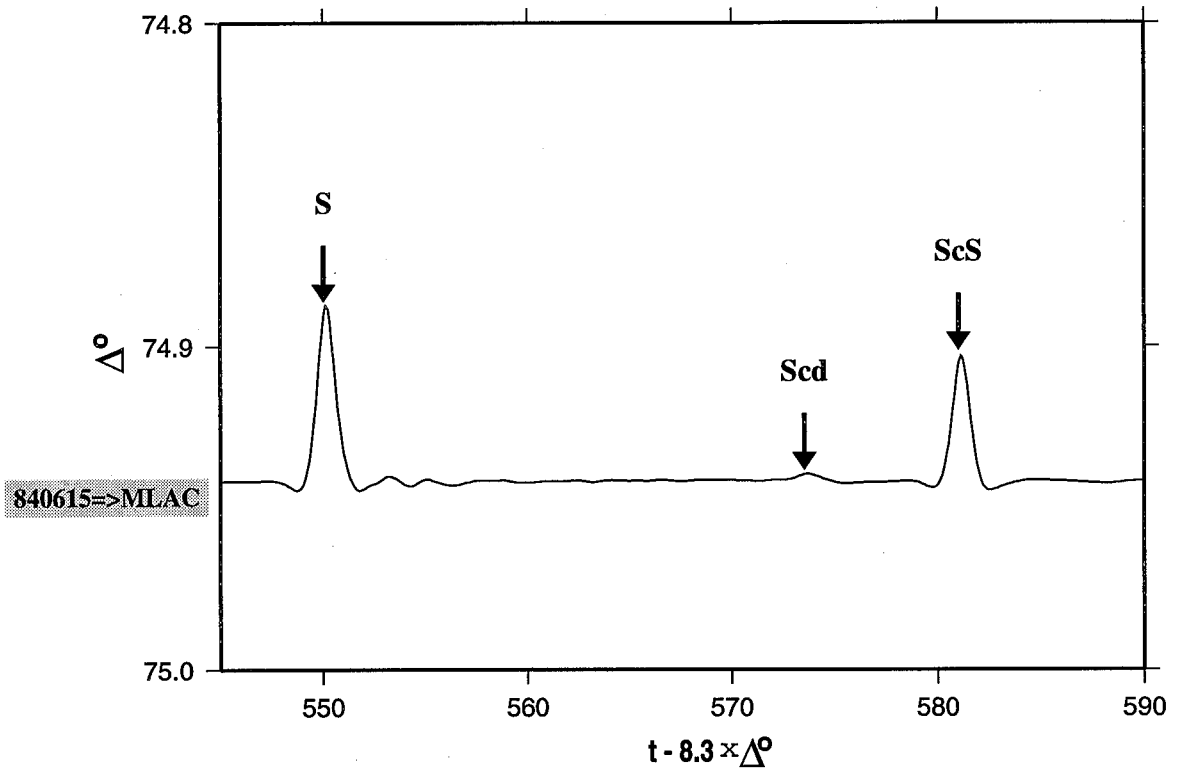
Figure 6.14: Synthetic Green's functions computed for a path beneath Central Pacific using the preferred model. The cross-section through Grand's tomography model along the path is given in Figure 6.13.
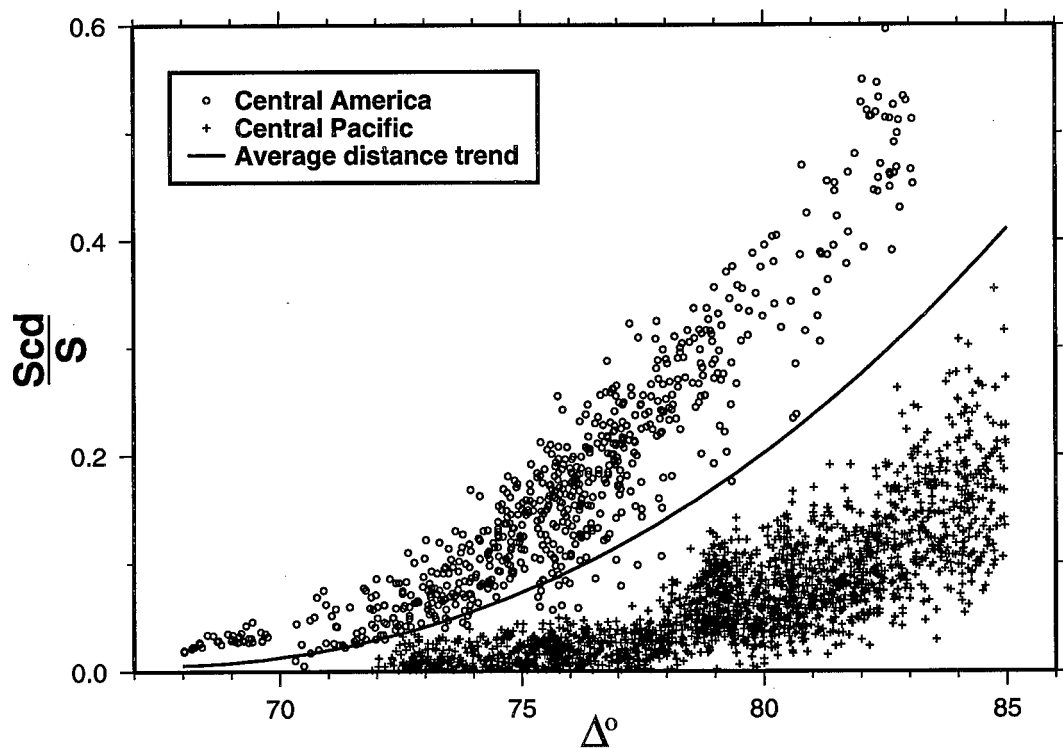
Figure 6.15: Computed Scd/S amplitude ratios for Central America and Central Pacific for our preferred model (h_{ph} = 200 km, γ_{ph} = 6 MPa/K, ϵ = 1.0). The line shows the average distance trend computed by averaging the values obtained by fitting polynomials of degree 3 separately to the data for Central America and the Central Pacific region.
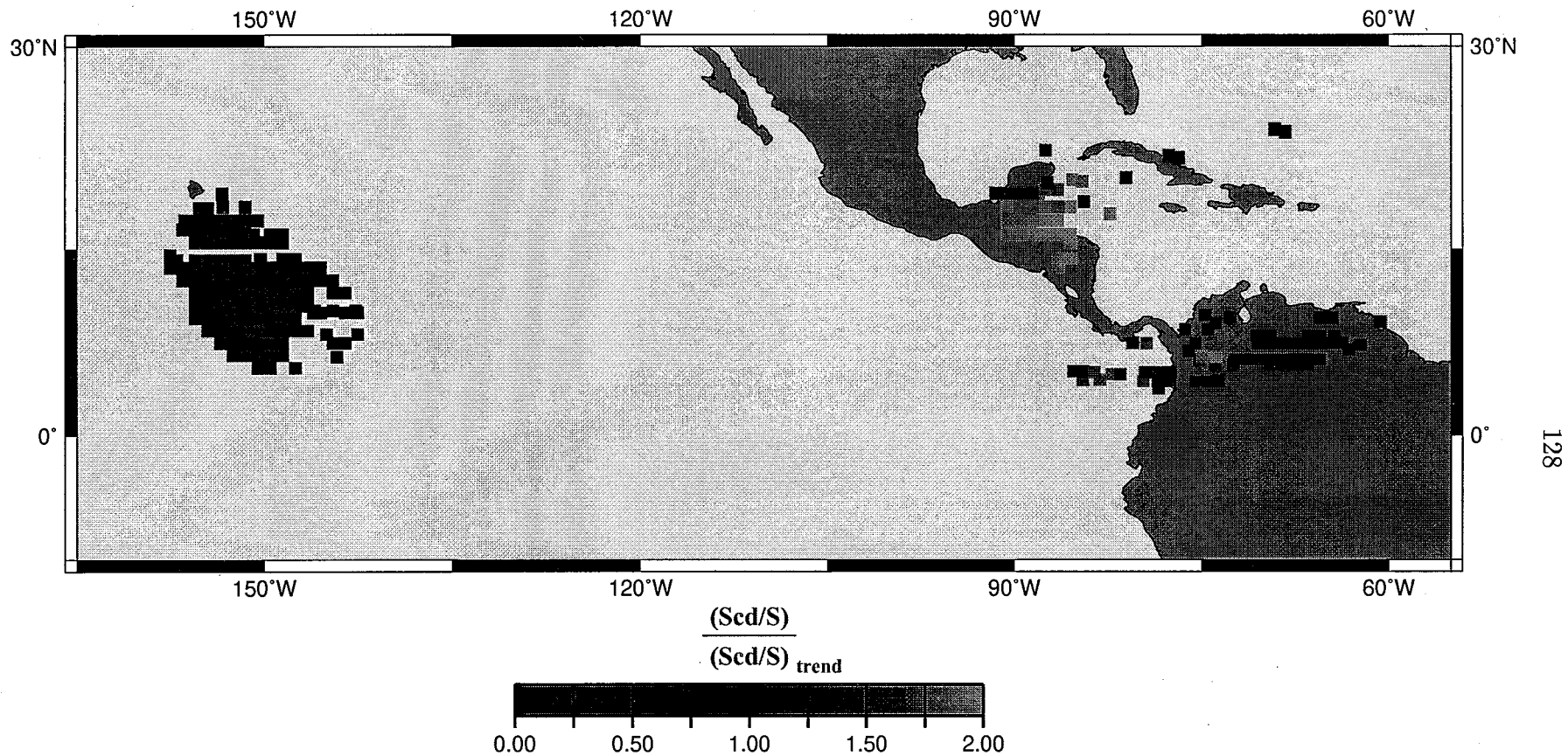
Figure 6.16: Predicted relative strength of D" triplication for Central America and Central Pacific. The color of the squares indicates the average value of Scd/S amplitudes corrected for the distance trend (Figure 6.15) for all paths that have an ScS bounce point surface projection within the square. The dimensions of the squares is $1° \times 1°$.

mechanisms and the structure of the Earth, including not only the velocity structure on many levels of detail, but also inelastic properties (attenuation). At the current resolution, tomography models recover just the longest wavelengths of heterogeneity in the mantle and contain no information about the inelastic properties. Therefore, reproduction by our models of even some of the more prominent long-period features of the observed waveforms should be viewed as very encouraging.

Figure 6.17 presents a comparison of synthetics computed for the preferred model with the data for Eurasia. The left panel shows a WWSSN record section. The middle panel presents synthetics computed for the original Grand's model without a discontinuity added. The panel on the right shows synthetics computed for our preferred composite model combining Grand's tomography model and a 1.5% discontinuity. The computed Green's functions are convolved with a WWSSN long-period instrument response. A trapezoidal source function with 2.5 s ramps and a 2.5 s plateau is used. All traces are aligned by the first arrival predicted by the 1-D reference model SGLE. The travel time curves predicted by model SGLE are also indicated for reference. In general, our model reproduces S waveform fairly well. Scd is also rather well reproduced for the two records (stations VAL and TRI) that have the clearest Scd arrival. For stations STU and IST, however, data shows no Scd arrival, while the phase still shows strong on the synthetics with a discontinuity. Note that no Scd phase is produced by Grand's tomography model without a discontinuity inclusion. The core reflection, ScS, is the most poorly reproduced phase. Not only is its amplitude poorly predicted by our model for some stations (COP, TAB, ESK, ATU), but its arrival time becomes highly anomalous at large distance (stations PTO and TOL). This anomaly is likely attributed to the introduction of the negative gradient at the base of the mantle in our models which slows down ScS that travel substantial distances in this region of reduced velocity.

Figure 6.18 compares a WWSSN record section (left panel) for Alaska with synthetics computed for Grand's tomography model with (right panel) and without (middle panel) an imposed discontinuity at the top of D". All traces are aligned by the first arrival predicted by model SYLO and the travel time curves computed for this

model are plotted for reference. The model with an imposed discontinuity (preferred model) fairly well reproduces the observed S and Scd phases for stations SFA, MNT, SCP, and OGD. The discrepancy is more pronounced for stations GEO and BLA, but still is rather minor. Again, ScS is the most poorly reproduced phase.

6.7   Discussion

The apparent spatial intermittance of the D" discontinuity has been one of the long standing mysteries of seismology and geodynamics. Seismologists have been mapping the existence of the discontinuity and its topography using 1-D techniques based solely on observed relative amplitudes and differential travel times. Geodynamicists have been searching for dynamic mechanisms that could make the discontinuity locally disappear while mineral physicists have been providing possible explanations to the apparent regional variations in the velocity contrast across the discontinuity. In Chapters 4 and 5 we suggested that it is possible that there exists a ubiquitous phase transition at the base of the mantle and the seismic triplication associated with it is largely modulated by the local structure. If the variation in the accompanying gradients is sufficiently strong, the triplication may be quite distinct in some regions while completely fading away in others. In this study we tested this hypothesis using the most comprehensive constraints on the global shear velocity structure of the mantle that are currently available and found out that, indeed, this is a viable hypothesis. The most attractive feature of our model is that it naturally reconciles the seismological observations pertaining to the D" triplication with geodynamics and removes some of the problems an intermittent discontinuity poses for the thermoelastic properties and mineralogy of the lower mantle. First of all, it provides consistent predictions of the observed regional patterns in the differential travel times and relative amplitudes, therefore satisfying most of the seismological constraints. It also does not require a fortuitous variation of composition or thermoelastic properties to provide variations of the velocity contrast across the discontinuity from 0% (for regions with no observed triplication) to 3% (as 1-D studies suggest for regions with
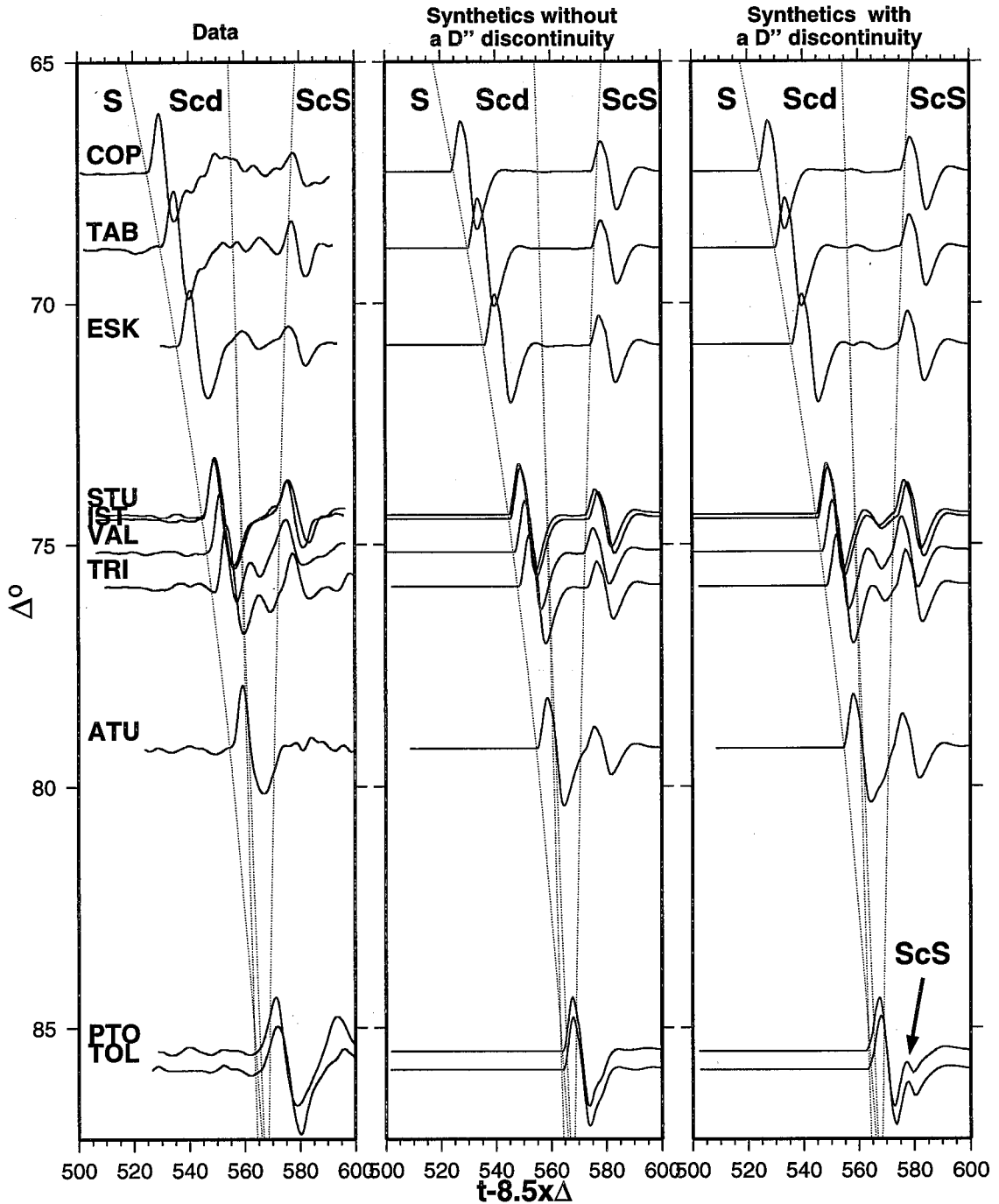
Figure 6.17: Record section (left) from event 710129 (Sea of Okhotsk) to stations in western Europe and synthetics (middle and right). Synthetics in the middle panel are computed using the original Grand's tomography model. Synthetics in the right panel are computed using the preferred model combining Grand's tomography model and a 1.5% velocity jump across a phase transition characterized by $h_{ph} = 200$ km and $\gamma_{ph} = 6$ MPa/K. All traces are aligned by the first arrival predicted by 1-D reference model SGLE. The travel time curves computed for this model are shown for reference. Arrows in the right panel indicate the anomalous ScS phase.
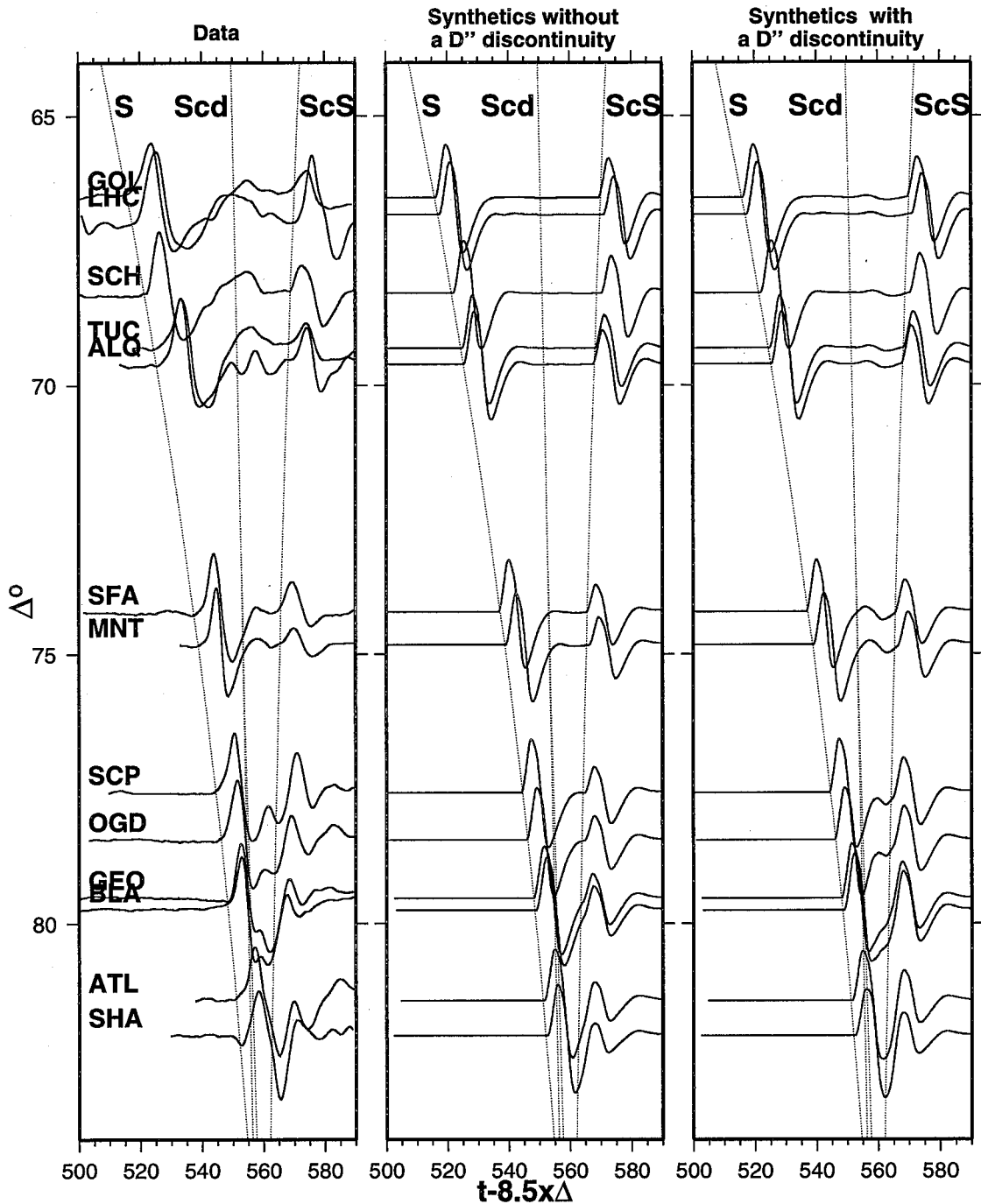
Figure 6.18: Record section (left) from event 700905 (Sea of Okhotsk) to stations in North America and synthetics (middle and right). Synthetics in the middle panel are computed using the original Grand's tomography model. Synthetics in the right panel are computed using the preferred model combining Grand's tomography model and a 1.5% velocity jump across a phase transition characterized by $h_{ph} = 200$ km and $\gamma_{ph} = 6$ MPa/K. All traces are aligned by the first arrival predicted by 1-D reference model SYLO. The travel time curves computed for this model are shown for reference.

strong evidence for a D" triplication). While such variations are not precluded, we demonstrate that most of the observations can be explained even when a constant amplitude of the velocity jump is used globally. Our modeling indicates that the level of detail resolved by Grand's tomography model is sufficient to provide the required variation in the relative strength of the Scd phase. Waveform modeling proves that the model predicts the amplitude of Scd phase consistent with observations beneath Eurasia (Figure 6.17) and Alaska (Figure 6.18), while the phase practically vanishes beneath Central Pacific or in the north-eastern part of the Caribbean.

It appears interesting that the analysis performed in this study using shear velocity structure inferred by tomography and an independent study using 2-D dynamic models (Chapter 5) suggest similar values for the characteristics of the possible phase transition most compatible with seismic observations. This may indicate that the dynamic models indeed simulate the same processes in the Earth that are imaged by mantle tomography. However, this apparent agreement of the predictions, in particular the value of the Clapeyron slope, γ_{ph}, should be looked at with caution. Tomography models suggest that the structure in the mid-mantle is considerably smoother than at the base, therefore, the variation in T_{Scd-S} is mostly due to the variation in T_{Scd}. If this is true, then the preference for positive values of γ_{ph} clearly suggested by the comparison of various models in this study (Figure 6.7) may simply indicate that the observed variation in T_{Scd-S} differential travel times is largely caused by the volumetric anomalies accompanying the discontinuity. The travel time of Scd phase can be perturbed by either introducing a volumetric anomaly along its path at the base of the mantle or varying the length of the path by adjusting the depth of the D" discontinuity. Imposing a phase transition with a positive Clapeyron slope has essentially the same effect on T_{Scd} as increasing the amplitude of the anomalies accompanying the discontinuity. To slow down the Scd phase one needs to either add a slow velocity anomaly at the base of the mantle or increase the path of Scd by depressing the discontinuity. Likewise, the travel time of Scd phase can be decreased by either adding a fast velocity anomaly at the base of the mantle or reducing the length of the path by elevating the discontinuity. In both cases the change of the elevation

is consistent with a phase transition characterized by a positive γ_{ph}. The opposite is true for a negative value of γ_{ph} as a basal phase transition with a negative Clapeyron slope tends to counteract the effects of the local velocity structure on the T_{Scd} travel time. According to our analysis, there is evidence that the volumetric anomalies are to some extent responsible for the observed regional patterns. As Figure 6.4b demonstrates, increasing the amplitudes of volumetric anomalies improves the fit to the data. However, as we mentioned in section 6.4, it is unclear to what extent the anomalies suggested by tomography models can be globally scaled. An alternative adjustment of tomographic models may include local enhancement of the structure. Such approach was used, for example, by *Liu et al.* [1998] to produce sufficiently sharp gradients in D" to give rise to a seismic triplication. However, we believe that arbitrary modification of the tomographic structure unconstrained by any particular physical model may be biased and may lead to ungrounded conclusions. It may be possible that the volumetric anomalies alone can account for most of the observed variations in T_{Scd-S}, even when the discontinuity is flat. However, at the current resolution of tomography models it appears that some topography is required for the discontinuity and this topography is consistent with a phase transition characterized by a positive value of Clapeyron slope of about 6 MPa/K.

One of the assumptions we make in the process of incorporating a phase transition into the tomography model is the purely thermal nature of the velocity anomalies recovered by tomography. This direct mapping between velocity and temperature suggests thermal anomalies in excess of 2000 K in some regions beneath Central Pacific and Africa, where shear velocity anomaly is more than 4% slower than average. Therefore, a quite deep (50 km above CMB) discontinuity is predicted by our preferred model for these regions. Such inferred thermal anomalies are perhaps too extreme suggesting that at least some of the velocity anomaly in those regions should be attributed to compositional heterogeneity or partial melting [*Lay et al.*, 1998]. It has been recently proposed by *Wysession et al.* [1999] that some presence of partial melt may be characteristic of the ambient D" and melt-free mantle material can only be present where D" layer has been cooled by introduction of subducted

lithosphere. If this hypothesis is true, our velocity to temperature mapping would be less justified beneath Central Pacific than beneath Eurasia, Alaska, India or Central America as each of the latter four regions is linked to paleo subduction zones. Any compositional stratification of the lower mantle (e.g., [*Kellogg et al.*, 1999; *van der Hilst and Kárason*, 1999]) is also expected to be displaced by subducting slabs, therefore making the linear scaling between seismic velocity and temperature more robust in regions associated with subduction. However, possible presence of partial melt or chemical inhomogeneity may lead to an underestimated value of the discontinuity elevation predicted by our preferred model anomalously slow regions, such as beneath Central Pacific. This, however, should not significantly affect the predicted amplitudes as the slow velocity zone at the base of the mantle in Central Pacific is rather thick (Figure 6.13) and elevating the discontinuity by about 100 km will not change the structural context of the discontinuity.

We have noted that our modification of Grand's tomography model affects some of the phases, in particular, ScS, that travel significant distances in the reduced velocity zone at the base of the mantle. This region with a negative velocity gradient is introduced to compensate the travel time increase due to the imposed discontinuity. While a moderate negative gradient at the base is consistent with both dynamic implications and seismic waveform modeling, the gradient in our models may be exaggerated. Such an extreme gradient may have an even more pronounced impact on the travel times of diffracted phases, such as S_{diff}. An alternative way of compensating for the travel time increase caused by the discontinuity insertion could be by reducing the velocity above the discontinuity. This, however, would require a different parameterization of the velocity profiles and call for a physical model based on which such adjustments could be made.

One of the main questions that remains, of course, is the nature of the suggested phase transition. Some of the possibilities were discussed in Chapter 5. Here we would like to once again emphasize that the uncertainties in the composition of the lower mantle and the limited accuracy of experimental mineral physics at simultaneous high pressures and temperatures leave many possibilities open, particularly given the

relatively small value of the shear velocity contrast (1-1.5%) that our studies suggest for the phase transition.

6.8 Conclusions

We have demonstrated that a phase transition at the base of the mantle is a viable explanation for the D" seismic triplication. When a phase transition is added to the larger scale shear velocity structure recovered by seismic tomography, the combination of the volumetric anomalies and topography of the phase transition produce substantial variations in differential travel times. We have shown that for a 1.5% velocity jump, $h_{\mathrm{ph}} = 200$ km and $\gamma_{\mathrm{ph}} = 6$ MPa/K (our preferred model), the regional patterns of these variations are consistent with seismological observations. We also find that the velocity anomalies imaged by tomography produces the observed trends in the differential travel times even for a flat discontinuity. However, the amplitude of these anomalies, even if scaled by 50%, is not sufficient to explain the observed variations. Additional topography is therefore required for the discontinuity and this topography must be correlated with the volumetric anomalies: the discontinuity must be more elevated in faster than average regions and more depressed in slower than average regions. Otherwise the variations in the depth of the discontinuity would tend to counteract the effects of velocity anomalies on the differential travel times. This, according to Chapter 4, strongly suggests a phase transition with a positive value of Clapeyron slope.

The large-scale shear velocity structure inferred by Grand's tomography model contains sufficient detail to produce an apparent intermittent triplication. The broad fast anomalies at the base of the mantle, such as, for example, beneath Alaska or Eurasia, tend to amplify Scd arrivals producing a strong triplication. The slow velocity anomalies, such as beneath Central Pacific, tend to obscure the triplication and produce very weak Scd phase that can be easily lost in noise. Using waveform modeling, we also demonstrated that the velocity gradients predicted by Grand's tomography model alone cannot produce a triplication and a first-order discontinuity

is required.

Due to the tendency of tomographic models to smear the recovered structure and the existing tradeoffs between volumetric anomalies and the topography of the discontinuity, our estimates of the most plausible phase change characteristics are uncertain. However, we believe that the progress being rapidly made in tomographic studies including both the addition of new data and data types and employing more advanced inversion techniques will soon make it possible to provide more definite answers to the questions addressed in this study.

Bibliography

Agnon, A., and M. S. T. Bukowinski, δ_S at high pressure and $d\ln V_S/d\ln V_P$ in the lower mantle, *Geophys. Res. Lett.*, *17*, 1149–1152, 1990.

Anderson, D. L., A seismic equation of state II. Shear properties and thermodynamics of the lower mantle, *Phys. Earth Planet. Inter.*, *45*, 307–323, 1987.

Anderson, D. L., Temperature and pressure derivatives of elastic constants with application to the mantle, *J. Geophys. Res.*, *93*, 4688–4700, 1988.

Anderson, O. L., Equation for thermal expansivity in planetary interiors, *J. Geophys. Res.*, *72*, 3661–3668, 1967.

Anderson, O. L., and D. G. Isaak, The dependence of the Anderson-Grüneisen parameter δ_T upon compression at extreme conditions, *J. Phys. Chem. Solids*, *54*, 221–227, 1993.

Anderson, O. L., and K. Masuda, A thermodynamic method for computing thermal expansivity, α, versus T along isobars for silicate perovskite, *Phys. Earth Planet. Inter.*, *85*, 227–236, 1994.

Anderson, O. L., H. Oda, and D. Isaak, A model for the computation of thermal expansivity at high compression and high temperatures: MgO as an example, *Geophys. Res. Lett.*, *19*, 1987–1990, 1992.

Anderson, O. L., H. Oda, A. Chopelas, and D. G. Isaak, A thermodynamic theory of the Grüneisen ratio at extreme conditions: MgO as an example, *Phys. Chem. Miner.*, *19*, 369–380, 1993.

Anderson, O. L., K. Masuda, and D. Guo, Pure silicate perovskite and the PREM lower mantle model: a thermodynamic analysis, *Phys. Earth Planet. Inter.*, *89*, 35–49, 1995.

Anderson, O. L., K. Masuda, and D. G. Isaak, Limits on the value of δ_T and γ for MgSiO$_3$ perovskite, *Phys. Earth Planet. Inter.*, *98*, 31–46, 1996.

Birch, F., Elasticity and constitution of the Earth's interior, *J. Geophys. Res.*, *57*, 227–286, 1952.

Breger, L., B. Romanowicz, and L. Vinnik, Test of tomographic models of D" using differential travel time data, *Geophys. Res. Lett.*, *25*, 5–8, 1998.

Breuer, D., D. A. Yuen, T. Spohn, and S. Zhang, Three-dimensional models of Martian mantle convection with phase transitions, *Geophys. Res. Lett.*, *25*, 229–232, 1998.

Bukowinski, M. S., and G. H. Wolf, Thermodynamically consistent decompression: Implications for lower mantle composition, *J. Geophys. Res.*, *95*, 12583–12593, 1990.

Bunge, H.-P., M. A. Richards, and J. R. Baumgardner, Effect of depth-dependent viscosity on the planform of mantle convection, *Nature*, *379*, 436–438, 1996.

Bunge, H. P., M. A. Richards, C. Lithgow-Bertelloni, J. R. Baumgardner, S. P. Grand, and B. A. Romanowicz, Time scales and heterogeneous structure in geodynamic Earth models, *Science*, *280*, 91–95, 1998.

Burdick, L., and D. L. Anderson, Interpretation of velocity profiles of the mantle, *J. Geophys. Res.*, *80*, 1070–1074, 1975.

Butler, R., and D. L. Anderson, Equation of state fits to the lower mantle and outer core, *Phys. Earth Planet. Inter.*, *17*, 147–162, 1978.

Chopelas, A., Thermal expansivity of lower mantle phases MgO and MgSiO$_3$ perovskite at high pressure derived from vibrational spectroscopy, *Phys. Earth Planet. Inter.*, *98*, 3–15, 1996.

Chopelas, A., and R. Boehler, Thermal expansivity in the lower mantle, *Geophys. Res. Lett.*, *19*, 1983–1986, 1992.

Christensen, U., Convection with pressure- and temperature-dependent non-Newtonian rheology, *Geophys. J. R. astr. Soc.*, *77*, 343–384, 1984.

Christensen, U., Effects of phase transitions on mantle convection, *Ann. Rev. Earth Planet. Sci.*, *23*, 65–87, 1995.

Christensen, U. R., The influence of trench migration on slab penetration into the lower mantle, *Earth Planet. Sci. Lett.*, *140*, 27–39, 1996a.

Christensen, U. R., Compositional heterogeneity of D" by segregation of subducted oceanic crust, in *EOS, Fall Meeting Supplement*, vol. 77, p. 709, 1996b, abstract.

Christensen, U. R., and A. W. Hofmann, Segregation of subducted oceanic crust in the convecting mantle, *J. Geophys. Res.*, *99*, 19,867–19,884, 1994.

Christensen, U. R., and D. A. Yuen, The interaction of a subducting lithospheric slab with a chemical or phase boundary, *J. Geophys. Res.*, *89*, 4389–4402, 1984.

Cohen, R. E., I. I. Mazin, and D. G. Isaak, Magnetic collapse in transition metal oxides at high pressure: Implications for the Earth, *Science*, *275*, 654–657, 1997.

Davies, G. F., Incorporation of plates into mantle convection models, in *The history and dynamics of plate motion*, p. 42, Am. Geophys. Un., 1997.

Davies, G. F., and A. M. Dziewonski, Homogeneity and constitution of the Earth's lower mantle and outer core, *Phys. Earth Planet. Inter.*, *10*, 336–343, 1975.

Davies, G. F., and M. Gurnis, Interaction of mantle dregs with convection: Lateral heterogeneity at the core-mantle boundary, *Geophys. Res. Lett.*, *13*, 1517–1520, 1986.

Ding, X., and D. V. Helmberger, Modeling D" structure beneath Central America with broadband seismic data, *Phys. Earth Planet. Inter.*, *101*, 245–270, 1997.

Dubrovinsky, L. S., S. K. Saxena, P. Lazor, R. Ahuja, O. Eriksson, J. M. Wills, and B. Johansson, Experimental and theoretical identification of a new high-pressure phase of silica, *Nature*, *388*, 362–365, 1997.

Duffy, T. S., and T. J. Ahrens, Thermal expansion of mantle and core materials at very high pressures, *Geophys. Res. Lett.*, *20*, 1103–1106, 1993.

Duffy, T. S., and D. L. Anderson, Seismic velocities in mantle minerals and the mineralogy of the upper mantle, *J. Geophys. Res.*, *94*, 1895–1912, 1989.

Dziewonski, A. M., and D. L. Anderson, Preliminary reference Earth model, *Phys. Earth Planet. Inter.*, *25*, 297–356, 1981.

Dziewonski, A. M., and J. H. Woodhouse, Global images of the Earth's interior, *Science*, *236*, 37–48, 1987.

Engebretson, D. C., K. P. Kelley, H. J. Cashman, and M. A. Richards, 180 million years of subduction, *GSA Today*, *2*, 93–100, 1992.

Fei, Y., and H. K. Mao, In situ determination of the NiAs phase of FeO at high pressure and temperature, *Science*, *266*, 1678–1680, 1994.

Forte, A. M., and W. R. Peltier, Core-mantle boundary topography and whole-mantle convection, *Geophys. Res. Lett.*, *16*, 621–624, 1989.

Funamori, N., and R. Jeanloz, High-pressure transformation of Al_2O_3, *Science*, *278*, 1109–1111, 1997.

Funamori, N., and T. Yagi, High pressure and high temperature in situ x-ray observation of $MgSiO_3$ perovskite under lower mantle conditions, *Geophys. Res. Lett.*, *20*, 387–390, 1993.

Gaffney, E. S., and D. L. Anderson, Effect of low-spin Fe^{2+} on the composition of the lower mantle, *J. Geophys. Res.*, *78*, 7005–7014, 1973.

Gaherty, J. B., and B. H. Hager, Compositional vs. thermal buoyancy and the evolution of subducted lithosphere, *Geophys. Res. Lett.*, *21*, 141–144, 1994.

Gaherty, J. B., and T. Lay, Investigation of laterally heterogeneous shear velocity structure in D" beneath Eurasia, *J. Geophys. Res.*, *97*, 417–435, 1992.

Garnero, E. J., and D. V. Helmberger, A very slow basal layer underlying large-scale low-velocity anomalies in the lower mantle beneath the Pacific: evidence from core phases, *Phys. Earth Planet. Inter.*, *91*, 161–176, 1995.

Garnero, E. J., D. V. Helmberger, and S. Grand, Preliminary evidence for a lower mantle shear wave velocity discontinuity beneath the central Pacific, *Phys. Earth Planet. Int.*, *79*, 335–347, 1993.

Grand, S. P., Mantle shear structure beneath the Americas and surrounding oceans, *J. Geophys. Res.*, *99*, 11591–11622, 1994.

Grand, S. P., R. D. van der Hilst, and S. Widiyantoro, Global seismic tomography: a snapshot of convection in the Earth, *GSA Today*, *7*, 1–7, 1997.

Griffiths, R. W., and J. S. Turner, Folding of viscous plumes impringing on a density or viscosity interface, *Geophys. J.*, *95*, 397–419, 1988.

Gurnis, M., The effects of chemical density differences on convective mixing in the Earth's mantle, *J. Geophys. Res.*, *91*, 11407–11419, 1986.

Gurnis, M., and G. F. Davies, Mixing in numerical models of mantle convection incorporating plate kinematics, *J. Geophys. Res.*, *91*, 6375–6395, 1986.

Gurnis, M., and B. H. Hager, Controls on the structure of subducted slabs, *Nature*, *335*, 317–321, 1988.

Hager, B. H., R. W. Clayton, M. A. Richards, R. P. Comer, and A. M. Dziewonski, Lower mantle heterogeneity, dynamic topography and the geoid, *Nature*, *313*, 541–545, 1985.

Han, L., and M. Gurnis, How valid are dynamic models of subduction and convection when plate motions are prescribed?, *Phys. Earth Planet. Inter.*, *110*, 235–246, 1999.

Hansen, U., and D. A. Yuen, Numerical simulations of thermal-chemical instabilities at the core-mantle boundary, *Nature*, *334*, 237–240, 1988.

Hansen, U., and D. A. Yuen, Dynamical influences from thermal-chemical instabilities at the core-mantle boundary, *Geophys. Res. Lett.*, *16*, 629–632, 1989.

Hemley, R. J., L. Stixrude, Y. Fei, and H. K. Mao, Constraints on lower mantle composition from $P - V - T$ measurements of (Fe,Mg)SiO$_3$-perovskite and (Fe,Mg)O, in *High-pressure research: Application to Earth and Planetary Sciences*, edited by Y. Syono and M. H. Manghnani, American Geophysical Union, Washington, DC, 1992.

Isaak, D. G., The mixed P, T derivatives of elastic moduli and implications on extrapolating throughout Earth's mantle, *Phys. Earth Planet. Inter.*, *80*, 37–48, 1993.

Isaak, D. G., O. L. Anderson, and T. Goto, Measured elastic moduli of single-crystal MgO up to 1800 K, *Phys. Chem. Minerals*, *16*, 704–713, 1989.

Isaak, D. G., R. E. Cohen, and M. J. Mehl, Calculated elastic and thermal properties of MgO at high pressures and temperatures, *J. Geophys. Res.*, *95*, 7055–7067, 1990.

Isaak, D. G., O. L. Anderson, and R. E. Cohen, The relationship between shear and compressional velocities at high pressures: Reconciliation of seismic tomography and mineral physics, *Geophys. Res. Lett.*, *19*, 741–744, 1992.

Jackson, I., and S. M. Rigden, Analysis of $P - V - T$ data: Constraints on the thermoelastic properties of high-pressure minerals, *Phys. Earth Planet. Inter.*, *96*, 85–112, 1996.

Jackson, I., and A. E. Ringwood, High-pressure polymorphism of the iron oxides, *Geophys. J. R. astr. Soc.*, *64*, 767–783, 1981.

Jeanloz, R., Phase transitions in the mantle, *Nature*, *340*, 184, 1989.

Jeanloz, R., and T. J. Ahrens, Equations of state of FeO and CaO, *Geophys J. R. astr Soc.*, *62*, 505–528, 1980.

Jeanloz, R., and E. Knittle, Reduction of mantle and core properties to a standard state by adiabatic decompression, in *Chemistry and physics of terrestrial planets*, edited by S. K. Saxena, Springer, 1986.

Jordan, T. H., P. Puster, G. A. Glatzmaier, and P. J. Tackley, Comparisons between seismic earth structures and mantle flow based on radial correlation functions, *Science*, *261*, 1427–1431, 1993.

Karki, B. B., M. C. Warren, L. Stixrude, G. J. Ackland, and J. Crain, *Ab initio* studies of high-pressure structural transformations in silica, *Phys. Rev. B*, *55*, 3465–3471, 1997a.

Karki, B. B., M. C. Warren, L. Stixrude, G. J. Ackland, and J. Crain, *Ab initio* studies of high-pressure structural transformations in silica, *Phys. Rev. B*, *56*, 2884–2884, 1997b.

Kellogg, L. H., Growing the earth's D" layer: Effects of density variations at the core-mantle boundary, *Geophys. Res. Lett.*, *24*, 2749–2752, 1997.

Kellogg, L. H., and S. D. King, Effect of mantle plumes on the growth of D" by reaction between the core and mantle, *Geophys. Res. Lett.*, *20*, 379–382, 1993.

Kellogg, L. H., B. H. Hager, and R. D. van der Hilst, Compositional stratification in the deep mantle, *Science*, *283*, 1881–1884, 1999.

Kendall, J.-M., and C. Nangini, Lateral variations in D" below the Caribbean, *Geophys. Res. Lett.*, *23*, 399–402, 1996.

Kendall, J.-M., and P. M. Shearer, Lateral variations in D" thickness from long-period shear wave data, *J. Geophys. Res.*, *99*, 11575–11590, 1994.

Kesson, S. E., and J. D. Fitz Gerald, Partitioning of MgO, FeO, NiO, MnO and Cr_2O_3 between magnesian silicate perovskite and magnesiowüstite: implications for the origin of inclusions in diamond and the composition of the lower mantle, *Earth Planet. Sci. Lett.*, *111*, 229–240, 1992.

King, S. D., and B. H. Hager, Subducted slabs and the geoid 1. Numerical experiments with temperature-dependent viscosity, *J. Geophys. Res.*, *99*, 19,843–19,852, 1994.

King, S. D., A. Raefsky, and B. H. Hager, ConMan: Vectorizing a finite element code for incompressible two-dimensional convection in the Earth's mantle, *Phys. Earth Planet. Inter.*, *59*, 195–207, 1990.

Kingma, K. J., R. E. Cohen, R. J. Hemley, and H. Mao, Transformation of stishovite to a denser phase at lower-mantle pressures, *Nature*, *374*, 243–245, 1995.

Knittle, E., and R. Jeanloz, High-pressure metallization of FeO and implications for the Earth's core, *Geophys. Res. Lett.*, *13*, 1541–1544, 1986.

Knittle, E., and R. Jeanloz, Synthesis and equation of state of (Mg, Fe)SiO$_3$ perovskite to over 100 gigapascals, *Science*, *235*, 668–670, 1987.

Knittle, E., and R. Jeanloz, Earth's core-mantle boundary: Results of experiments at high pressures and temperatures, *Science*, *251*, 1438–1443, 1991.

Knittle, E., R. Jeanloz, and G. L. Smith, Thermal expansion of silicate perovskite and stratification of the Earth's mantle, *Nature*, *319*, 214–216, 1986.

Lavely, E. M., D. W. Forsyth, and P. Friedemann, Scales of heterogeneity near the core-mantle boundary, *Geophys. Res. Lett.*, *13*, 1505–1508, 1986.

Lay, T., Localized velocity anomalies in the lower mantle, *Geophys. J. R. astr. Soc.*, *72*, 483–516, 1983.

Lay, T., and D. V. Helmberger, A lower mantle S wave triplication and the shear velocity structure of D", *Geophys. J. R. astr. Soc.*, *75*, 799–838, 1983.

Lay, T., E. J. Garnero, C. J. Young, and J. B. Gaherty, Scale lengths of shear velocity heterogeneity at the base of the mantle from S wave differential travel times, *J. Geophys. Res.*, *102*, 9887–9909, 1997.

Lay, T., Q. Williams, and E. J. Garnero, The core-mantle boundary layer and deep Earth dynamics, *Nature*, *392*, 461–468, 1998.

Lenardic, A., and W. M. Kaula, Tectonic plates, D" structure, and the nature of mantle plumes, *J. Geophys. Res.*, *99*, 15697–15708, 1994.

Li, B., S. M. Rigden, and R. C. Liebermann, Elasticity of stishovite at high pressure, *Phys. Earth Planet. Inter.*, *96*, 113–127, 1996.

Li, X. D., and B. Romanowicz, Global mantle shear velocity model developed using nonlinear asymptotic coupling theory, *J. Geophys. Res.*, *101*, 22245–22272, 1996.

Liu, X. F., J. Tromp, and A. Dziewonski, Is there a first-order discontinuity in the lowermost mantle?, *Earth Planet. Sci. Lett.*, *160*, 343–351, 1998.

Loper, D. E., and T. Lay, The core-mantle boundary region, *J. Geophys. Res.*, *100*, 6397–6420, 1995.

Mao, H. K., R. J. Hemley, Y. Fei, J. Shu, L. Chen, A. P. Jephcoat, W. Wu, and W. A. Basset, Effect of pressure, temperature, and composition on lattice parameters and density of (Fe, Mg)SiO$_3$-perovskites to 30 GPa, *J. Geophys. Res.*, *96*, 8069–8079, 1991.

Masters, G., S. Johnson, G. Laske, and H. Bolton, A shear-velocity model of the mantle, *Phil. Trans. R. Soc.*, *354*, 1385–1411, 1996.

Meade, C., H. K. Mao, and J. Hu, High temperature phase transition and dissociation of (Mg, Fe)SiO$_3$ perovskite at lower mantle pressures, *Science*, *268*, 1743–1745, 1995.

Mégnin, C., H. P. Bunge, B. Romanowicz, and M. Richards, Imaging 3-D spherical convection models: What can seismic tomography tell us about mantle dynamics?, *Geophys. Res. Lett.*, *24*, 1299–1302, 1997.

Mitrovica, J., and A. Forte, Radial profile of mantle viscosity: Results from the joint inversion of convection and postglacial rebound observables, *J. Geophys. Res.*, *102*, 2751–2769, 1997.

Moresi, L., and M. Gurnis, Constraints on the lateral strength of slabs from three-dimensional dynamic flow models, *Earth Planet. Sci. Lett.*, *138*, 15–28, 1996.

Morgan, J. P., and P. M. Shearer, Seismic constraints on mantle flow and topography of the 670 km discontinuity – evidence for whole mantle convection, *Nature*, *365*, 506–511, 1993.

Nataf, H.-C., and S. Houard, Seismic discontinuity at the top of D": A world-wide feature?, *Geophys. Res. Lett.*, *20*, 2371–2374, 1993.

Navrotsky, A., and P. K. Davies, Cesium chloride versus nickel arsenide as possible structures for (Mg, Fe)O in the lower mantle, *J. Geophys. Res.*, *86*, 3689–3694, 1981.

Ni, S., X. Ding, and D. V. Helmberger, Constructing synthetics for deep earth tomographic models, *Geophys. J. Int.*, 1999, in press.

Olson, P., and C. Kincaid, Experiments on the interaction of thermal convection and compositional layering at the base of the mantle, *J. Geophys. Res.*, *96*, 4347–4354, 1991.

Patel, A., G. D. Price, M. Matsui, J. Brodholt, and R. Howarth, A computer simulation approach to the high pressure thermoelasticity of MgSiO$_3$ perovskite, *Phys. Earth Planet. Inter.*, *98*, 55–63, 1996.

Ricard, Y., C. Vigny, and C. Froidevaux, Mantle heterogeneities, geoid, and plate motion: a Monte Carlo inversion, *J. Geophys. Res.*, *94*, 13739–13754, 1989.

Ricard, Y., M. Richards, C. Lithgow-Bertelloni, and Y. L. Stunff, A geodynamic model of mantle density heterogeneity, *J. Geophys. Res.*, *98*, 21,895–21,909, 1993.

Richards, M. A., and G. F. Davies, On the separation of relatively buoyant components from subducted lithosphere, *Geophys. Res. Lett.*, *16*, 831–834, 1989.

Richards, M. A., and D. C. Engebretson, Large-scale mantle convection and the history of subduction, *Nature*, *355*, 437–440, 1992.

Ruff, L., and D. L. Anderson, Core formation, evolution, and convection: A geophysical model, *Phys. Earth Planet. Inter.*, *21*, 181–201, 1980.

Russel, S., and T. Lay, Evidence for a shear-wave discontinuity in D" beneath the Central Pacific, in *EOS, Fall Meeting Supplement*, vol. 79, p. 618, 1998, abstract.

Sammis, C., D. L. Anderson, and T. Jordan, Application of isotropic finite strain theory to ultrasonic and seismological data, *J. Geophys. Res.*, *75*, 4478–4480, 1970.

Saxena, S. K., Earth mineralogical model: Gibbs free energy minimization computation in the system MgO-FeO-SiO_2, *Geochim. Cosmochim. Acta*, *60*, 2379–2395, 1996.

Schimmel, M., and H. Paulssen, Steeply reflected ScSH precursors from the D" region, *J. Geophys. Res.*, *101*, 1996.

Serghiou, G., A. Zerr, and R. Boehler, $(Mg,Fe)SiO_3$-perovskite stability under lower mantle conditions, *Science*, *280*, 1998.

Sherman, D. M., High-spin to low-spin transition of iron(II) oxides at high pressures: Possible effects on the physics and chemistry of the lower mantle. In: S. Ghose et al. (Editors), Structural and Magnetic Phase Transitions in Minerals, *Adv. Phys. Geochem.*, *7*, 113–128, 1988.

Sherman, D. M., and H. J. F. Jansen, First-principles prediction of the high-pressure phase transition and electronic structure of FeO: Implications for the chemistry of the lower mantle and core, *Geophys. Res. Lett.*, *22*, 1001–1004, 1995.

Sidorin, I., and M. Gurnis, Geodynamically consistent seismic velocity predictions at the base of the mantle, in *The Core-Mantle Boundary Region*, edited by M. Gurnis,

M. Wysession, E. Knittle, and B. Buffett, American Geophysical Union, Washington, DC, 1998.

Sidorin, I., M. Gurnis, D. V. Helmberger, and X. Ding, Interpreting D" seismic structure using synthetic waveforms computed from dynamic models, *Earth Planet. Sci. Lett.*, *163*, 31–41, 1998.

Sleep, N. H., Gradual entrainment of a chemical layer at the base of the mantle by overlying convection, *Geophys. J. Int.*, *95*, 437–447, 1988.

Stacey, F. D., Thermoelasticity of (Mg, Fe)SiO₃ perovskite and a comparison with the lower mantle, *Phys. Earth Planet. Inter.*, *98*, 65–77, 1996.

Stixrude, L., and M. S. T. Bukowinski, Fundamental thermodynamic relations and silicate melting with implications for the constitution of D", *J. Geophys. Res.*, *95*, 19311–19325, 1990.

Stixrude, L., and R. E. Cohen, Stability of orthorhombic MgSiO₃ perovskite in the Earth's lower mantle, *Nature*, *364*, 613–615, 1993.

Stixrude, L., R. J. Hemley, Y. Fei, and H. K. Mao, Thermoelasticity of silicate perovskite and magnesiowüstite and stratification of the Earth's mantle, *Science*, *257*, 1099–1101, 1992.

Strens, R. G. J., The nature and geophysical importance of spin-pairing in minerals of iron (II), in *The Physics and Chemistry of Minerals and Rocks*, edited by S. K. Runcorn, John Wiley, New York, 1969.

Su, W., R. L. Woodward, and A. M. Dziewonski, Degree 12 model of shear velocity heterogeneity in the mantle, *J. Geophys. Res.*, *99*, 6945–6980, 1994.

Suzuki, I., Thermal expansion of periclase and olivine, and their anharmonic properties, *J. Phys. Earth*, *23*, 145–159, 1975.

Suzuki, I., S. Okajima, and K. Seya, Thermal expansion of single-crystal manganosite, *J. Phys. Earth*, *27*, 63–69, 1979.

Tackley, P., Three-dimensional simulations of mantle convection with a thermoche-mical CMB boundary layer: D"?, in *The Core-Mantle Boundary Region*, edited by M. Gurnis, M. Wysession, E. Knittle, and B. Buffett, American Geophysical Union, Washington, DC, 1998.

Tackley, P. J., D. J. Stevenson, G. A. Glatzmaier, and G. Schubert, Effects of an endothermic phase transition at 670 km depth in a spherical model of convection in the Earth's mantle, *Nature*, *361*, 699–704, 1993.

Tsuchida, Y., and T. Yagi, A new, post-stishovite high-pressure polymorph of silica, *Nature*, *340*, 217–220, 1989.

Utsumi, W., N. Funamori, T. Yagi, E. Ito, T. Kikegawa, and O. Shimomura, Thermal expansivity of $MgSiO_3$ perovskite under high pressures up to 20 GPa, *Geophys. Res. Lett.*, *22*, 1005–1008, 1995.

van der Hilst, R. D., and H. Kárason, Compositional heterogeneity in the bottom 1000 km of Earth's mantle: toward a hybrid convection model, *Science*, *283*, 1885–1888, 1999.

van der Hilst, R. D., S. Widiyantoro, and E. R. Engdahl, Evidence for deep mantle circulation from global tomography, *Nature*, *386*, 578–584, 1997.

van Heijst, H. R., and J. Woodhouse, Global high resolution overtone and fundamen-tal mode surface wave phase velocity distributions determined using mode branch stripping, *Geophys. J. Int.*, 1998, submitted.

van Keken, P. E., S. D. King, H. Schmeling, U. R. Christensen, D. Neumeister, and M.-P. Doin, A comparison of methods for the modeling of thermochemical convection, *J. Geophys. Res.*, *102*, 22477–22495, 1997.

Vassiliou, M. S., and T. J. Ahrens, The equation of state of $Mg_{0.6}Fe_{0.4}O$ to 200 GPa, *Geophys. Res. Lett.*, *9*, 127–130, 1982.

Vidale, J. E., and H. M. Benz, Seismological mapping of fine structure near the base of the Earth's mantle, *Nature*, *361*, 529–532, 1993.

Wang, Y., D. J. Weidner, R. C. Liebermann, and Y. Zhao, $P - V - T$ equation of state of (Mg, Fe)SiO₃ perovskite: constraints on composition of the lower mantle, *Phys. Earth Planet. Inter.*, *83*, 13–40, 1994.

Watt, J. P., G. F. Davies, and R. J. O'Connell, The elastic properties of composite materials, *Rev. Geophys. Space Phys.*, *14*, 541–563, 1976.

Weber, M., P– and S–wave reflections from anomalies in the lowermost mantle, *Gephys. J. Int.*, *115*, 183–210, 1993.

Williams, Q., The temperature contrast across D", in *The Core-Mantle Boundary Region*, edited by M. Gurnis, M. Wysession, E. Knittle, and B. Buffett, American Geophysical Union, Washington, DC, 1998.

Wysession, M. E., Imaging cold rock at the base of the mantle: The sometimes fate of slabs?, in *Subduction: Top to Bottom*, edited by G. E. Bebout, D. W. Scholl, S. H. Kirby, and J. P. Platt, American Geophysical Union, Washington, DC, 1996.

Wysession, M. E., T. Lay, J. Revenaugh, Q. Williams, E. Garnero, R. Jeanloz, and L. H. Kellogg, The D" discontinuity and its implications, in *The Core-Mantle Boundary Region*, edited by M. Gurnis, M. Wysession, E. Knittle, and B. Buffett, American Geophysical Union, Washington, DC, 1998.

Wysession, M. E., A. Langenhorst, M. J. Fouch, K. M. Fischer, G. I. Al-Eqabi, P. J. Shore, and T. J. Clarke, Lateral variations in compressional/shear velocities at the base of the mantle, *Science*, *284*, 120–125, 1999.

Yagi, T., T. Suzuki, and S. Akimoto, Static compression of wüstite (Fe₀.₉₈O) to 120 GPa, *J. Geophys. Res.*, *90*, 8784–8788, 1985.

Yagi, T., K. Fukuoka, H. Takei, and Y. Syono, Shock compression of wüstite, *Geophys. Res. Lett.*, *15*, 816–819, 1988.

Yamamoto, S., I. Ohno, and O. L. Anderson, High temperature elasticity of sodium chloride, *J. Phys. Chem. Solids*, *48*, 143–151, 1987.

Yeganeh-Haeri, A., Synthesis and re-investigation of the elastic properties of single-crystal magnesium silicate perovskite, *Phys. Earth Planet. Inter.*, *87*, 111–121, 1994.

Young, C. J., and T. Lay, Evidence for a shear velocity discontinuity in the lowermost mantle beneath India and the Indian Ocean, *Phys. Earth Planet. Inter.*, *49*, 37–53, 1987.

Young, C. J., and T. Lay, Multiple phase analysis of the shear velocity structure in the region beneath Alaska, *J. Geophys. Res.*, *95*, 17385–17402, 1990.

Yuen, D. A., A. M. Leitch, and U. Hansen, Dynamical influences of pressure-dependent thermal expansivity on mantle convection, in *Glacial Isostasy, Sea-level and Mantle Rheology*, edited by R. Sabadini and K. Lambeck, Kluwer, Dordrecht, 1991.

Yuen, D. A., O. Cadek, A. Chopelas, and C. Matyska, Geophysical inferences of thermal-chemical structures in the lower mantle, *Geophys. Res. Lett.*, *20*, 899–902, 1993.

Zhang, J., and T. Lay, Investigations of a lower mantle shear wave triplication using broadband array, *Geophys. Res. Lett.*, *11*, 620–623, 1984.

Zhao, Y., and D. L. Anderson, Mineral physics constraints on the chemical composition of the Earth's lower mantle, *Phys. Earth Planet. Inter.*, *85*, 273–202, 1994.

Zhong, S., and M. Gurnis, Dynamic feedback between a continentlike raft and thermal convection, *J. Geophys. Res.*, *98*, 12219–12232, 1993.

Zhong, S., and M. Gurnis, Mantle convection with plates and mobile, faulted plate margins, *Science*, *267*, 838–843, 1995.

Zhong, S., and M. Gurnis, Dynamic interaction between tectonic plates, subducting slabs, and the mantle, *Earth Interactions*, *1*(6), 1997, http://EarthInteractions.org/.

Zou, G. T., H. K. Mao, P. M. Bell, and D. Virgo, High-pressure experiments on the iron oxide wüstite ($Fe_{1-x}O$), *Year Book Carnegie Inst. Washington*, *79*, 374–376, 1980.